Electronic Applications of Magnetic Resonance Force Microscopy

Final Report Submitted to the Office of Naval Research
ONR Contract N00014-95-C-0124

DISTRIBUTION STATEMENT A
Approved for public release;
Distribution Unlimited

International Business Machines Corporation

Principal Investigator: Daniel Rugar

IBM Research Division
Almaden Research Center
650 Harry Rd.
San Jose, CA 95120-6099

Telephone: 408-927-2027
Fax: 408-927-2100
E-mail: rugar@almaden.ibm.com

Contents

1 **Overview** 1

1.1 Introduction 1

1.2 Organization of this report 3

1.3 Bibliography of papers published acknowledging ONR support 4

2 **Basic Principles** 6

2.1 Why low-temperature MRFM? 6

2.2 Low-temperature MRFM configuration 8

2.3 Force resolution 10

2.4 Active damping feedback 14

2.5 Techniques for generating oscillatory magnetic forces 17

2.5.1 Cyclic saturation 17

2.5.2 Cyclic adiabatic inversion 18

3 **MRFM Detection of Dopants in Silicon** 21

3.1 Experiment 22

3.2 Force detection of electron paramagnetic resonance 24

3.2.1 AM cyclic saturation 24

3.2.2 FM cyclic saturation 25

3.2.3 Observation of hyperfine splitting 27

3.2.4 Interrupted cyclic adiabatic inversion 30

4 E' Centers in SiO_2 35

4.1 Force detected EPR 37

4.1.1 Experiment 37

4.1.2 Cyclic adiabatic inversion 38

4.1.3 Steady-state magnetization during cyclic adiabatic inversion 40

4.2 Nonequilibrium magnetization measurements 42

4.2.1 Nutation 42

4.2.2 Spin echoes 46

4.3 Magnetization decay during adiabatic inversion cycles 49

5 EPR and FMR imaging 57

5.1 Improved MRFM setup 57

5.2 Cantilever with a magnetic tip in the external field 65

5.3 EPR of phosphorus-doped silicon 70

5.3.1 Low-dopant-concentration silicon 73

5.3.2 High-dopant-concentration silicon 83

5.4 EPR force imaging of DPPH sample 83

5.5 FMR force imaging 92

5.6 Magnetic field mapping using force-detected FMR 96

6 Single Spin Experiment 102

6.1 Experimental configuration 102

6.2 Ultrasensitive silicon cantilevers 105

6.3 Attonewton force detection 108

6.4 Magnetic tips 109

6.5 Single spin experiments 117

6.6 Key outstanding issues 119

List of Figures

2.1 Low temperature MRFM setup. 9

2.2 An optical micrograph of a typical cantilever and sample. . . . 12

2.3 Cantilever vibration decay. The motion of the cantilever was monitored by the fiber-optic interferometer and the amplitude of the vibration at the resonant frequency was measured after the vibration was driven. 13

2.4 The vibration noise of the cantilever. The motion of the cantilever was monitored by the fiber-optic interferometer and the amplitude of the vibration at the resonance frequency was measured at (a) 300 K and (b) 6 K. The measurement bandwidth was determined by the natural bandwidth of the cantilever, $\omega_c/4Q$ = 0.4 Hz for T = 300 K and 0.08 Hz for 6 K. 15

2.5 The laboratory frame and rotating frame. 19

3.1 Schematic setup of the experiment 22

3.2 Force-detected EPR spectrum of the high-concentration sample. (a) AM cyclic saturation with $T = 5.5$ K. (b) FM cyclic saturation with $T = 6.5K$ and $\Omega/2\pi = 10$ MHz. 26

3.3 Temperature dependence of the force-detected EPR signal of the high-concentration sample. For reference, the dotted line shows a slope of $T^{-1.5}$. 28

3.4 Force-detected EPR spectrum of the low-concentration sample using FM cyclic saturation for $T = 10$ K and $\Omega/2\pi = 10$ MHz. The 42-gauss spacing between the two bipolar features is due to ^{31}P hyperfine splitting. 29

3.5 Temperature dependence of the force-detected EPR signal for the low-concentration sample. For reference, the dotted line indicates a slope of T^{-3}. 31

3.6 Amplitude and frequency modulation pattern used for interrupted cyclic adiabatic inversion. 32

3.7 Force-detected EPR spectrum of the low-concentration sample for interrupted cyclic adiabatic inversion for $T = 6.5$ K and $\Omega/2\pi = 10$ MHz. 34

4.1 (a) Time dependence of the cantilever-vibration amplitude. The start and stop of the probe sequence are indicated by arrows. The probe sequence consists of frequency modulation to the microwave field such that $\Delta\omega(t) = -\Omega\cos(2\pi f_c t)$, inducing cyclic adiabatic inversion of the electron spin magnetization. The peak frequency deviation $\Omega/2\pi$ was 10 MHz. (b) Inverted cantilever response obtained when sample magnetization was adiabatically inverted by a frequency ramp before the probe sequence. 39

4.2 Force-detected EPR spectrum. The peak amplitude of the cantilever vibration is plotted as a function of the polarizing field strength. The peak deviation $\Omega/2\pi$ was 20 MHz, the cantilever response time was $\sim$ 10 ms, and the signal was averaged over 50 scans. The peak appears when $B_0 = \omega_0/\gamma$ at the sample position. 41

4.3 (a) Time dependence of the cantilever-vibration amplitude with a microwave input power of 52 mW ($B_1 = 0.82$ G). The vibration amplitude reaches a steady-state value by the end of the probe sequence. (b) The steady-state cantilever-vibration amplitude as a function of the B_0 strength. Absolute vibration amplitude is smaller than in (a) because greater damping feedback was used. 43

4.4 Force-detected nutation signal. The peak amplitude of the cantilever vibration is plotted as a function of the width of a microwave pulse t_p applied prior to the probe sequence. A microwave power of 130 mW was used for the pulse, and 4 mW was used for the probe sequence. The dotted line is a fit to a damped cosinusoidal oscillation with an offset. 45

4.5 (a) Pulse sequence used for the spin echo experiment. A microwave power of 130 mW was used for the pulses, and 4 mW was used for the probe sequence. Widths of $\pi/2$ and π pulses were 70 ns and 140 ns, respectively. (b) The peak amplitude of the cantilever vibration as a function of τ_A, with a fixed $\tau_B = 1$ μs. A peak appears when $\tau_A \simeq \tau_B/2$, corresponding to a spin echo. (c) Spin echoes observed with various τ_B. The amplitude of the spin echoes gradually decreases as τ_B increases. 47

4.6 The peak amplitude of the cantilever vibration as a function of the spin-lock time τ_{lock} before the probe sequence. The dotted line is a fit to an exponential decay with an offset. The signal decays with a time constant $T_{1\rho} \simeq 190$ ms. The inset shows the FM waveform used for the measurement. 50

4.7 Trapezoidal FM waveform used to study magnetization decay. The slope of the trapezoid is set such that $|\gamma^{-1}d\omega/dt| = |d\mathbf{B}_{\mathrm{eff}}/dt| = 3.0 \times 10^6$ G/s. 51

4.8 A typical cantilever response for the trapezoidal modulation. The line is a fit using the function in Eq. (4.5). The magnetization decay time τ_m is found to be 46 ms in this case. $B_1 = 1.35$ G. 53

4.9 Magnetization decay time τ_m as a function of B_1. Arrows indicate values of adiabaticity parameter $\gamma B_1^2/|d\mathbf{B}_{\mathrm{eff}}/dt|$. . . . 55

5.1 Schematic diagram of the improved low-temperature magnetic resonance force microscope. The microscope is suspended in a vacuum can that fits into a liquid-helium dewer with a superconducting magnet. 59

5.2 Close-up view of the microscope from the side. 61

5.3 Schematic setup of the experiment. 62

5.4 Block diagram of the experiment. 64

5.5 (a) Optical micrographs of the cantilever with a nickel sphere with $r \simeq 10$ μm. A pyramidal-shape silicon tip is also visible. (b) The cantilever with a nickel sphere with $r \simeq 55$ μm. 66

5.6 The dc deflection of the cantilever with a nickel sphere ($r \simeq 10$ μm) as the field is swept forward and backward. 68

5.7 Model of the cantilever deflection. 69

5.8 The resonant frequency of the cantilever with a nickel sphere ($r \simeq 10$ μm) as the field is swept forward and backward. . . . 71

5.9 (a) Q of the cantilever with a nickel sphere ($r \simeq 10$ μm) as a function of the field. (b) Q of the cantilever with a nickel sphere ($r \simeq 55$ μm) as a function of the field. 72

5.10 Force-detected EPR spectra of a ~100-μm-thick phosphorus-doped silicon sample. Dopant concentration is $\sim 8 \times 10^{16}$ cm^{-3}. Arrows indicate a peak that depends on the tip-sample distance. (a) The tip-sample distance was ~ 80 μm. (b) The tip-sample distance was ~ 60 μm. (c) The tip-sample distance was ~ 40 μm. 74

5.11 Contours of B_z from a fully magnetized nickel sphere ($r = 55$ μm). The z axis denotes the distance from the surface of the sphere. 76

5.12 Contours of $\partial B_z/\partial z$ from a fully magnetized nickel sphere ($r = 55$ μm). The z axis denotes the distance from the surface of the sphere. 77

5.13 Contours of $\partial B_z/\partial x$ from a fully magnetized nickel sphere ($r = 55$ μm). The z axis denotes the distance from the surface of the sphere. 78

5.14 The simulation result for EPR force for a thin sample and a 55-μm-radius nickel sphere tip. Tip-sample distance is 150 μm. 80

5.15 The simulation result for EPR force for a thin sample and a 55-μm-radius nickel sphere tip. Tip-sample distance is 100 μm. 81

5.16 The simulation result for EPR force for a thin sample and a 55-μm-radius nickel sphere tip. Tip-sample distance is 50 μm. 82

5.17 Force-detected EPR spectra for a high-concentration (4×10^{18} cm^{-3}) phosphorus-doped thin silicon sample. Tip-sample distances were approximately 100, 80, 60, and 40 μm. 84

5.18 (a) Optical micrograph of DPPH sample. (b) EPR force map obtained by scanning the DPPH sample in x-y at $B_{\text{ext}} = 3895$ G. 86

5.19 Optical micrograph of DPPH sample consisting of two particles. 87

5.20 EPR force maps obtained by scanning the DPPH sample in x-y at fixed values of B_{ext}. 89

5.21 Force-detected EPR spectrum for the DPPH sample. 90

5.22 Reconstructed three-dimensional magnetization image. Constant density surfaces are depicted from two viewing orientations. 93

5.23 (a) Force-detected FMR spectrum for a small YIG plate, showing a narrow-linewidth main signal. Arrows indicate small spectral features observed due to magnetostatic modes. (b) FMR force map at $B_{\text{ext}} = 4418$ G, showing a sharp ring-like response. Arrows indicate concentric ring-like responses due to magnetostatic modes. 95

5.24 (a) Force-detected FMR spectrum obtained at lower microwave power. Small spectral features believed to be due to magnetoelastic coupling are observed within the main line. (b) FMR force map at $B_{\text{ext}} = 4342$ G with the same microwave power. Note the spiral-like features superimposed on the main circular response. 97

5.25 Apparatus to quantitatively map the magnetic field emanating from a sample. A Ga-doped YIG particle mounted on the cantilever serves as a local probe of magnetic field emanating from a nearby sample. A cantilever vibration signal is generated whenever the field from the sample matches the field for ferromagnetic resonance of the YIG particle. 98

5.26 Force-detected ferromagnetic resonance spectrum of Ga-doped YIG particle. 99

5.27 MRFM image showing contours of constant field above a 20 micron diameter nickel sphere. 100

6.1 Experiment to detect individual electron spins (E' centers) in SiO_2. The 1 Å-thick resonant slice is shown by the dotted lines.103

6.2 Processing steps for fabricating ultrathin silicon cantilevers with integrated in-plane ferromagnetic tips. 106

6.3 A 600 Å-thick, 220 μm-long single-crystal silicon cantilever with in-plane tip. 108

6.4 Time trace of the cantilever vibration amplitude showing noise and response to an oscillating 36 aN-rms electrostatic force. The cantilever vibration amplitude is shown on the right hand scale and the corresponding force on the left hand scale. A force noise of 3.6 aN was measured. The bandwidth of the measurement was set by the natural bandwidth of the cantilever (approximately 0.4 Hz). 110

6.5 Hysteresis loop of cantilever frequency vs. applied field. 112

6.6 Model of single domain particle on a vertical cantilever. The easy axis of the particle is assumed to be aligned with the free end of the cantilever which, during vibration, tilts by an angle α. The particle magnetization is canted by an angle θ with respect to the particle easy axis because of a z-directed applied field. 114
6.7 The points show the increase in cantilever stiffness measured as a function of applied field for the reversible portion of the hysteresis loop. The solid curve is a plot of equation (6.10) using the fitting parameters shown. 116

Chapter 1

Overview

1.1 Introduction

This is the final report for Office of Naval Research Contract N00014-95-C-0124. Work under this recently completed contract has focused on improving the basic technology of magnetic resonance force microscopy (MRFM) and working towards the dual goals of dopant detection in silicon and single electron spin detection. In addition, a number of important advances were achieved, including ultrasensitive force detection, magnetic resonance characterization of dangling bond defects in SiO_2, and two- and three-dimensional imaging of both paramagnetic and ferromagnetic resonance on the micron-scale.

Magnetic resonance force microscopy[1, 2, 3] (MRFM) is a new scanning probe microscope technique that combines aspects of magnetic resonance imaging (MRI) and atomic force microscopy (AFM). IBM's interest in MRFM is driven by the possibility of achieving non-invasive, three-dimensional imaging with atomic-resolution and elemental selectivity. If this goal can be realized, the technique would have a revolutionary impact on the field of microscopy and have many important applications. Potential applications include: 1) determining the sub-surface, three-dimensional structure of solid state materials, 2) imaging three-dimensional distributions of dopants in semiconductors with angstrom spatial resolution, 3) imaging defects and trapping sites in semiconductors, 4) imaging interactions between polymer molecules, 5) determining the three-dimensional atomic structure of macromolecules, such as proteins.

The long-term goal of single nuclear spin detection and imaging is an extremely challenging one due to the smallness of the forces that need to be detected (e.g., attonewtons). Because of the many challenges, IBM is pursuing a step-by-step approach wherein new force sensing and magnetic resonance techniques are being introduced in stages and intermediate results obtained. Microscopes with progressively greater sensitivity and spatial resolution are constructed as new force sensing and magnetic resonance techniques are developed. Applications demonstrating the efficacy of new techniques are being developed in parallel with improvements in imaging capability. The recent experimental emphasis has been on electron spin resonance, instead of nuclear magnetic resonance, because of the larger magnetic moment of the electron.

Work under the ONR contract was aimed at extending the capability of micron-scale MRFM, while simultaneously working towards single spin imaging with nanometer resolution. Specific accomplishments include:

1. Achievement of spin sensitivity that is 100-1000 better than conventional magnetic resonance techniques.

2. Operation of two low temperature MRFM apparatuses: one for micron-scale studies and one for single spin detection.

3. ESR-MRFM studies of a) phosphorus dopants in silicon, b) dangling

bonds in SiO_2, c) organic free radicals (DPPH), and d) yttrium-iron-garnet ferromagnetic resonance.

4. First demonstration of MRFM with a tip-on-cantilever configuration. True three-dimensional (volumetric) imaging at the micron scale was demonstrated.
5. Demonstration of attonewton force sensitivity using ultrathin single crystal silicon cantilevers. This is the most sensitive mechanical force detection ever demonstrated.
6. Demonstration of the key ingredients for single spin MRFM experiments, including a) operation of ultrathin vertical cantilevers within 10 nm of a sample surface at low temperature, b) development and characterization of magnetic tips compatible with ultrathin silicon cantilevers; c) characterization of electron spins in a test sample consisting of dangling bond defects in SiO_2 (E' centers).
7. Demonstration of quantitative magnetic field mapping using force-detected ferromagnetic resonance.

1.2 Organization of this report

This report is organized into chapters that describe various aspects of MRFM covered under the ONR contract. Portions of the report, especially chapters 2–5, are adapted from the Ph.D. thesis of Koichi Wago, who was partially supported by the contract.

Chapter 2 overviews basic principles of low temperature MRFM and experimental procedures. Force resolution achievable at low temperature is also discussed in Chapter 2.

Chapter 3 describes the detection of phosphorus dopants in silicon by force-detected electron paramagnetic resonance. We also discuss experiments on force-detected EPR spectroscopy, including the observation of the hyperfine splitting due to ^{31}P nuclei.

Chapter 4 describes EPR measurements of E' centers (dangling bond defects) in SiO_2, including spectroscopy, spin nutation and spin echoes. Relaxation times of electron spins while undergoing cyclic adiabatic inversion are presented and discussed in terms of the utility for future single-spin detection experiments.

Chapter 5 describes an improved MRFM configuration incorporating a magnetic tip mounted directly on the cantilever. The improved microscope was used to compare and contrast two- and three-dimensional imaging characteristics of EPR and ferromagnetic resonance (FMR). Quantitative magnetic field mapping on the micrometer scale is also discussed.

Chapter 6 discusses the ongoing effort aimed at detecting individual electron spins. It describes the basic experimental approach and the status of key experimental sub-systems, including fabrication of ultrasensitive silicon cantilevers capable of detecting attonewton forces.

1.3 Bibliography of papers published acknowledging ONR support

A number of technical papers were published acknowledging ONR support, including the following:

- "Paramagnetic and ferromagnetic resonance imaging with a tip-on-cantilever magnetic resonance force microscope", K. Wago, D. Botkin, C.S. Yannoni and D. Rugar, Appl. Phys. Lett. **72**, May 1998 (in press).

- "Attonewton force detection using ultrathin silicon cantilevers", T. Stowe, K. Yasumura, T. Kenny, D. Botkin and D. Rugar, Appl. Phys. Lett. **71**, 288 (1997).
- "Force-detected electron spin resonance: adiabatic inversion, nutation and spin echo", K. Wago, D. Botkin, O. Zueger, R. Kendrick, C.S. Yannoni and D. Rugar, Phys. Rev. B **57**, 1108 (1998).
- "Magnetic resonance force microscopy", D. Rugar, K. Wago, D. Botkin, C.S. Yannoni, T. Stowe, K. Yasumura and T. Kenny, invited paper for Proceedings of the Robert A. Welch Foundation 40th Conference on Chemical Research - Chemistry on the Nanometer Scale.
- "Torsional force probes optimized for higher order mode suppression", T. Stowe, K. Yasumura, T. Pfafman, T. Kenny, D. Botkin, D. Rugar, Proceedings of 1997 International Conference on Solid-state Sensors and Actuators, Chicago, IL, p.141 (1997).
- "Ultrasensitive vertical force probe for magnetic resonance force microscopy", T. Stowe, K. Yasumura, T. Kenny, D. Botkin, K. Wago and D. Rugar, Proceedings of Solid State Sensors and Actuators Workshop, Hilton Head, SC, June 2-6, 1996.

Chapter 2

Basic Principles

2.1 Why low-temperature MRFM?

Improving the detectability of small forces is a key aspect of MRFM research since the force resolution, in combination with the magnitude of the tip field gradient, sets the ultimate spin sensitivity. The force resolution of a cantilever-based force sensor is fundamentally limited by thermomechanical noise. If a cantilever with a spring constant k is in thermal equilibrium at temperature T, the equipartition theorem predicts

$$\frac{1}{2}k\langle x^2\rangle = \frac{1}{2}k_B T, \tag{2.1}$$

where $\langle x^2\rangle$ is the mean-square vibration amplitude of the cantilever and k_B is the Boltzmann constant. If we assume that the vibration noise arises from a force noise with a flat power spectrum S_F, then the resulting cantilever vibration amplitude is

$$\langle x^2\rangle = \int_0^\infty S_F |G(\omega)|^2 \frac{d\omega}{2\pi}, \tag{2.2}$$

where

$$G(\omega) = \frac{\omega_c^2/k}{(\omega_c^2 - \omega^2) + i\omega_c\omega/Q} \tag{2.3}$$

is the transfer function of the cantilever with a spring constant k, resonant frequency ω_c, quality factor Q. Integration of Eq. (2.2) for $Q \gg 1$ gives

$$\langle x^2 \rangle = S_F \frac{\omega_c Q}{4k^2}. \tag{2.4}$$

From Eqs. (2.1) and (2.4), we obtain

$$S_F = \frac{4kk_BT}{\omega_c Q}, \tag{2.5}$$

and the minimum detectable force in a detection bandwidth $\Delta\nu$ is given by[4, 5, 6]

$$F_{\min} = S_F^{1/2}(\Delta\nu)^{1/2} = \sqrt{\frac{4kk_BT\Delta\nu}{Q\omega_c}}. \tag{2.6}$$

It is clear from Eq. (2.6) that low-temperature operation should increase the sensitivity of MRFM. An additional advantage of low-temperature operation is that the magnetic moment due to spin polarization, which is inversely proportional to temperature, will also increase, resulting in a larger force signal. Equation (2.6) also suggests the strategy on choosing cantilevers: use a soft (small k) cantilever with high Q. Operating at low temperature will benefit in this sense as well, since Q generally improves at lower temperature[7].

This chapter and chapters 3–5 concentrate on low temperature MRFM experiments using commercially available cantilevers capable of force detection in the femtonewton range. Chapter 6 shows how the force resolution can be extended to the attonewton range using ultrathin custom-fabricated cantilevers.

2.2 Low-temperature MRFM configuration

Figure 2.1 shows the schematic of an experimental apparatus used for micron-scale MRFM experiments. The MRFM apparatus was suspended in a vacuum can in a liquid helium dewer[8] with a superconducting magnet to generate a polarizing magnetic field. The apparatus was cooled via a copper braid connected to the bottom of the can to provide thermal conduction while maintaining adequate vibration isolation.

To ensure that the resonant volume is large enough to generate a measurable signal, a millimeter-size magnetic tip was placed external to the cantilever and the sample was directly glued onto the cantilever. For example, an iron tip of 1.5 mm diameter and 3 mm long was placed roughly 700 μm away from the cantilever for the NMR experiments in Chapter.

The rf field B_1 was applied to the sample using a nearby coil to induce magnetic resonance. The polarizing magnetic field B_0 was a combination of the field from the superconducting magnet and the field from the magnetic tip. The oscillatory magnetic force resulting from magnetic resonance excites the vibration of the cantilever. The angstrom-scale motion of the cantilever was measured with a fiber-optic interferometer [9] and was synchronously detected with a lock-in amplifier.

It might seem that, since the magnetic force is proportional to the field gradient, using a smaller tip placed closer to the sample should increase the signal due to the stronger field gradient. In general, scaling down dimensions of the tip size and tip-sample distance increases the field gradient in inverse proportion to the scale factor. This has the beneficial effect of increasing the force per spin (or per unit volume). However, the resonant volume decreases faster as the dimensions are scaled down, because not only the thickness of the resonant slice scales down in proportion to the scale factor, but the area

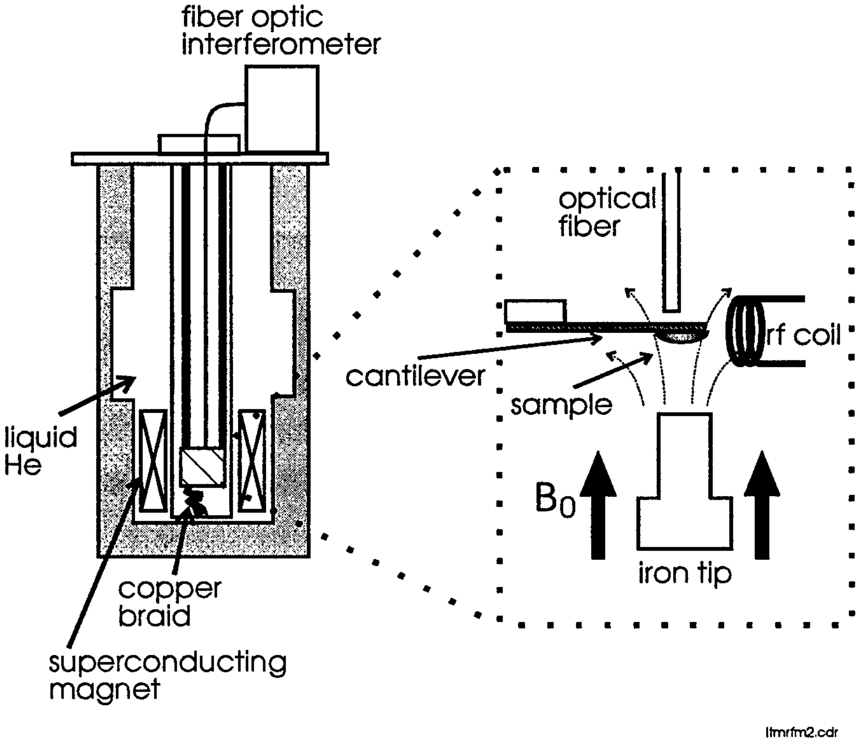

Figure 2.1: Low temperature MRFM setup.

covered by the resonant slice decreases as well. As a result, the net force, (force per volume) × (resonant volume), decreases as the dimensions are scaled down.[1]

In the configuration shown in Fig. 2.1, where a micron-size sample and a millimeter-size magnetic tip are used, the resonant volume is given by

$$V = \Delta x \Delta y \frac{\Delta B}{|\nabla B_{\mathrm{tip}}|}, \tag{2.7}$$

where Δx and Δy are the sample lateral dimensions and ΔB is the magnetic resonance linewidth.[2] The force per volume is given by

$$F = \frac{N\mu^2 B_0}{k_B T} |\nabla B_{\mathrm{tip}}|, \tag{2.8}$$

where N is the number of spin per volume. The net force is then given by

$$F_{\mathrm{net}} = \frac{N\mu^2 B_0}{k_B T} \Delta x \Delta y \Delta B. \tag{2.9}$$

Substituting typical numbers[3] $N = 4.9 \times 10^{22}$ cm^{-3}, $\mu = 1.33 \times 10^{-26}$ J/T, $B_0 = 2.5$ T, $\Delta x = \Delta y = 10$ μm, $k_B = 1.38 \times 10^{-23}$ J/K, $T = 5$ K, and $\Delta B = 2$ G, we obtain $F_{\mathrm{net}} \simeq 6 \times 10^{-15}$ N, which should be detectable as discussed in the next Section.

2.3 Force resolution

For experiments described in Chapters 2-6, we used commercial single-crystal-silicon cantilevers[10] with dimensions of approximately 470 μm × 45 μm ×

---

[1] This argument does not apply to the case of single-spin MRFM, for which the gradient may be increased without concern for the size of the resonant volume.

[2] The sample is assumed to be thicker than the resonant slice such that $\Delta z > \Delta B/|\nabla B_{\mathrm{tip}}|$.

[3] The values of N and μ are for ^{19}F in 1% Nd-doped CaF$_2$. Linewidth ΔB is generally determined by the natural linewidth and the modulation amplitude used to generate the oscillatory force as discussed later.

1.5 μm, a spring constant $k \simeq 0.07$ N/m, and a resonance frequency $f_c \simeq 9.8$ kHz. Figure 2.3 shows the optical micrograph of a typical cantilever with sample loaded.[4]

The single-crystal-silicon cantilevers showed very high Q in vacuum ($\sim 10^{-5}$ torr) and at low temperature. Q was determined by measuring the decay time of the vibration amplitude after the vibration was driven by a piezoelectric actuator at the base of the cantilever. Figure 2.3 shows a typical Q measurement for a cantilever with sample loaded (resonant frequency $f_c = 1.6$ kHz). Decay time becomes longer as the temperature is decreased, yielding $Q \simeq 500\,000$ at 6 K, improved from $Q \simeq 20\,000$ at room temperature.

Low temperature force resolution was characterized using a bare silicon cantilever ($f_c = 9.8$ kHz). Figure 2.4 shows the thermal vibration amplitude of the cantilever measured synchronously at the cantilever resonant frequency. The vibration amplitude was 1.1 Å-rms at room temperature and decreased to 0.26 Å-rms at 6 K. From the spring constant, the Q at each temperature,[5] and the position of the optical fiber, we estimate[6]

---

[4] The samples were glued onto cantilevers with a UV-curing epoxy (Loctite). A pipette with a sharp pulled end (prepared using lighter flame) and a micromanipulator were used under a microscope to mount the sample on the cantilever.

[5] $Q \simeq 40\,000$ at room temperature and $Q \simeq 200\,000$ at 6K for this cantilever.

[6] The procedure we used to determine $S_F^{1/2}$ is as follows. The root-mean-square cantilever vibration amplitude, A, was measured at both 300 K and 6 K using a lock-in amplifier with a short time constant ($\tau_L = 100$ ms). The short time constant ($\tau_L \ll Q/\omega_c$) ensured that the entire bandwidth of the cantilever noise was detected. A correction factor, c, was applied to account for the fact that the optical fiber was not measuring the motion of the cantilever end, but rather at a point approximately 40% from the end. The correction factor was determined using room-temperature thermal noise such that $k(cA_{300K})^2/2 = k_B T/2$ for $T = 300$ K. The determined value, $c = 2.3$, was consistent with that estimated from the mode shape, $\phi(x) = [\cosh \kappa x - \cos \kappa x - \sigma(\sinh \kappa x - \sin \kappa x)]/2$,

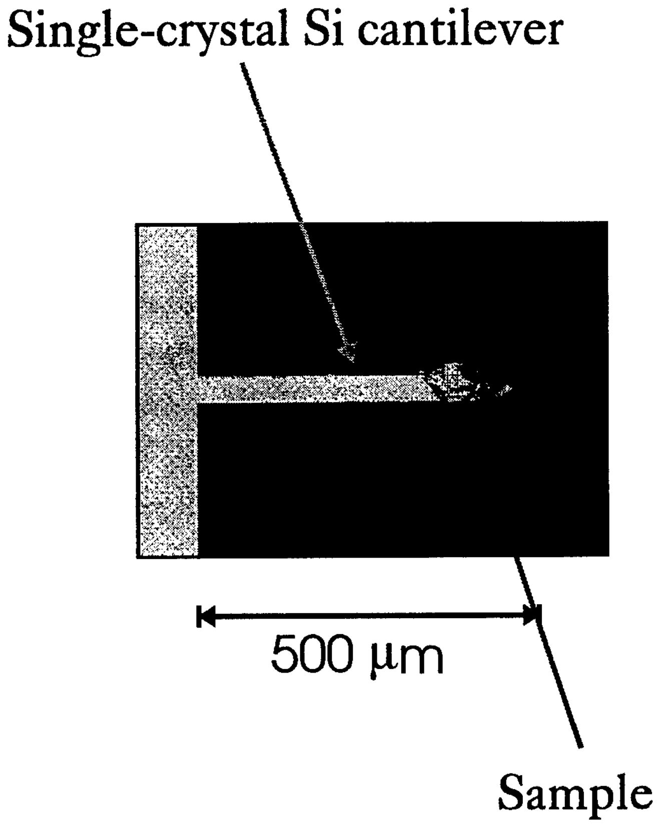

Figure 2.2: An optical micrograph of a typical cantilever and sample.

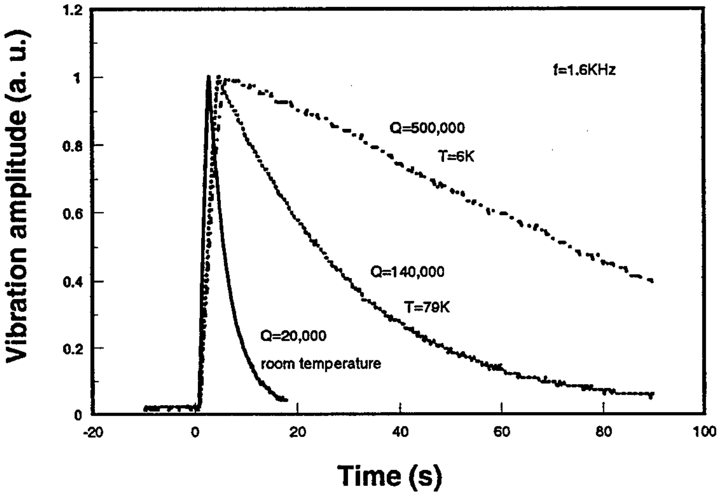

Figure 2.3: Cantilever vibration decay. The motion of the cantilever was monitored by the fiber-optic interferometer and the amplitude of the vibration at the resonant frequency was measured after the vibration was driven.

$S_F^{1/2} = 8 \times 10^{-17}$ N/$\sqrt{\text{Hz}}$ at 6 K. This is a factor of 8 improvement compared to room temperature. The measured force resolution is about two times larger than the theoretical value, 4.3×10^{-17} N/$\sqrt{\text{Hz}}$, calculated from Eq. (2.5). The discrepancy is probably due to some environmental vibration noise.

2.4 Active damping feedback

In addition to the improved force resolution, the high Q of the silicon cantilever also means that it takes a long time for the vibration amplitude to reach the steady state value. In order to speed up the cantilever response, an electromechanical feedback technique was often used[11, 12, 13]. A damping feedback signal, 90° phase-shifted from the measured cantilever vibration signal $x(t)$, was applied to the piezoelectric actuator at the base of the cantilever.

The feedback force is proportional to $\dot{x}(t)$ and can be written as $F_{\text{feedback}}(\omega) = -i\alpha\omega x(\omega)$ in the Fourier domain, where α is a constant. The cantilever vibration amplitude $x(\omega)$ driven by a force $F(\omega)$ is then described as

$$x(\omega) = G(\omega)\left[F(\omega) + F_{\text{feedback}}(\omega)\right] = G(\omega)\left[F(\omega) - i\alpha\omega x(\omega)\right], \tag{2.10}$$

where

$$G(\omega) = \frac{\omega_c^2/k}{(\omega_c^2 - \omega^2) + i\omega_c\omega/Q} \tag{2.11}$$

is the transfer function of the cantilever as in Eq. (2.3). We can rewrite Eq. (2.10) as

$$x(\omega) = G_{\text{eff}}(\omega)F(\omega), \tag{2.12}$$

---

where $\kappa \simeq 1.875/L$ and $\sigma \simeq 0.734$. Spectral density of the force noise at 6 K was estimated according to $S_F^{1/2} = kcA_{6K}/Q \cdot (4Q/\omega_c)^{1/2}$ (units of N/$\sqrt{\text{Hz}}$). The quantity $4Q/\omega_c$ is the inverse of the equivalent noise bandwidth of the cantilever resonance.

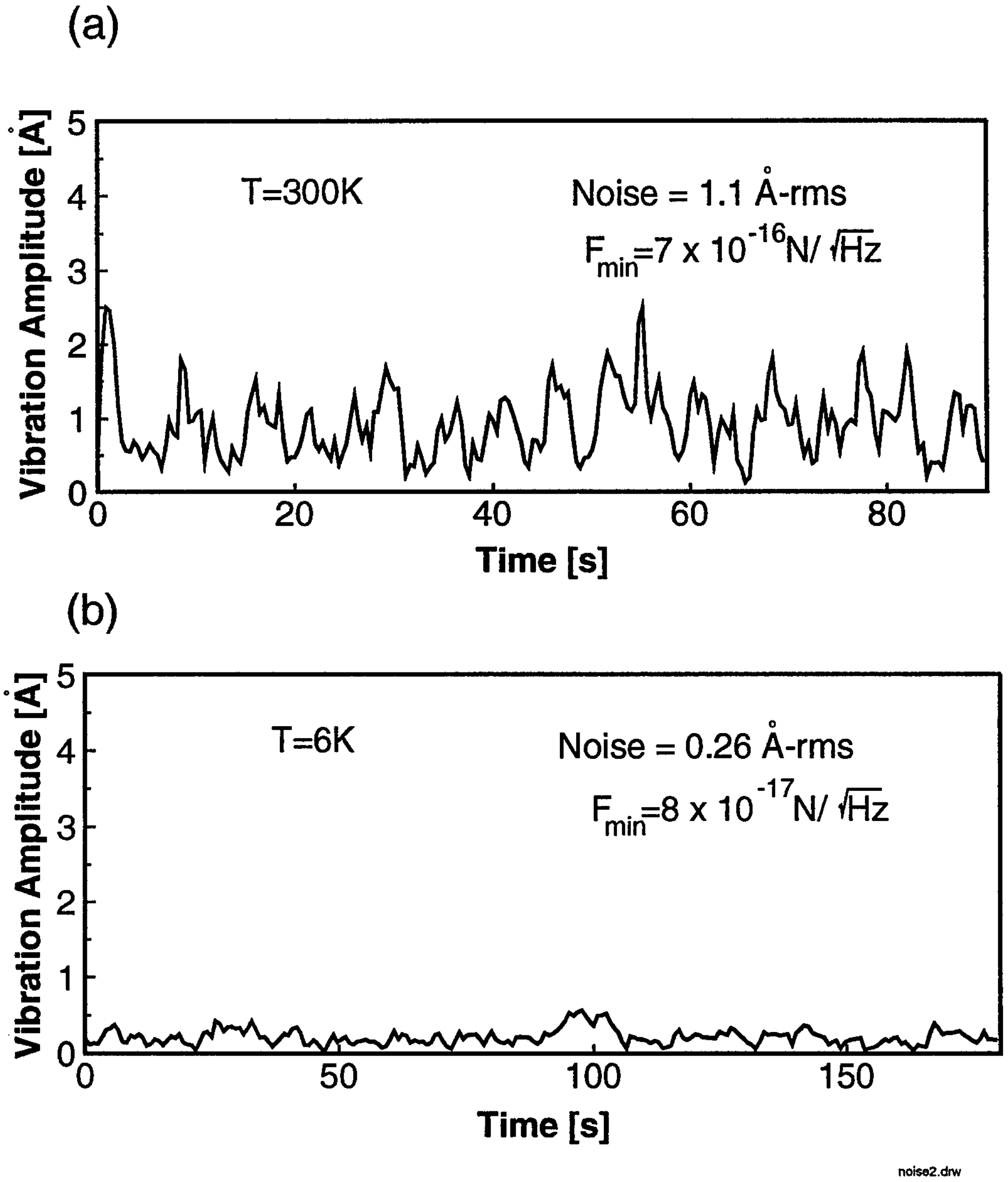

Figure 2.4: The vibration noise of the cantilever. The motion of the cantilever was monitored by the fiber-optic interferometer and the amplitude of the vibration at the resonance frequency was measured at (a) 300 K and (b) 6 K. The measurement bandwidth was determined by the natural bandwidth of the cantilever, $\omega_c/4Q = 0.4$ Hz for $T = 300$ K and 0.08 Hz for 6 K.

where

$$G_{\text{eff}}(\omega) = \frac{\omega_c^2/k}{(\omega_c^2 - \omega^2) + i\omega_c\omega/Q_{\text{eff}}} \tag{2.13}$$

with an effective Q

$$Q_{\text{eff}} = \left(\frac{1}{Q} + \frac{\alpha\omega_c}{k}\right)^{-1}. \tag{2.14}$$

As a result, the $1/e$ response time of the cantilever is reduced to $\tau_{\text{eff}} = 2Q_{\text{eff}}/\omega_c$ from $\tau = 2Q/\omega_c$.

This reduction of effective Q and τ occurs without degrading the force resolution for the same detection bandwidth, since the active damping does not affect the spectral density of the noise force S_F. S_F is determined by the coupling to the thermal bath and given by $S_F = 4kk_BT/\omega_cQ$ as in Eq. (2.5), where Q is the intrinsic Q of the cantilever.

The advantage of using feedback to speed up the cantilever response rather than using a cantilever with low intrinsic Q can be understood if we consider the energy of the actively damped cantilever. The mean-square vibration amplitude due to thermal noise is given by

$$\begin{aligned} \langle x^2 \rangle &= \int_0^\infty S_F |G_{\text{eff}}(\omega)|^2 \frac{d\omega}{2\pi} \\ &= \frac{Q_{\text{eff}}}{Q} \int_0^\infty S_F |G(\omega)|^2 \frac{d\omega}{2\pi}, \end{aligned} \tag{2.15}$$

and is therefore reduced by a factor of Q_{eff}/Q compared to the case without feedback given by Eq. (2.2). The energy of the cantilever is

$$\frac{1}{2}k\langle x^2 \rangle = \frac{Q_{\text{eff}}}{Q} \cdot \frac{1}{2}k_BT, \tag{2.16}$$

and no longer in thermal equilibrium with its environment.

2.5 Techniques for generating oscillatory magnetic forces

The maximum vibrational response of the cantilever is achieved when the sample magnetization, and hence the resulting magnetic force, is cyclically modulated at the mechanical resonant frequency of the cantilever ω_c. Typically ω_c is in the kilohertz range, much slower than the Larmor frequency. Thus, at least for our present cantilevers, the precession of the magnetization cannot be directly used as the source of oscillatory forces matched to ω_c. Instead, two techniques, described below, have been used to modulate the longitudinal component of the magnetization M_z, causing $F_z = M_z(\partial B_{\text{tip}}/\partial z)$ to oscillate at ω_c.

2.5.1 Cyclic saturation

In general, the behavior of the magnetization is described phenomenologically by the Bloch equation given by[14]

$$\frac{d\mathbf{M}}{dt} = \mathbf{M} \times \gamma \mathbf{B} - \frac{M_x \mathbf{i} + M_y \mathbf{j}}{T_2} - \frac{(M_z - M_0)\mathbf{k}}{T_1}, \tag{2.17}$$

where $\mathbf{i}$, $\mathbf{j}$, and $\mathbf{k}$ are unit vectors in the x, y, and z directions, respectively, and M_0 is the equilibrium magnetization, T_1 and T_2 are spin-lattice and spin-spin relaxation times, respectively. In the presence of the static field B_0 in the z direction and the rf field B_1 at frequency ω in the x direction, it is customary to introduce the rotating frame at frequency ω, where B_1 is stationary.[7] The steady state solution of the Bloch equation (*i.e.*, $d\mathbf{M}/dt = 0$) in the rotating

---

[7] B_1 is decomposed into two circularly polarized components rotating in opposite directions in the xy plane and we use the approximation to ignore the counter rotating component.

frame leads to

$$M_z = M_0 \left[1 - \frac{\gamma^2 B_1^2 T_1 T_2}{1 + (\gamma B_0 - \omega)^2 T_2^2 + \gamma^2 B_1^2 T_1 T_2} \right]. \tag{2.18}$$

For the spins that are excited at resonance ($\omega = \gamma B_0$), M_z is suppressed to the value $M_0 - \delta M_z$, where

$$\delta M_z = \frac{M_0 \gamma^2 B_1^2 T_1 T_2}{1 + \gamma^2 B_1^2 T_1 T_2}. \tag{2.19}$$

Modulating either the amplitude B_1, frequency ω of the rf field, or the polarizing field strength B_0 at frequency ω_c cyclically suppresses M_z, causing the magnetic force F_z to oscillate at ω_c. An assumption made here is that the magnetization reaches the steady state value sufficiently fast ($T_1, T_2 \ll 1/\omega_c$), which is typically the case for electron spin systems. This technique was used for the first EPR-MRFM experiments[2, 15, 16].

2.5.2 Cyclic adiabatic inversion

For spins with long relaxation times, the cyclic saturation technique is not effective. An alternative method is the cyclic adiabatic inversion technique used in NMR-MRFM[11, 17].

In the rotating frame, B_0 is transformed to $B_0 - \omega/\gamma$ as shown in Fig. 2.5[18]. The magnetization precesses about the effective field

$$\mathbf{B}_{\text{eff}} = B_1 \hat{\mathbf{x}} + \left(B_0 - \frac{\omega}{\gamma} \right) \hat{\mathbf{z}}, \tag{2.20}$$

where $\hat{\mathbf{x}}$ and $\hat{\mathbf{z}}$ are unit vectors in the rotating frame. $\mathbf{B}_{\text{eff}}$ can be manipulated by modulating the frequency ω. If the direction of $\mathbf{B}_{\text{eff}}$ is changed starting from being parallel to the magnetization, then the magnetization follows the direction of $\mathbf{B}_{\text{eff}}$ as long as the rate of change is "slow" enough such that

$$\left| \frac{d\mathbf{B}_{\text{eff}}}{dt} \right| \ll \gamma B_1^2. \tag{2.21}$$

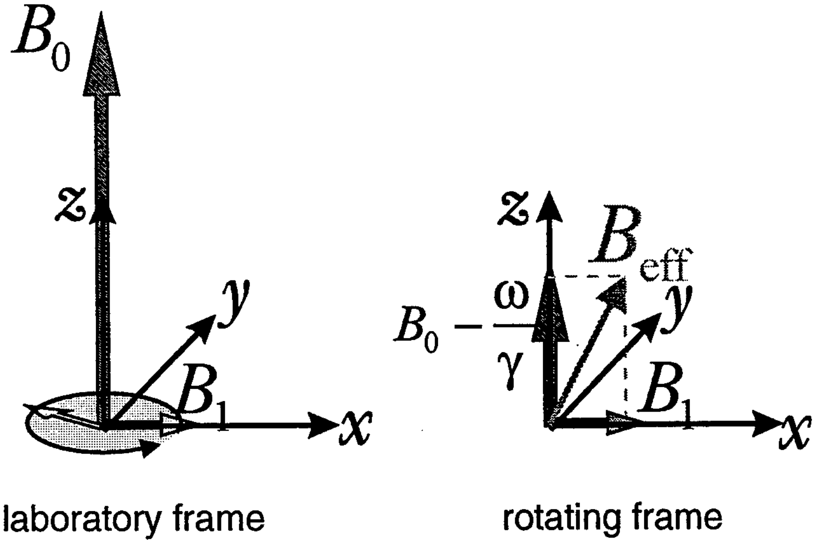

Figure 2.5: The laboratory frame and rotating frame.

This condition is described by the term “adiabatic” condition[18].

For example, modulating the frequency of the rf field ω such that

$$\omega(t) = \omega_0 - \Omega \cos \omega_c t, \tag{2.22}$$

where $\omega_0 = \gamma B_0$, causes $\mathbf{B}_{\text{eff}}$ to swing up and down at ω_c. If the adiabatic condition is satisfied, the magnetization is cyclically inverted following $\mathbf{B}_{\text{eff}}$, resulting in the oscillatory magnetic force F_z. In terms of frequencies, the adiabatic condition (2.21) becomes

$$\left| \frac{d\omega}{dt} \right| \ll \gamma^2 B_1^2 \tag{2.23}$$

or

$$\Omega \omega_c \ll \gamma^2 B_1^2. \tag{2.24}$$

Chapter 3

MRFM Detection of Dopants in Silicon

One potential technological application of MRFM is the imaging of dopants in semiconductors. This chapter describes basic experiments that demonstrate detection and spectroscopy of phosphorus dopants in silicon using force-detected electron paramagnetic resonance (EPR).[1] Force-detected EPR spectra were obtained using an amplitude or frequency modulated microwave field to cyclically saturate the spin magnetization. For a sample containing 4×10^{18} phosphorus atoms/cm^3, a single strong EPR line was observed. For a sample containing 8×10^{16} phosphorus atoms/cm^3, a pair of lines split by the 42-gauss ^{31}P hyperfine interaction was observed. This result demonstrates the possibility of using MRFM techniques for spectroscopic purposes.

---

[1] A portion of the work presented in this chapter was performed after the submission of the ONR contract proposal in 1995, but before the official start of the contract. We include the results here since they are directly relevant to the goals of the contract

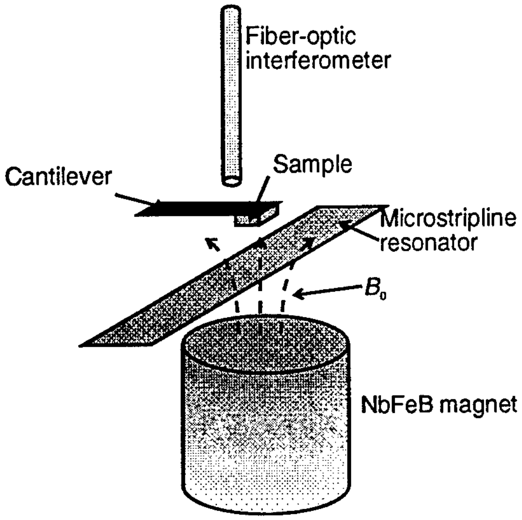

Figure 3.1: Schematic setup of the experiment

3.1 Experiment

The experimental apparatus is shown schematically in Fig. 3.1.

Two samples with different phosphorus concentrations were studied. The "high-concentration" sample had a phosphorus concentration $N_D = 4 \times 10^{18}$ cm^{-3}, and had a size of roughly 25μm × 25μm × 5μm. The "low-concentration" sample had $N_D = 8 \times 10^{16}$ cm^{-3} and was slightly larger in size. The samples were glued onto commercial single-crystal-silicon cantilevers[10] with spring constant $k \simeq 0.07$ N/m. The resulting mechanical resonant frequencies f_c were 7.6 kHz and 5.0 kHz for the high and low concentration samples, respectively. The vibration amplitude of the cantilever was monitored with a fiber-optic interferometer[9] using an optical power of less than 10 μW at the cantilever. At higher optical power, we found that the cantilever Q was affected by an interaction between the laser light and the cantilever and, depending on the condition of optical interference, Q was either suppressed or enhanced.

EPR was excited by a microwave field B_1 at a frequency $\omega/2\pi = 12.6$ GHz using an end-coupled half-wavelength microstripline resonator[19, 20]. The resonator consisted of a 4 mm long section of 50-ohm-impedance microstrip transmission line fabricated on a 0.5 mm thick sapphire substrate. With an input power of 24 mW, the resonator produced 0.6 G at the sample position 200 μm above the center of the resonator.[2] A NdFeB permanent magnet, 3 mm in both diameter and length, was located 800 μm away from the sample, and produced a field gradient $G = 2$ G/μm. This served to generate a magnetic force on the sample, as well as defining a "resonant slice" within which the magnetic resonance condition, $\omega = \gamma B_0$, is satisfied. The total field B_0 was a combination of the fields from the permanent magnet (~ 2000 G) and a superconducting magnet. A control experiment was performed to verify that antimony dopants in the cantilever contribute no EPR force signal. Presumably this is because of the very short relaxation times of antimony-doped silicon[21].

---

[2] The strength of B_1 was calibrated by spin nutation experiments described in Chapter 4.

3.2 Force detection of electron paramagnetic resonance

Cyclic saturation, described in Section 2.5.1, was used to induce an oscillatory component in the longitudinal magnetization M_z. Either amplitude modulation of B_1 (AM cyclic saturation) or frequency modulation of B_1 (FM cyclic saturation) was used, as described below.

3.2.1 AM cyclic saturation

For the case of AM cyclic saturation, B_1 was modulated at frequency f_c so that B_1 was turned on and off with a 50% duty cycle. As a result, M_z oscillates between the values M_0 and $M_0 - \delta M_z$ (see Eq. (2.19)) with frequency f_c, provided that T_1 is short enough so that M_z reaches its steady state value quickly compared with the time scale of $1/f_c$. The oscillating magnetization has the first-harmonic Fourier component $M_1 = (2/\pi)\delta M_z$, which produces an oscillating magnetic force $M_1 G$ in the presence of the field gradient G. Spins that are slightly off resonance also contribute to the oscillatory force but less effectively since the suppression of M_z is not complete. The total force is obtained by integrating these contributions over the sample volume taking into account that B_0 is a function of position z. Therefore

$$F = \frac{2}{\pi} \int \frac{M_0 \gamma^2 B_1^2 T_1 T_2}{1 + [\gamma B_0(z) - \omega]^2 T_1^2 + \gamma^2 B_1^2 T_1 T_2} G A(z)\, dz, \qquad (3.1)$$

where $A(z)$ is the cross-sectional area of the sample at z. The dominant contribution to the total force originates from the spins in the resonant slice, the thickness of which is on the order of $\Delta B/G$, where $\Delta B = 2\sqrt{1 + \gamma^2 B_1^2 T_1 T_2}/(\gamma T_2)$ is the full-width-at-half-maximum of the resonance given by Eq. (2.18). If the strength of the polarizing field B_0 is scanned by changing the external field from the superconducting magnet, the oscillatory magnetic force F is expected to be at its maximum when the resonant slice falls roughly in the middle of the sample.

Figure 3.2(a) shows the force-detected EPR spectrum for the high-concentration sample at $T = 5.5$ K. B_1 amplitude modulation was applied and B_0 was swept while measuring the cantilever vibration amplitude. A single peak was observed with a maximum force of about 10^{-14} N. The observed linewidth of 6 G is not the intrinsic linewidth ΔB, but rather includes additional broadening due to the extended sample thickness in the presence of the field gradient.

3.2.2 FM cyclic saturation

For the case of FM cyclic saturation, the microwave frequency was modulated as $\omega(t) = \omega_0 + \Omega \sin(2\pi f_c t)$, generating a time varying $M_z(t)$ that contains the first-harmonic Fourier component M_1. For small values of Ω, M_1 is given by $\Omega \partial M_z / \partial \omega$. M_1 is zero exactly on resonance ($\omega_0 = \gamma B_0$) and has positive and negative peaks at $B_0 = \omega_0/\gamma \pm \Delta B / 2\sqrt{3}$ when B_0 is swept through the resonance. For an extended sample, the bipolar nature of the resonance line leads to cancellation of the net force when the resonant slice is in the center of the sample. The net force is maximum when the resonant slice is positioned at either edge of the sample. Figure 3.2(b) shows the force-detected EPR spectrum measured with FM cyclic saturation for the high-concentration sample. The peak deviation $\Omega/2\pi$ was 10 MHz and $T = 6.5$ K. The spectrum shows positive and negative peaks, resembling the derivative of Eq. (2.18) as expected. The observed linewidth was 6 G. There are three factors contributing to this linewidth: (1) the intrinsic linewidth of the resonance, (2) broadening due to the frequency modulation, and (3) broadening due to the sample thickness in the presence of the field gradient.

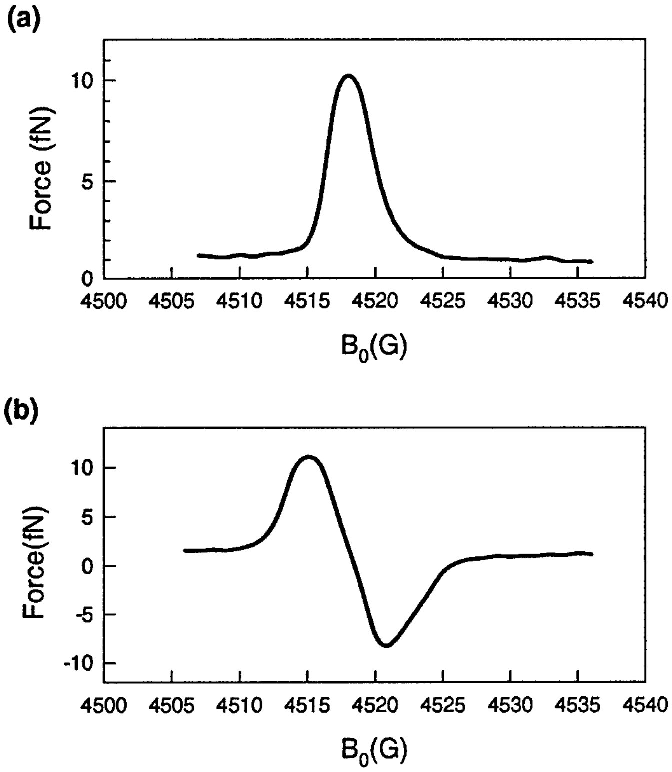

Figure 3.2: Force-detected EPR spectrum of the high-concentration sample. (a) AM cyclic saturation with $T = 5.5$ K. (b) FM cyclic saturation with $T = 6.5K$ and $\Omega/2\pi = 10$ MHz.

The difference between the positive and the negative force peak is plotted as a function of temperature in Fig. 3.3. The force-detected EPR signal increased as the temperature decreased and was approximately proportional to $T^{-1.5}$. Due to the nature of degenerate conduction-electron paramagnetism (Pauli paramagnetism), the temperature dependence of the magnetization M_0 can be neglected in this temperature range[22]. We believe, therefore, that the temperature dependence of the force-detected EPR signal is mainly due to the changing relaxation times, T_1 and T_2. Assuming that the resonant slice is positioned at the edge of the sample ($z = 0$), and that the sample is much thicker than the resonant-slice thickness and has a constant cross-sectional area A, we obtain the peak EPR force as

$$\begin{aligned} F &= \int_0^\infty \Omega M_0 \frac{\partial}{\partial \omega}\left[\frac{\gamma^2 B_1^2 T_1 T_2}{1+\{\gamma[B_0(0)+Gz]-\omega\}^2 T_2^2+\gamma^2 B_1^2 T_1 T_2}\right]_{\omega=\gamma B_0(0)} GA\,dz \\ &= \frac{\Omega M_0 A \gamma B_1^2 T_1 T_2}{1+\gamma^2 B_1^2 T_1 T_2}. \end{aligned} \tag{3.2}$$

For B_1 values that are not too large, F is expected to increase as the relaxation times become longer at lower temperatures[23], consistent with the result in Fig. 3.3.

3.2.3 Observation of hyperfine splitting

For the low-dopant-concentration sample, additional features were observed in the spectrum. Figure 3.4 shows the force-detected EPR spectrum for FM cyclic saturation at $T = 10$ K. The peak deviation $\Omega/2\pi$ was 10 MHz and the signal was averaged over eight B_0 sweeps to increase the signal-to-noise ratio. The spectrum shows two separate bipolar EPR lines spaced by 42 G. The origin of the two lines is the hyperfine interaction between the electron spins and phosphorus nuclear spins[24]. It is well known that at low temperature

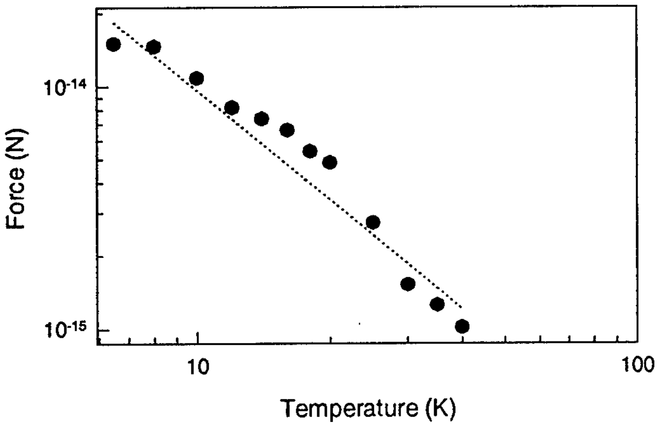

Figure 3.3: Temperature dependence of the force-detected EPR signal of the high-concentration sample. For reference, the dotted line shows a slope of $T^{-1.5}$.

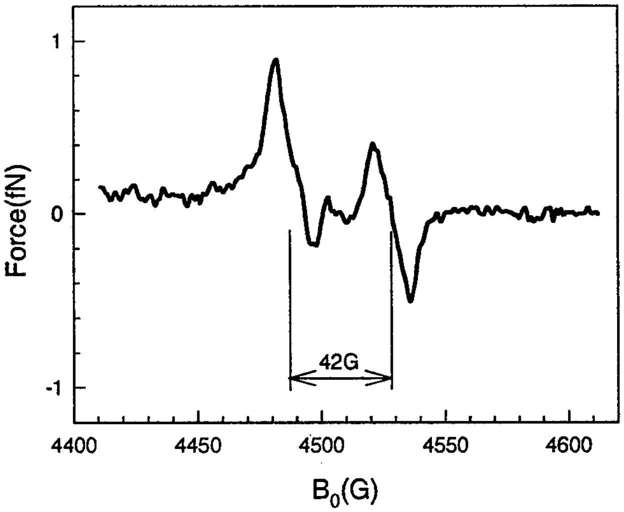

Figure 3.4: Force-detected EPR spectrum of the low-concentration sample using FM cyclic saturation for $T = 10$ K and $\Omega/2\pi = 10$ MHz. The 42-gauss spacing between the two bipolar features is due to ^{31}P hyperfine splitting.

and at low doping concentration, the unpaired electron spin from the donor atom is localized on the donor atom, allowing the hyperfine splitting to be revealed[25]. (In contrast, for the high-concentration sample, the observed EPR corresponds to conduction electrons[22].)

The peak-to-peak force is plotted as a function of temperature in Fig. 3.5. For temperatures above 10 K, the EPR force increased rapidly as the temperature decreased. It showed stronger temperature dependence, $\sim T^{-3}$, than for the high-concentration sample. This is likely due to stronger temperature dependence of both M_0 and the relaxation times. Unlike the high-concentration sample, the paramagnetism of electrons localized on donor atoms obeys the Curie-law temperature dependence, $M_0 \sim T^{-1}$. It is also known that T_1 increases as $\sim T^{-n}$, where n is in the rage of 7 to 9, at low temperature[26, 27]. The strong temperature dependence of M_0 and T_1 results in the rapid increase of the force as expected from Eq. (3.2). For temperatures below 10 K, the EPR force decreased as the temperature decreased. This cannot be explained simply from Eq. (3.2). However, in this temperature range, T_1 becomes comparable to the time scale of $1/f_c$[26, 27], which prevents the magnetization from reaching the steady state value in Eq. (2.18) when it is modulated at f_c. This results in a smaller EPR force than expected by Eq. (3.2), suppressing the signal at lower temperatures.

3.2.4 Interrupted cyclic adiabatic inversion

When T_1 is long compared with $1/f_c$, cyclic saturation is not an effective way to generate the cantilever vibration. In this situation, an alternative way to drive the cantilever is using interrupted cyclic adiabatic inversion[28]. This is performed by applying frequency and amplitude modulation of B_1 as shown in Fig. 3.6. During the inversion cycle, the magnetization is in-

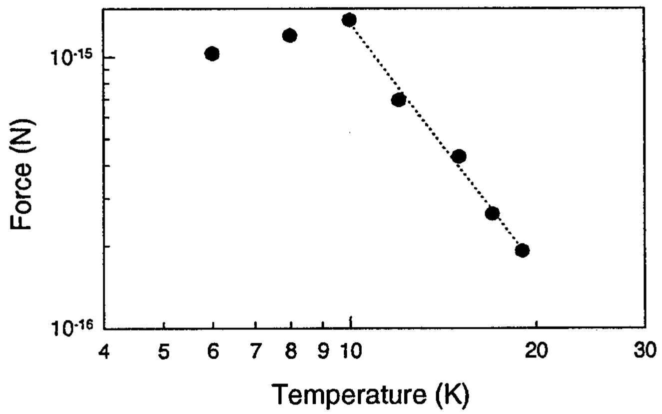

Figure 3.5: Temperature dependence of the force-detected EPR signal for the low-concentration sample. For reference, the dotted line indicates a slope of T^{-3}.

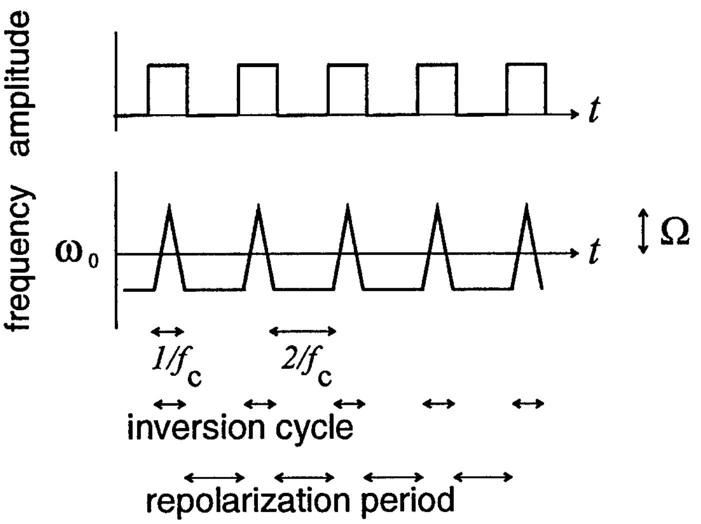

Figure 3.6: Amplitude and frequency modulation pattern used for interrupted cyclic adiabatic inversion.

verted down and then up by manipulating the direction of the effective field $\mathbf{B}_{\text{eff}}(t) = [B_0 - \omega(t)/\gamma]\hat{\mathbf{z}} + B_1\hat{\mathbf{x}}$ in the rotating frame[28][3] ($\hat{\mathbf{z}}$ and $\hat{\mathbf{x}}$ are the unit vectors in the rotating frame). This generates an oscillatory magnetic force on the cantilever. Between inversion cycles, a repolarization period lasting two cantilever cycles is inserted to ensure that the magnetization does not die out over many cycles of inversion. This method of manipulating the mag-

---

[3] See Section 2.5.2

netization works only if T_1 is comparable to or longer than $1/f_c$; if T_1 is too short, FM cyclic saturation results. The two cases should be distinguished by different shapes of the EPR force spectrum, since the cyclic adiabatic inversion has a unipolar spectral response with the maximum force obtained when the resonant slice is in the middle of the sample. Figure 3.7 shows the EPR force spectrum for the low-concentration sample obtained with this technique at $T = 6.5$ K with $\Omega/2\pi = 10$ MHz. The spectrum was averaged over eight sweeps. It shows two peaks separated by 42 G, corresponding to the two hyperfine lines. Each hyperfine line shows a single positive peak, indicating that the magnetization is indeed modulated by the adiabatic inversion. A small peak between the two main peaks is also visible and is due to pairs of dopant atoms[29].

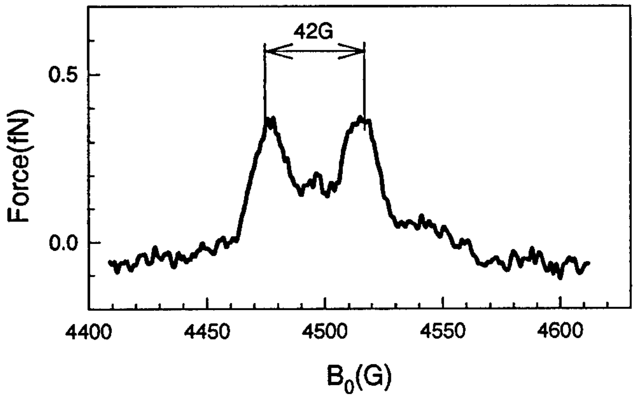

Figure 3.7: Force-detected EPR spectrum of the low-concentration sample for interrupted cyclic adiabatic inversion for $T = 6.5$ K and $\Omega/2\pi = 10$ MHz.

Chapter 4

E' Centers in SiO_2

This chapter describes force-detected EPR experiments investigating singly-occupied dangling bond defects (E' centers) in vitreous silica. This type of sample is important because similar dangling bond defects can act as trapping sites in silicon devices. Furthermore this spin system is the leading candidate for our initial single spin detection experiments because the spin-lattice relaxation time can be very long at low temperatures ($>$ 1 second), hopefully allowing cyclic adiabatic inversion to be performed coherently for times long enough for signal measurement.

In previous EPR-MRFM experiments[2, 15, 16, 30, 31, 32], including the one described in the previous chapter, modulation of the sample magnetization has been accomplished by cyclic saturation using modulation of the microwave magnetic field B_1 and/or modulation of the polarizing field B_0[2].[1] Cyclic saturation implicitly depends on having an ensemble of spins whose relaxation time is much shorter than the modulation period, allowing the magnetization to saturate and recover nearly instantaneously as the sample

---

[1] The exception is the use of the interrupted cyclic adiabatic inversion described in Section 3.2.4.

is driven in and out of resonance. Since the concept of saturation relies on the behavior of an ensemble, cyclic saturation is not a suitable technique for future MRFM experiments directed towards the detection of individual electron spins.

Cyclic adiabatic inversion, on the other hand, should be extendable to the single-spin level. In cyclic adiabatic inversion, the spin magnetization is aligned either parallel or anti-parallel to the effective field in the rotating frame while the direction of the effective field is periodically inverted by modulating the frequency of the B_1 field. For cyclic adiabatic inversion to be effective, the rotating frame relaxation time[29] must be long enough for a large number of inversion cycles to be completed, allowing a measurable cantilever vibration to build up.

Achieving a sufficiently long relaxation time is problematic for electron spins at room temperature since relaxation times are commonly in the microsecond or nanosecond range. At low temperature, however, relaxation times are much longer and a number of electron spin systems exhibit sufficiently slow relaxation. We have chosen to investigate a particularly attractive system: E' centers in vitreous silica. E' centers are defect sites characterized by singly occupied silicon orbitals[33]. For spin densities on the order of 10^{17} cm^{-3}, E' centers are known to have T_1 relaxation times on the order of seconds at temperatures as high as 5–10 K[34]. Such long relaxation times are well suited for cyclic adiabatic inversion experiments.

The work in this chapter serves several purposes. First, we demonstrate that cyclic adiabatic inversion can indeed be used with an electron spin system to generate a detectable oscillating force. After describing basic MRFM signals from E' centers, we show measurements of non-equilibrium magnetization states due to nutation and spin echoes. Finally, we study the relaxation behavior of E' centers during cyclic adiabatic inversion and measure the rate of magnetization decay as a function of the applied B_1 field. While the experiments presented here were performed using a micron-size sample containing millions of spins, we believe that the magnetization decay results, in particular, will be useful for planning future single spin experiments. Related experiments on bulk samples have been carried out using a conventional EPR spectrometer modified to detect adiabatic rapid passage signals[35, 36].

4.1 Force detected EPR

4.1.1 Experiment

The experiments were performed using the low-temperature magnetic resonance force detection apparatus used for the experiments described in the previous chapter. The sample material was synthetic vitreous silica (Spectrosil) that was irradiated by ^{60}Co γ-rays (4.4×10^8 rad) to produce E' centers.[2] The spin concentration was measured to be $3.5\times10^{16}/\mathrm{cm}^3$ using a standard spin-counting technique[35, 36]. The spin-lattice relaxation time T_1 was 1.5 s at 5 K. A sample piece with approximate dimensions 50μm $\times 50\mu$m $\times 5\mu$m was glued onto a commercial single-crystal-silicon cantilever[10] with a spring constant $k \simeq 0.07$ N/m and a mechanical-resonant frequency $f_c \simeq 5.46$ kHz (with the sample loaded). Angstrom-scale motion of the cantilever was monitored by a fiber-optic interferometer[9] and synchronously detected with a lock-in amplifier. In order to speed up the cantilever response time, damping feedback was applied to the cantilever using a piezoelectric element[11, 12, 13].

The sample was positioned 200 μm above the center of a microstripline resonator[19, 20] that produced a microwave field B_1 at $\omega/2\pi = 12.6$ GHz. The input power to the resonator ranged from 4 to 140 mW, corresponding

---

[2] Thanks to D. L. Griscom for generously providing this material.

to a B_1 strength of 0.23 to 1.35 G. The polarizing field B_0 was a combination of the homogeneous field from a superconducting magnet and the inhomogeneous field ($\sim$ 2300 G) produced by a permanent magnet located 800 μm away from the sample. The permanent magnet created a field gradient of 2 G/μm and served to generate a magnetic force on the sample. All experiments were performed at low temperature (5–10 K).

4.1.2 Cyclic adiabatic inversion

An oscillatory magnetic force from the resonant spins is generated by a "probe sequence", which consists of frequency modulation of the microwave field such that $\omega(t) = \omega_0 + \Delta\omega(t)$, where $\omega_0 = \gamma B_0$. Starting with $\Delta\omega(0) = -2\pi \times 10$ MHz $\equiv -\Omega$, the microwave field is switched on and the frequency is modulated such that $\Delta\omega(t) = -\Omega \cos(2\pi f_c t)$. After several thousand cycles (t = 0.4 s), the microwave field is switched off. Provided that the adiabatic condition (2.21) is satisfied during the probe sequence, this sequence induces cyclic inversion of the resonant magnetization $\mathbf{M}$, which follows the direction of the rotating frame effective field as described in Section 2.5.2. Consequently, the longitudinal component of $\mathbf{M}$ oscillates at a frequency f_c, causing the cantilever to vibrate.

Figure 4.1(a) shows the cantilever-vibration amplitude during a typical probe sequence obtained at 5.2 K using a microwave input power of 4 mW (B_1 = 0.23 G). Damping feedback was set to give a cantilever response time of approximately 25 ms and a lock-in time constant of 3 ms was used. The signal was averaged over roughly 30 probe sequences, with 4 seconds between successive sequences to allow the spins to repolarize. As shown in Fig. 4.1(a), the cantilever vibrated in response to the probe sequence and a peak vibration amplitude of $\sim$ 1 Å-rms was achieved approximately 25

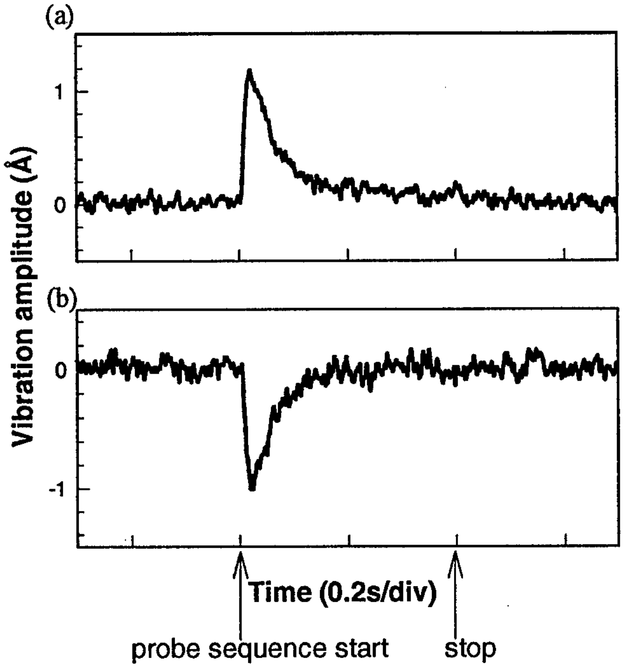

Figure 4.1: (a) Time dependence of the cantilever-vibration amplitude. The start and stop of the probe sequence are indicated by arrows. The probe sequence consists of frequency modulation to the microwave field such that $\Delta\omega(t) = -\Omega\cos(2\pi f_c t)$, inducing cyclic adiabatic inversion of the electron spin magnetization. The peak frequency deviation $\Omega/2\pi$ was 10 MHz. (b) Inverted cantilever response obtained when sample magnetization was adiabatically inverted by a frequency ramp before the probe sequence.

ms after the start of the sequence. After the initial peak, the amplitude decayed exponentially with a decay time constant of approximately 55 ms. This indicates that **M** decayed in magnitude while it was modulated by the probe sequence. Taking into account the cantilever response time and lock-in time constant, we estimate the decay time constant of the magnetization to be 25 ms. This magnetization decay will be discussed further in Section 4.3.

In order to verify that frequency modulation of B_1 indeed causes adiabatic inversion of **M**, we applied a single additional frequency ramp prior to the probe sequence. The microwave field was switched on with $\Delta\omega = \Omega$ and then ramped to $\Delta\omega = -\Omega$. This ramp should adiabatically invert **M**. The same probe sequence as before was then applied: $\Delta\omega(t) = -\Omega\cos(2\pi f_c t)$. As shown in Fig. 4.1(b), cantilever vibration was excited, but with opposite phase compared to the case in which only the probe sequence was applied. This indicates that the magnetization before the start of the probe sequence was indeed adiabatically inverted by the preparatory frequency ramp.

An EPR spectrum can be obtained by measuring the cantilever response to the probe sequence while sweeping the field from the superconducting magnet. Figure 4.2 shows the peak amplitude of the cantilever vibration as a function of B_0. The lineshape is symmetric with a width of 12 G. This width, considerably broader than the intrinsic linewidth for E' centers[37], results from the use of the large gradient with a sample of finite thickness and from the large FM deviation $\Omega/2\pi = 20$ MHz ($\Omega/\gamma \simeq 7.1$ G).

4.1.3 Steady-state magnetization during cyclic adiabatic inversion

While the peak amplitude of the cantilever vibration reflects the state of the magnetization just prior to the probe sequence, it is also interesting

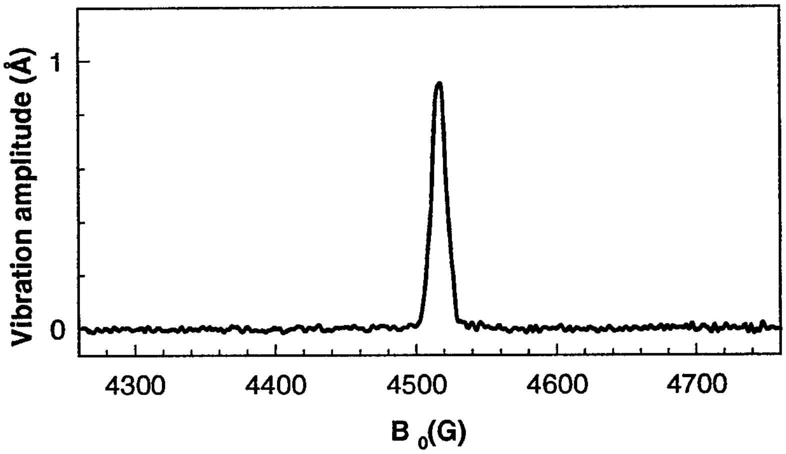

Figure 4.2: Force-detected EPR spectrum. The peak amplitude of the cantilever vibration is plotted as a function of the polarizing field strength. The peak deviation $\Omega/2\pi$ was 20 MHz, the cantilever response time was $\sim$ 10 ms, and the signal was averaged over 50 scans. The peak appears when $B_0 = \omega_0/\gamma$ at the sample position.

to investigate the steady-state cantilever vibration achieved at the end of the probe sequence. In Fig. 4.1, the cantilever-vibration amplitude decays almost to zero by the end of the probe sequence; however, we found that this is not always the case and that the steady-state amplitude depends on the strengths of both B_0 and B_1. Figure 4.3(a) shows the cantilever-vibration amplitude during the probe sequence with a microwave input power of 52 mW ($B_1 = 0.82$ G). After the initial excitation, the vibration amplitude decays and reaches a steady-state value of approximately 0.3 Å-rms.

The steady-state value of cantilever-vibration amplitude changes sign as the external field is swept, leading to the bipolar spectrum[3] shown in Fig. 4.3(b). The cantilever-vibration amplitude reaches a positive steady-state value when B_0 is slightly above resonance ($B_0 - \omega/\gamma > 0$), and a negative value when B_0 is below resonance ($B_0 - \omega/\gamma < 0$). These results can be understood in terms of spin dynamics in the rotating frame. In the steady state, $\mathbf{M}$ is locked parallel to $\mathbf{B}_{\text{eff}}$ if $B_0 - \omega/\gamma > 0$ and antiparallel to $\mathbf{B}_{\text{eff}}$ if $B_0 - \omega/\gamma < 0$[29]. When cyclically modulated by the FM sequence, the magnetization antiparallel to $\mathbf{B}_{\text{eff}}$ generates an oscillatory force that is 180° out of phase with respect to that generated when $\mathbf{M}$ is parallel to $\mathbf{B}_{\text{eff}}$.

4.2 Nonequilibrium magnetization measurements

4.2.1 Nutation

The initial peak amplitude of the cantilever vibration reflects the state of longitudinal magnetization at the start of the probe sequence. This fact can

---

[3] The small background signal of ~ 0.02 Å observed for field values far from resonance is due to spurious microwave-feedthrough effects.

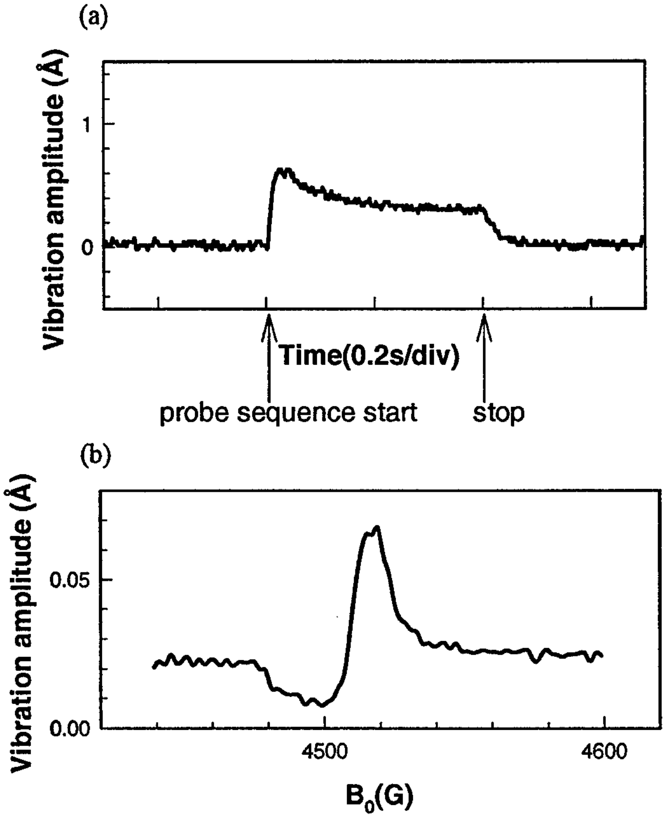

Figure 4.3: (a) Time dependence of the cantilever-vibration amplitude with a microwave input power of 52 mW ($B_1 = 0.82$ G). The vibration amplitude reaches a steady-state value by the end of the probe sequence. (b) The steady-state cantilever-vibration amplitude as a function of the B_0 strength. Absolute vibration amplitude is smaller than in (a) because greater damping feedback was used.

be used to probe nonequilibrium states of magnetization[28]. Here, we show nutation and spin echo experiments.

Nutations can be measured by applying a microwave pulse of width t_p before the probe sequence. The pulse causes resonant spins to precess about $\mathbf{B}_{\text{eff}} = B_1\hat{\mathbf{x}}$ in the rotating frame with an angular frequency γB_1. As a result, the longitudinal component of $\mathbf{M}$ is given by $M_z = M_0 \cos(\gamma B_1 t_p)$, where M_0 is the thermal equilibrium magnetization. The probe sequence following the pulse generates an oscillatory force proportional to M_z that excites the cantilever vibration. Figure 4.4 shows the peak cantilever-vibration amplitude as a function of the microwave pulse width t_p. A microwave input power of 130 mW was used for the pulse and 4 mW was used for the probe sequence. The signals show an oscillation with a 270 ns period and gradually decreasing amplitude. The oscillation is superimposed on a positive offset. Since the oscillation period corresponds to $2\pi/(\gamma B_1)$, the amplitude of B_1 for the 130 mW microwave pulse is determined to be 1.3 G. This result calibrates the B_1 field at the location of the sample generated by the microstripline resonator.

The positive offset is due to off-resonance spins in the sample (*i.e.*, due to the field gradient and the finite sample thickness). With the frequency deviation $\Omega/2\pi = 10$ MHz used for the probe sequence, spins that are off-resonance by $|\Delta B| = \Omega/\gamma \simeq 3.6$ G still contribute to the force signal significantly[17, 28].[4] Rather than precessing about $B_1\hat{\mathbf{x}}$, these off-resonance spins will precess in a cone about $\mathbf{B}_{\text{eff}} = B_1\hat{\mathbf{x}} + \Delta B\hat{\mathbf{z}}$, which is tilted 70° from the $\hat{\mathbf{x}}$ axis (for $B_1 = 1.3$ G). Spins precessing in this cone will always have a positive z component, leading to a positive offset in the nutation.

The decay of the nutation is also attributed to off-resonance spins. For the

---

[4] See Section ??.

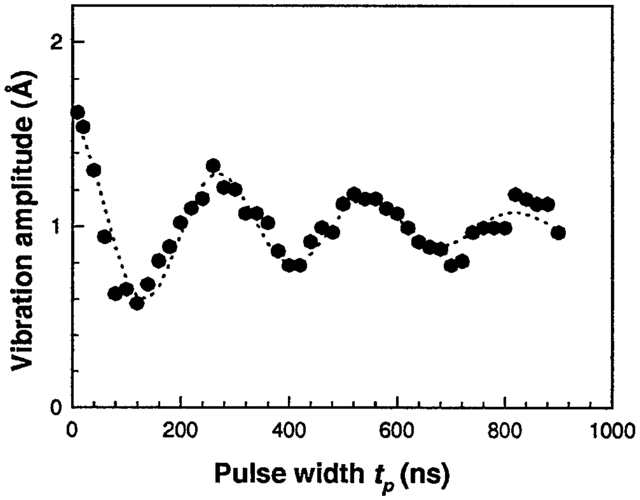

Figure 4.4: Force-detected nutation signal. The peak amplitude of the cantilever vibration is plotted as a function of the width of a microwave pulse t_p applied prior to the probe sequence. A microwave power of 130 mW was used for the pulse, and 4 mW was used for the probe sequence. The dotted line is a fit to a damped cosinusoidal oscillation with an offset.

off-resonance case, the precession frequency $\gamma|\mathbf{B}_{\text{eff}}|$ differs from γB_1, causing spins in different regions of the sample to precess at different rates. The interference caused by a range of precession frequencies leads to a gradual decay of the oscillation amplitude in the total nutation signal. This effect dominates over the decay due to spin-spin relaxation processes (T_2 decay), which are related to the much smaller homogeneous broadening.

4.2.2 Spin echoes

Spin echoes play an important role in many magnetic resonance techniques. In conventional magnetic resonance, a $\pi/2$-τ-π pulse sequence is used to generate an echo. After the $\pi/2$ pulse, the spread in precession rates of the magnetization due to local fields and the inhomogeneity of B_0 causes a reversible decay of transverse magnetization. When a π pulse is applied after a time τ, spins are refocused at $t = 2\tau$, leading to an echo, the size of which is given by $M_0 \exp(-2\tau/T_2)$. Since the MRFM technique described here is sensitive to the longitudinal component of $\mathbf{M}$, the spin echo is detected by applying a $\pi/2$-τ-π-τ'-$\pi/2$ pulse sequence. The last $\pi/2$ pulse rotates the refocused magnetization to the longitudinal direction, which is mechanically detected by a subsequent probe sequence.

The experiment was carried out with the pulse sequence shown in Fig. 4.5(a). The peak amplitude of the cantilever vibration was measured while changing the time interval τ_A between the first $\pi/2$ pulse and the π pulse and keeping a fixed time interval τ_B between the two $\pi/2$ pulses. This has the effect of "walking" the echo through the last $\pi/2$ pulse. The widths of the $\pi/2$ and π pulses were 70 ns and 140 ns, respectively. Figure 4.5(b) shows the result for $\tau_B = 1$ μs. A peak is observed at $\tau_A \simeq 500$ ns $= \tau_B/2$, corresponding to the refocus condition for a spin echo.

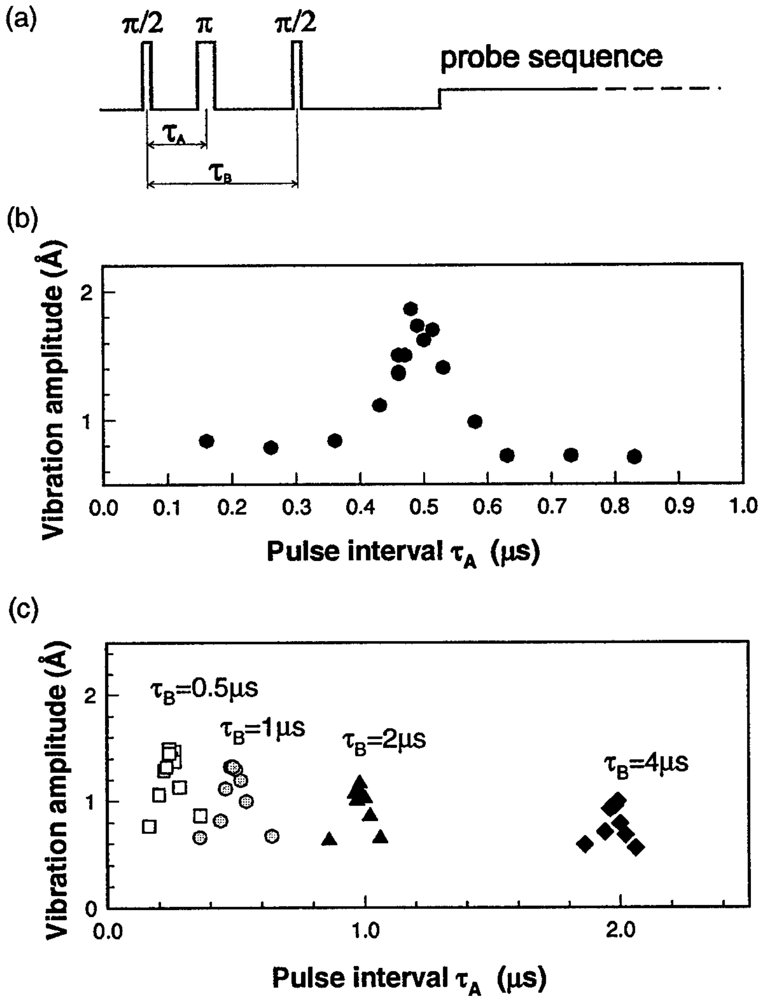

Figure 4.5: (a) Pulse sequence used for the spin echo experiment. A microwave power of 130 mW was used for the pulses, and 4 mW was used for the probe sequence. Widths of $\pi/2$ and π pulses were 70 ns and 140 ns, respectively. (b) The peak amplitude of the cantilever vibration as a function of τ_A, with a fixed $\tau_B = 1$ μs. A peak appears when $\tau_A \simeq \tau_B/2$, corresponding to a spin echo. (c) Spin echoes observed with various τ_B. The amplitude of the spin echoes gradually decreases as τ_B increases.

The results for various τ_B are shown in Fig. 4.5(c). In each case, a peak appears when $\tau_A \simeq \tau_B/2$, representing spin echoes at various time intervals. With increasing τ_B, the peak height gradually decreases, presumably due to the T_2 decay as in conventional spin echo experiments[38]. The observed decay time indicates a T_2 on the order of 5 μs. For comparison, T_2 of 2.1 μs has been measured previously using conventional techniques on a silica sample containing a slightly higher concentration of spins[39].

4.3 Magnetization decay during adiabatic inversion cycles

One key issue for the force detection of electron spins is the relaxation rate of the spins while they are subjected to cyclic adiabatic inversion. As mentioned earlier, the magnetization decays during the force detection sequence (Fig. 4.1). For a successful MRFM experiment, the spin magnetization must last long enough to excite the cantilever vibration to a detectable level. The decay of magnetization can be due to a variety of effects, including spin-lattice relaxation in the rotating frame, violation of the adiabatic condition, and spin-spin relaxation processes.

As shown in Fig. 4.6, the spin-lattice relaxation time in the rotating frame $T_{1\rho}$ can be measured by staying spin-locked on resonance for a variable time τ_{lock} before the probe sequence. The data in Fig. 4.6 shows the peak cantilever-vibration amplitude as a function of the spin-locking time for $B_1 = 0.23$ G. The signal decreases exponentially towards a steady-state value as τ_{lock} increases. The decay time constant was estimated to be $T_{1\rho} \simeq 190$ ms, in reasonable agreement with the value measured using conventional techniques[35, 36].

The observed magnetization decay time constant during repeated adiabatic reversals was found to be significantly shorter than $T_{1\rho}$. For example, the observed decay time constant in Fig. 4.1 was only 25 ms. To further investigate this effect, we used the trapezoidal FM waveform shown in Fig. 4.7, instead of the usual sinusoidal frequency modulation. The slope of the linear frequency ramp in the waveform was set such that $|\gamma^{-1}d\omega/dt| = |d\mathbf{B}_{\text{eff}}/dt| = 3.0 \times 10^6$ G/s.

The frequency modulation of B_1 causes an oscillation of longitudinal mag-

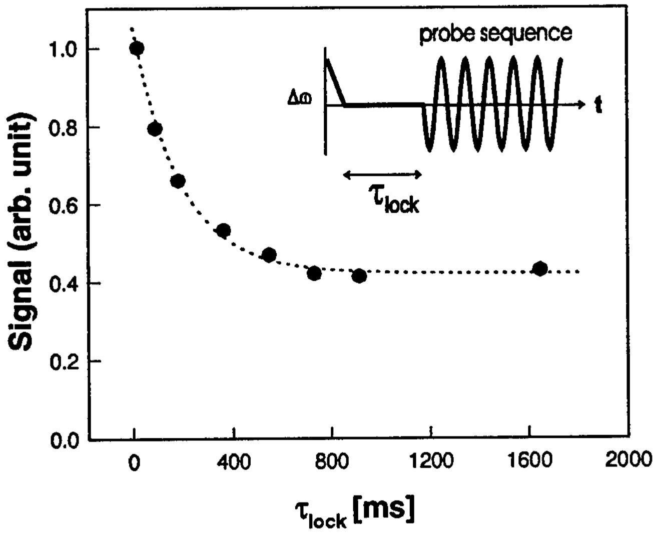

Figure 4.6: The peak amplitude of the cantilever vibration as a function of the spin-lock time $\tau_{\rm lock}$ before the probe sequence. The dotted line is a fit to an exponential decay with an offset. The signal decays with a time constant $T_{1\rho} \simeq 190$ ms. The inset shows the FM waveform used for the measurement.

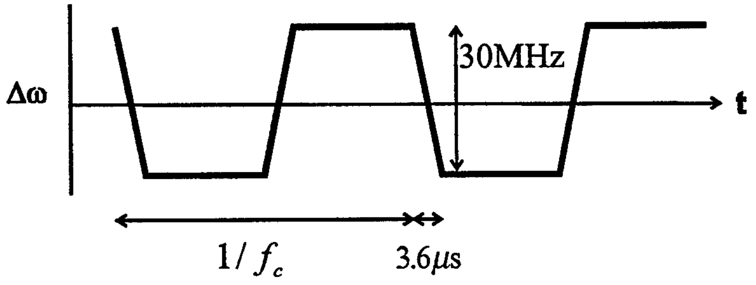

Figure 4.7: Trapezoidal FM waveform used to study magnetization decay. The slope of the trapezoid is set such that $|\gamma^{-1} d\omega/dt| = |d\mathbf{B}_{\text{eff}}/dt| = 3.0 \times 10^6$ G/s.

netization such that

$$M_z(t) = \tilde{M}(t)\frac{\Delta\omega(t)}{\sqrt{(\gamma B_1)^2 + [\Delta\omega(t)]^2}}, \tag{4.1}$$

where $\tilde{M}(t)$ is the magnitude of the magnetization, which varies slowly compared to the 5.5 kHz modulation frequency. The first-harmonic Fourier component (in rms) of $M_z(t)$ is approximately given by $(2\sqrt{2}/\pi)\tilde{M}(t)$ for a $\Delta\omega(t)$ with a trapezoidal waveform. If $\tilde{M}(t)$ slowly decays such that $\tilde{M}(t) = M_0 \exp(-t/\tau_m)$, the rms amplitude of the resulting oscillatory force is given by

$$\tilde{F}(t) = \frac{2\sqrt{2}}{\pi} M_0 G \exp\left(-\frac{t}{\tau_m}\right) + \tilde{F}_b, \tag{4.2}$$

where G is the field gradient and $\tilde{F}_b$ is a small background oscillatory force that is included to account for spurious feedthrough of the microwave modulation.

The rms amplitude of the cantilever response $\tilde{A}(t)$ is given by the convolution

$$\tilde{A}(t) = \int_0^t h(t')\tilde{F}(t-t')dt', \tag{4.3}$$

where

$$h(t) = \frac{Q_{\text{eff}}}{k\tau_c} \exp\left(-\frac{t}{\tau_c}\right) \tag{4.4}$$

is the impulse response function of the cantilever. Here, Q_{eff} and $\tau_c = Q_{\text{eff}}/\pi f_c$ are the effective Q factor and $1/e$ response time of the cantilever, respectively, taking into account the damping feedback. Equations (4.2) and (4.3) lead to the cantilever response

$$\tilde{A}(t) = \frac{Q_{\text{eff}}}{k}\left\{\frac{2\sqrt{2}}{\pi}\frac{M_0 G}{1-\tau_c/\tau_m}\left[\exp\left(-\frac{t}{\tau_m}\right) - \exp\left(-\frac{t}{\tau_c}\right)\right] + \tilde{F}_b\left[1 - \exp\left(-\frac{t}{\tau_c}\right)\right]\right\}. \tag{4.5}$$

A typical cantilever response for the trapezoidal modulation sequence is shown in Fig. 4.8. The observed cantilever response was fit to Eq. (4.5) using

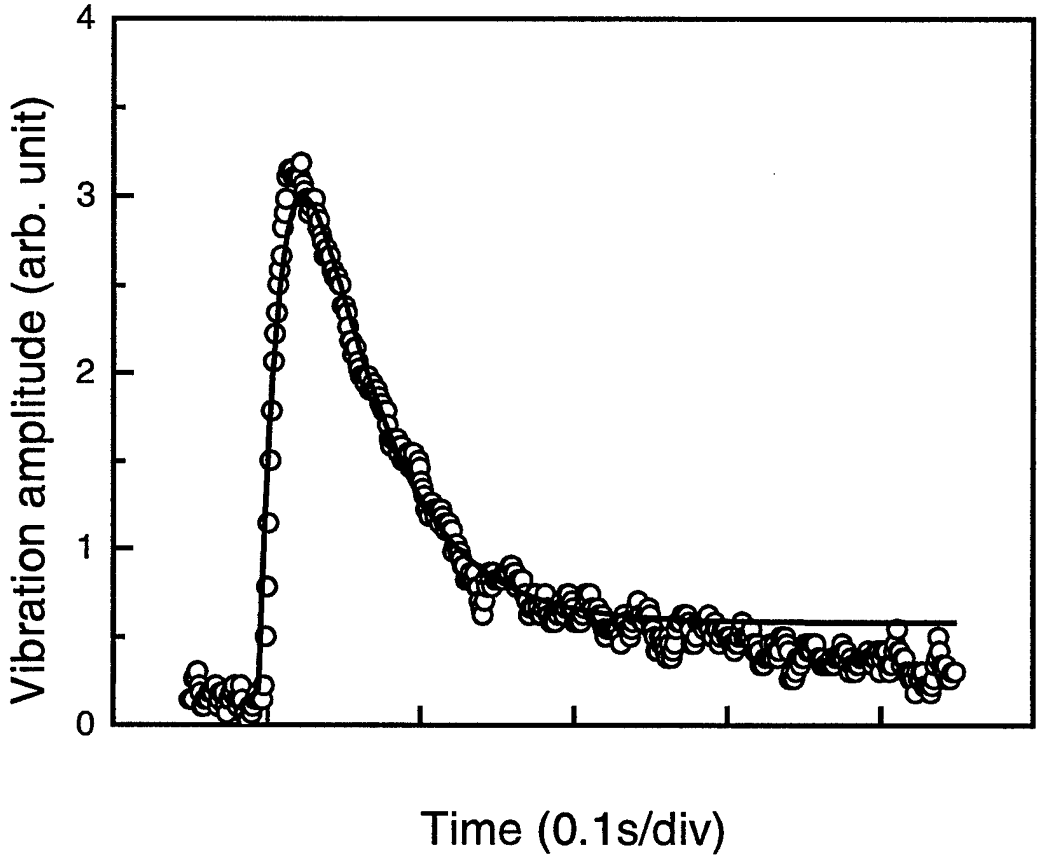

Figure 4.8: A typical cantilever response for the trapezoidal modulation. The line is a fit using the function in Eq. (4.5). The magnetization decay time τ_m is found to be 46 ms in this case. $B_1 = 1.35$ G.

three adjustable parameters M_0, τ_m, and $\tilde{F}_b$. The other parameters were determined independently. For Fig. 4.8, we found that $M_0 = 2.4 \times 10^{-13}$ emu $= 2.6 \times 10^7 \mu_B$, where μ_B is the Bohr magneton, and $\tau_m = 46$ ms. The uncertainty in these results is estimated to be on the order of 10%.

Magnetization decay time constants τ_m obtained for various B_1 strengths are plotted in Fig. 4.9. Values of adiabaticity parameter $\gamma B_1^2/|d\mathbf{B}_{\text{eff}}/dt|$, defined as the ratio of the right hand side and left hand side of (2.21), are also indicated in the figure. It was found that τ_m increases as B_1 increases, suggesting that the magnetization decay is due to the violation of the adiabatic condition, $|d\mathbf{B}_{\text{eff}}/dt| \ll \gamma B_1^2$. At the maximum B_1, where $\gamma B_1^2/|d\mathbf{B}_{\text{eff}}/dt| \simeq 10$, $\tau_m = 46$ ms and it appears to be reaching a plateau, indicating that loss due to non-adiabaticity is no longer dominant. Nevertheless, τ_m is still significantly shorter than $T_{1\rho} \simeq 190$ ms. An additional mechanism for magnetization decay, such as rotating frame cross-relaxation processes among spins in inhomogeneously broadened lines, might be responsible for the relatively short τ_m[35, 36].

The magnetization decay time during cyclic adiabatic inversion may have implications for future single spin experiments since the spin lifetime determines the detection bandwidth that must be used. The spin lifetime of ~ 50 ms implies the detection bandwidth of ~ 20 Hz. A sharp magnetic tip (50 nm radius) generates a field gradient on the order of 10 G/Å at a position ~ 150 Å below the tip. For an electron spin located at this position and undergoing cyclic adiabatic inversion, the resulting interaction force is 7×10^{-17} N-rms. To detect such a small force in a detection bandwidth of 20 Hz, a force resolution of 2×10^{-17} N/$\sqrt{\text{Hz}}$ or better is needed to achieve unity signal-to-noise ratio. Such force resolution was recently demonstrated using ultrathin single-crystal silicon cantilevers[40, 41]. Assuming that the spin relaxation time is not adversely affected by the close proximity of the magnetic

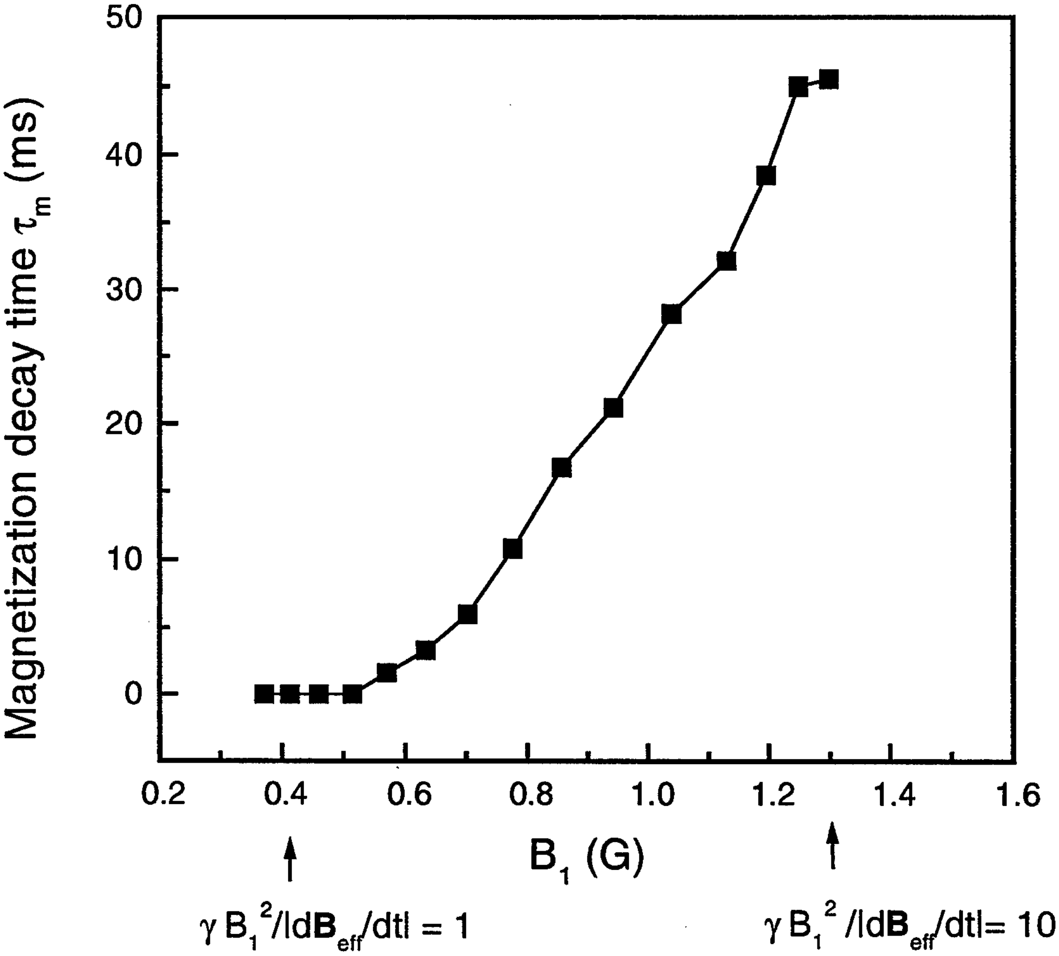

Figure 4.9: Magnetization decay time τ_m as a function of B_1. Arrows indicate values of adiabaticity parameter $\gamma B_1^2/|d\mathbf{B}_{\text{eff}}/dt|$.

tip, the long spin lifetime of E' centers make them a suitable candidate for future single spin MRFM experiments.

Chapter 5

EPR and FMR imaging

Magnetic resonance force microscopy (MRFM) has previously been performed with the sample mounted on a micromechanical cantilever positioned close to a millimeter-size field gradient source. In this chapter, we describe an improved microscope configuration, where the gradient source consists of a magnetic tip mounted directly on the cantilever. This allows a much wider variety of samples to be investigated and greatly improves the convenience of the technique. We have used this improved microscope to compare and contrast two- and three-dimensional imaging characteristics of paramagnetic and ferromagnetic samples.

5.1 Improved MRFM setup

The design of the microscope is shown schematically in Figs. 5.1, 5.2, and 5.3. The entire system is suspended in a vacuum can with Teflon support frames to ensure adequate vibration isolation. The vacuum can fits into a liquid-helium dewer with a superconducting magnet. The microscope consists of a gradient source-cantilever combination and a sample that can be scanned in three dimensions. The gradient source is a magnetic tip (typically a 10–100 micron-size sphere) glued onto the cantilever, the motion of which is measured by a fiber-optic interferometer[9]. The sample is placed on top of a microstripline resonator[19, 20] that generates the 12-GHz microwave field B_1 used to induce magnetic resonance. The sample and resonator are mounted on a piezoelectric tube scanner.

In this design, the spatial resolution of MRFM is aimed at a micron level, requiring a total scan range on the order of 100 μm at low temperature. We used a 15-cm-long piezoelectric tube scanner to achieve this. Two tube scanners (3 inch long × 0.25 inch diameter × 0.02 inch wall-thickness)[42] were joined together to achieve a scan range of approximately 100 μm laterally (x and y) and 5 μm in the z direction at low temperature with a maximum applied voltage of ±150 V.[1] The piezoelectric tube is surrounded by an outer support tube attached to a tripod assembly, which is held with three springs against three adjustment screws. One of these screws is coupled to an external shaft for coarse adjustment of the tip-sample distance during operation[8].

In order to provide thermal conduction from liquid helium, most of the instrument, including the sample/resonator holder, the outer support tube of the scanner, and the side frame of the microscope, is made of oxygen-free high-conductivity (OFHC) copper. The copper braids, attached by soldering, connect to the bottom flange of the vacuum can immersed in liquid helium. Since the copper braid and a semi-rigid coax to provide the microwave to the resonator are attached to the sample/resonator holder on top of the 15-cm-long tube scanner, special attention is required in handling the microscope not to break the rather fragile tube scanner. One disadvantage of using such

---

[1] The scan range was calibrated by imaging a calibration grid using contact-mode atomic force microscopy.

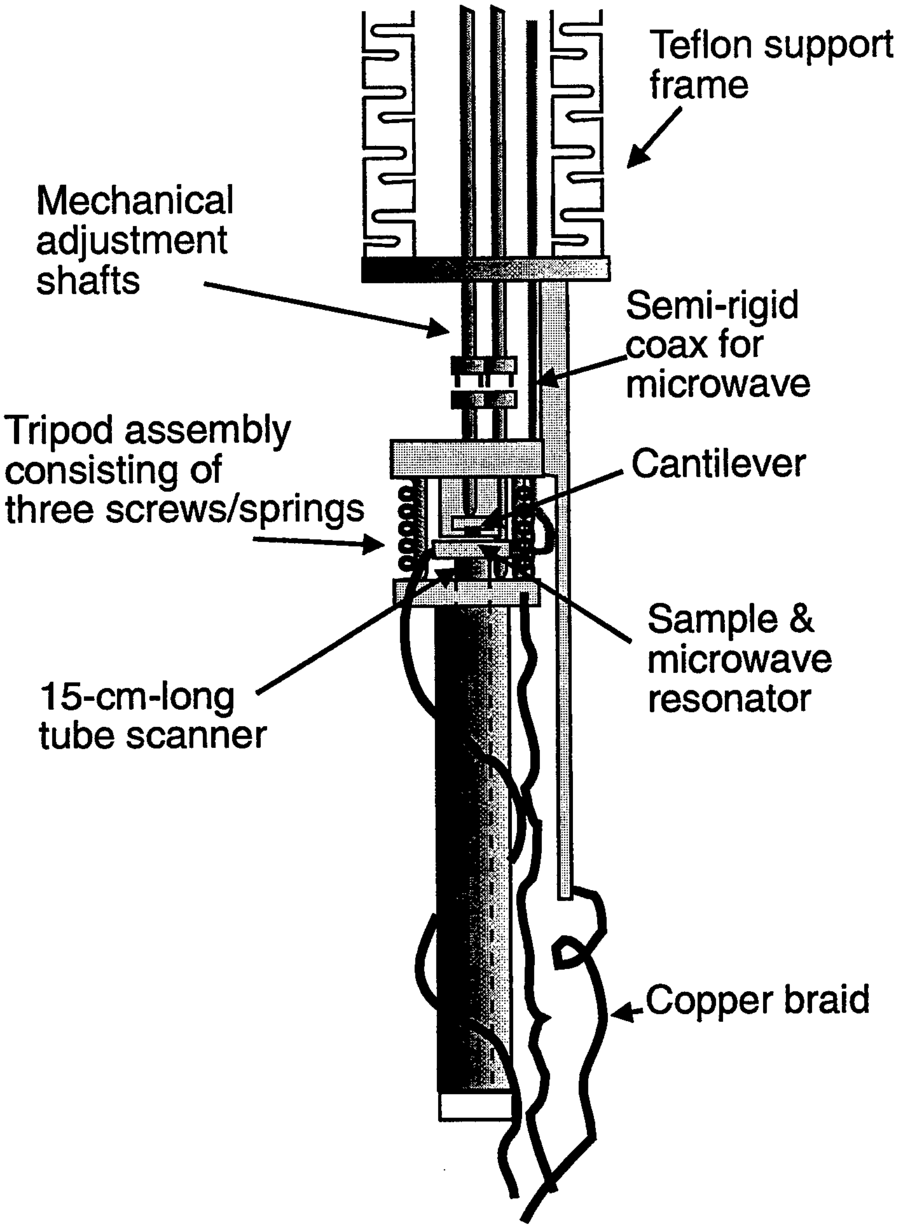

Figure 5.1: Schematic diagram of the improved low-temperature magnetic resonance force microscope. The microscope is suspended in a vacuum can that fits into a liquid-helium dewer with a superconducting magnet.

a long tube scanner is that the positioning of the sample holder is susceptible to environmental vibration coupled either directly via the support structure or through the coax and copper braid. The stability of the sample holder was estimated to be on the order of 0.1–1.0 μm in x and y, and 0.1 μm in z.

The cantilever chip is glued onto the end of a stiff stainless steel flexure beam that is deflected by a fine-pitch adjustment screw as shown in Fig. 5.2. The screw is coupled to a second external shaft. Between the screw and the flexure beam is a piezoelectric disk used to fine-adjust the z position of the cantilever relative to the fiber end. The piezoelectric disk is also used to drive the vibration of the cantilever and provide damping feedback in some cases[11, 12, 13]. The x-y position of the fiber end is adjusted at room temperature with the positioner consisting of a cylindrical flexure and adjustment screws.

Magnetic resonance in the sample is induced by the microwave field B_1 from the resonator in the presence of the static field B_0, which is a combination of the homogeneous field B_{ext} applied in the z direction by an external superconducting magnet and the inhomogeneous field B_{tip} from the magnetic tip. B_{ext} also served to magnetize the magnetic tip to its saturation magnetization.

To generate a kilohertz-frequency oscillatory magnetic force from the on-resonance spins, B_1 was frequency modulated so as to cyclically saturate the spin magnetization. The modulation frequency ω_m was chosen to be equal to the mechanical resonant frequency of the cantilever ω_c. This results in a bipolar spectral lineshape of force-detected magnetic resonance as explained in Chapter 3. The force-detected magnetic resonance signal, measured as a vibration amplitude of the cantilever, is recorded while the sample is scanned in x-y with various values of B_{ext}.

The presence of the tip on the cantilever results in some unwanted side

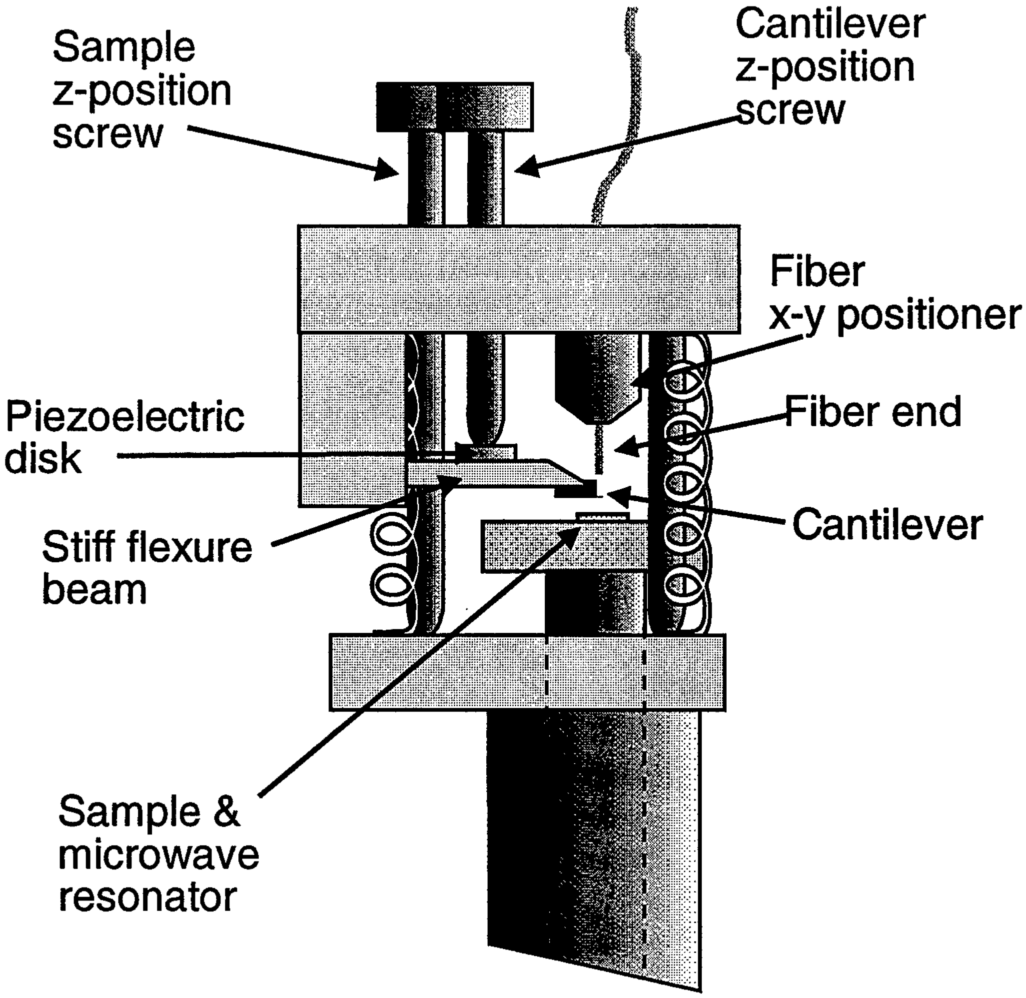

Figure 5.2: Close-up view of the microscope from the side.

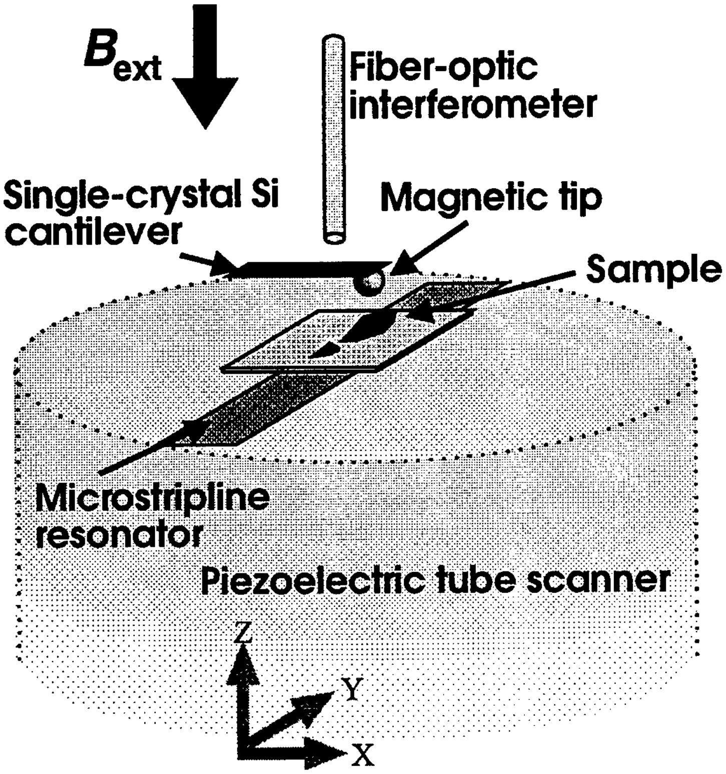

Figure 5.3: Schematic setup of the experiment.

effects observed during the x-y-B_{ext} scan. The mechanical resonant frequency of the cantilever is affected by tip-sample interaction forces and by the force/torque exerted by B_{ext}. Therefore, at each point of the x-y-B_{ext} scan, ω_c is first measured in order to set ω_m before detecting the magnetic resonance force signal. To ensure proper operation of the fiber interferometer, the cantilever-fiber spacing is corrected by a piezoelectric actuator at the base of the cantilever.

Figure 5.4 shows a block diagram of the experiment. A personal computer (PC) controls the sample position and B_{ext}. The cantilever-fiber spacing is controlled by servo electronics to maintain the proper operation of the interferometer. At each point of the scan, a calibration sequence for the cantilever frequency is first initiated. A pulse generator (HP8118A) sends pulses to open the gate to drive the cantilever vibration with the piezoelectric disk, and to activate a phase-locked loop (PLL) consisting of a lock-in amplifier (PAR124) to detect the phase error, which is fedback to the frequency control of the function generator (FG5010) driving the cantilever vibration. After the calibration sequence, the frequency modulation of the microwave generator (HP83732A) is turned on at the calibrated cantilever resonant frequency. The cantilever vibration amplitude resulting from the oscillatory force due to magnetic resonance is then measured by another lock-in amplifier (SR530) and recorded by the PC. If necessary, damping feedback to reduce the cantilever response time is used by applying a 90°-phase-shifted signal to the piezoelectric disk.

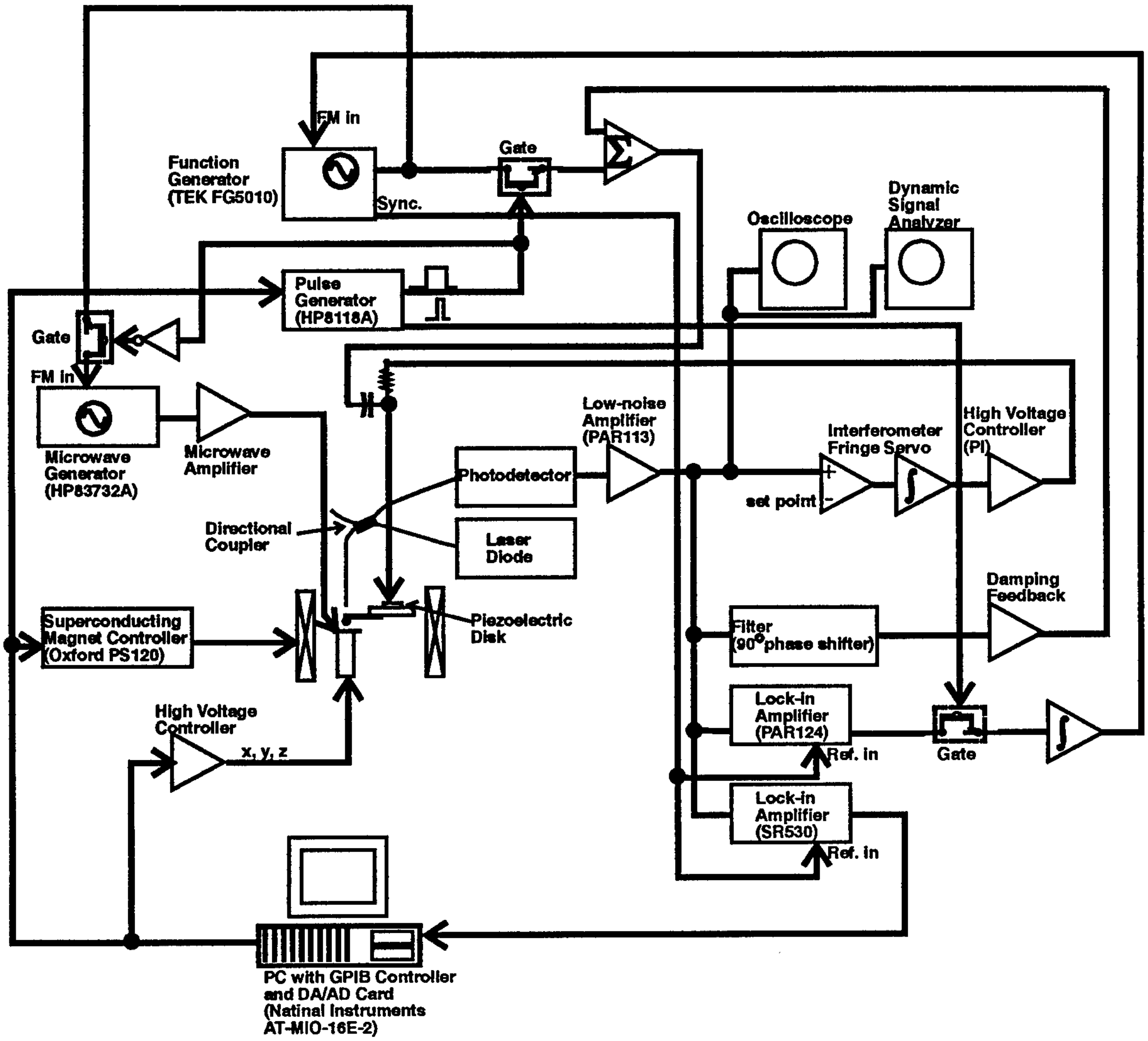

Figure 5.4: Block diagram of the experiment.

5.2 Cantilever with a magnetic tip in the external field

As a magnetic tip, we used a NdFeB sphere of ~10 μm radius,[2] a ferrite particle (irregular shape), and nickel spheres of ~10 μm and ~55 μm radii.[3] The magnetic tip was glued onto a commercial single-crystal-silicon cantilever[10]. Figure 5.5 shows optical micrographs of 10 μm and 55 μm radius nickel spheres mounted on the cantilevers.

The behavior of the cantilever with the magnetic tip is studied by measuring the dc deflection and resonant frequency of the cantilever in the applied external field. Figure 5.6 shows the dc deflection of the cantilever with a 10-μm-radius nickel sphere (Fig. 5.5(a)). The deflection increases as the field is increased in both polarities, with greatest effect at lower field (below ~3000 G).

The magnetic force acting on the magnetic tip is

$$F = MV\frac{\partial B}{\partial z}, \tag{5.1}$$

where M is the magnetization of the tip assumed to be parallel to the field B applied in the z direction and V is the volume of the tip. The cantilever is not positioned exactly at the center of the superconducting magnet, resulting in a small field gradient on the order of 10 G/cm for $B = 1000$ G. For a soft ferromagnetic sphere, M varies linearly with B up to $4\pi M_s/3$, where M_s is the saturation magnetization. For nickel, $M_s \simeq 510$ emu/cm^3 at low temperature. Since $\partial B/\partial z$ is proportional to B, the linear dependence of M on B up to $4\pi M_s/3 \simeq 2140$ G leads to $F \propto B^2$. In higher fields where M

---

[2] Available from Particle Technology, Inc., Hanover, Maryland.

[3] Available from Alfa Aester, 1-800-343-0660.

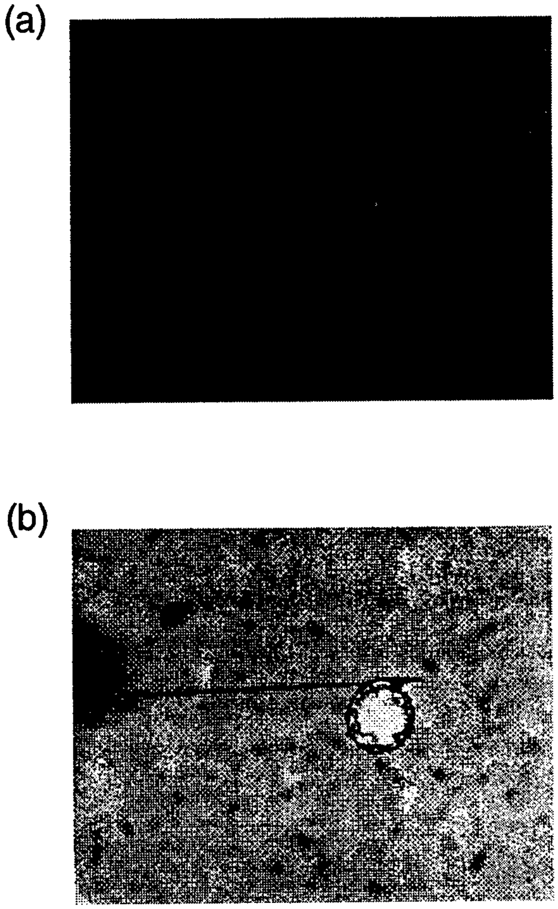

Figure 5.5: (a) Optical micrographs of the cantilever with a nickel sphere with $r \simeq 10$ μm. A pyramidal-shape silicon tip is also visible. (b) The cantilever with a nickel sphere with $r \simeq 55$ μm.

reaches a constant value of M_s, F is expected to be linear with B. The curve in Fig. 5.6 agrees qualitatively with the expected behavior.

The curve shows a little hysteresis, indicating the presence of anisotropy presumably due to imperfect spherical shape or crystalline anisotropy. If there is anisotropy, a torque also acts on the tip since the magnetization tends to align with the easy axis as well as the external field. Let θ be the angle between the easy axis and the z direction when the cantilever is not deflected, α be the angle between the easy axis and the magnetization, and φ be the angle of the cantilever deflection as shown in Fig. 5.7. In the case of the crystalline anisotropy, the total energy can be modeled as

$$E = \left[K \sin^2 \alpha - BM \cos(\theta - \alpha - \varphi) + M\frac{\partial B}{\partial z} l \sin \varphi\right] V + \frac{1}{2} k l^2 \sin^2 \varphi, \quad (5.2)$$

where K is the anisotropy factor, k and l are the spring constant and the length of the cantilever, respectively. The first term in E is the anisotropy energy, the second and the third terms are the energies in the applied field, and the last term is the potential energy of the cantilever. The cantilever deflection can be determined by minimizing E with respect to α and φ with given B and M, which is assumed to be proportional to B up to $4\pi M_s/3$. Even if B is perfectly uniform ($\partial B/\partial z = 0$), this leads to a finite deflection. For small B, we obtain $\alpha \simeq 0$ and $\varphi \propto B^2$. For large B, where M is saturated, φ reaches a constant value θ. The dc deflection shown in Fig. 5.6 is likely to be resulting from both the force due to $\partial B/\partial z$ and the torque due to the anisotropy.

Figure 5.8 shows the change of the resonant frequency as a function of the field for the same cantilever. The resonant frequency at zero field is 3.97 kHz. The frequency increases up to ~2100 G and then decreases, reaching a plateau above ~5000 G. There is also a little hysteresis due to an apparent ~600 G of coercivity.

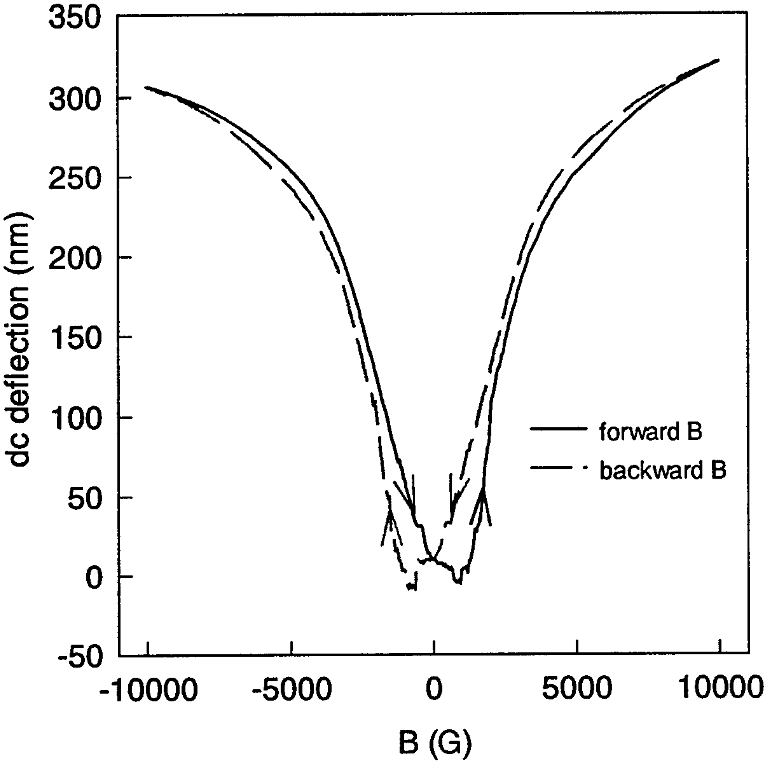

Figure 5.6: The dc deflection of the cantilever with a nickel sphere ($r \simeq 10$ μm) as the field is swept forward and backward.

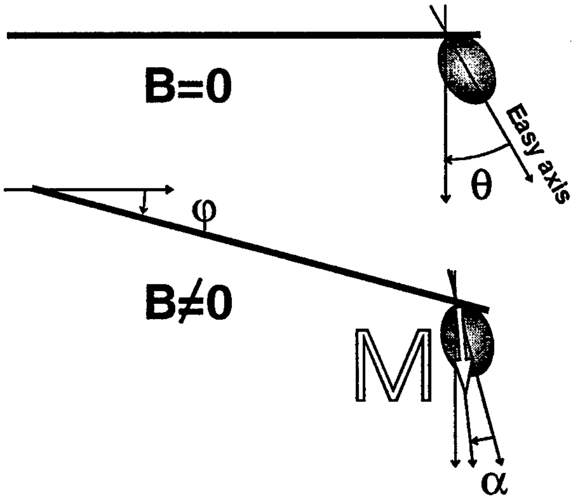

Figure 5.7: Model of the cantilever deflection.

The magnetic interaction modifies the effective spring constant of the cantilever according to

$$\Delta k = \frac{\partial F}{\partial z}, \tag{5.3}$$

which, in the absence of the anisotropy, is given by

$$\frac{\partial F}{\partial z} = MV\frac{\partial^2 B}{\partial z^2}. \tag{5.4}$$

Near the center of the superconducting magnet, which can be assumed to be a simple solenoid, this term has the effect of increasing the resonant frequency. Since both M and $\partial^2 B/\partial z^2$ are proportional to B for low field, the frequency change is expected to be proportional to B^2 up to $4\pi M_s/3 \simeq 2140$ G, beyond which it is expected to be proportional to B. The torque due to the anisotropy also has the effect of increasing the frequency, which varies as $\propto B^2$ for low field and reaches a plateau for high field. The result shown in Fig. 5.8 agrees with the expected behavior for low field. The frequency decrease in high field, however, does not agree with the expectation based on the model described in Eq. (5.2), indicating an additional mechanism affecting the resonant frequency of the cantilever.

The presence of the tip on the cantilever also has a significant effect on the quality factor of the cantilever in the field. Figure 5.9 shows Q for the cantilevers with 10 μm and 55 μm radius nickel spheres (Fig. 5.5). Q is reduced from more than 100 000 at zero field as the field is increased. The effect is more significant for the bigger sphere, for which Q is reduced to below 100 at B =10 000 G. This effect is due to micromagnetic loss caused by motion of the tip magnetization when the cantilever vibrates in the field.

5.3 EPR of phosphorus-doped silicon

As described in Chapter 3, electron paramagnetic resonance (EPR) of phosphorus-doped silicon was studied using the low-temperature magnetic resonance force detection apparatus. It was found that force detection can be used for spectroscopic measurements in micron-size samples, and the hyperfine splitting of the EPR line was observed for the low dopant-concentration sample ($N_D \simeq 8 \times 10^{16}$ cm^{-3}).

Here, we compare imaging characteristics of low- and high-concentration phosphorus-doped silicon using the improved low-temperature MRFM apparatus.

Samples were approximately 100-μm-thick phosphorus-doped silicon pieces (4 mm $\times$ 2 mm). Two samples with dopant concentrations $N_D \simeq 8 \times 10^{16}$ cm^{-3} and 4×10^{18} cm^{-3} were used. A 55-μm-radius nickel sphere was used as a magnetic tip (Fig. 5.5(b)).

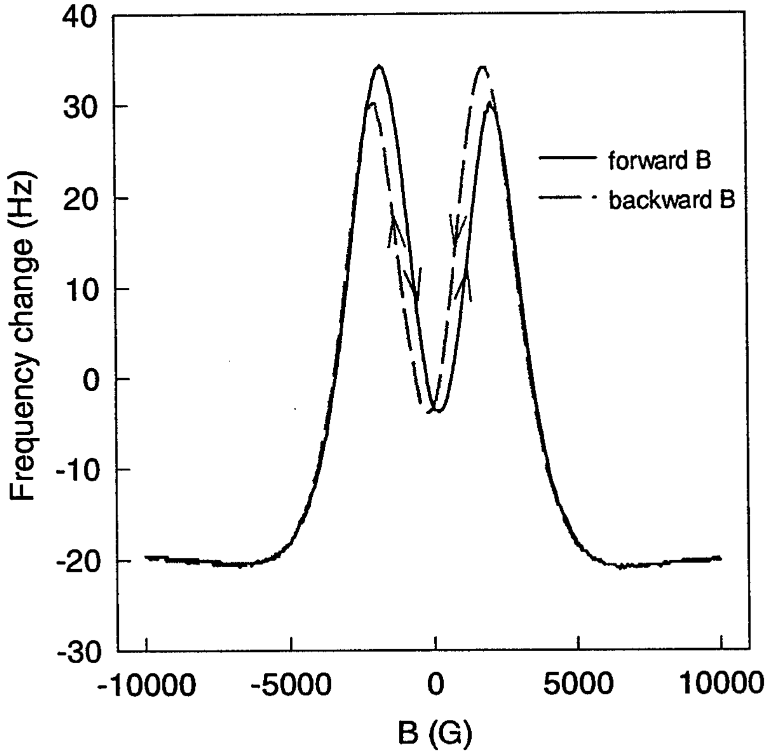

Figure 5.8: The resonant frequency of the cantilever with a nickel sphere ($r \simeq 10$ μm) as the field is swept forward and backward.

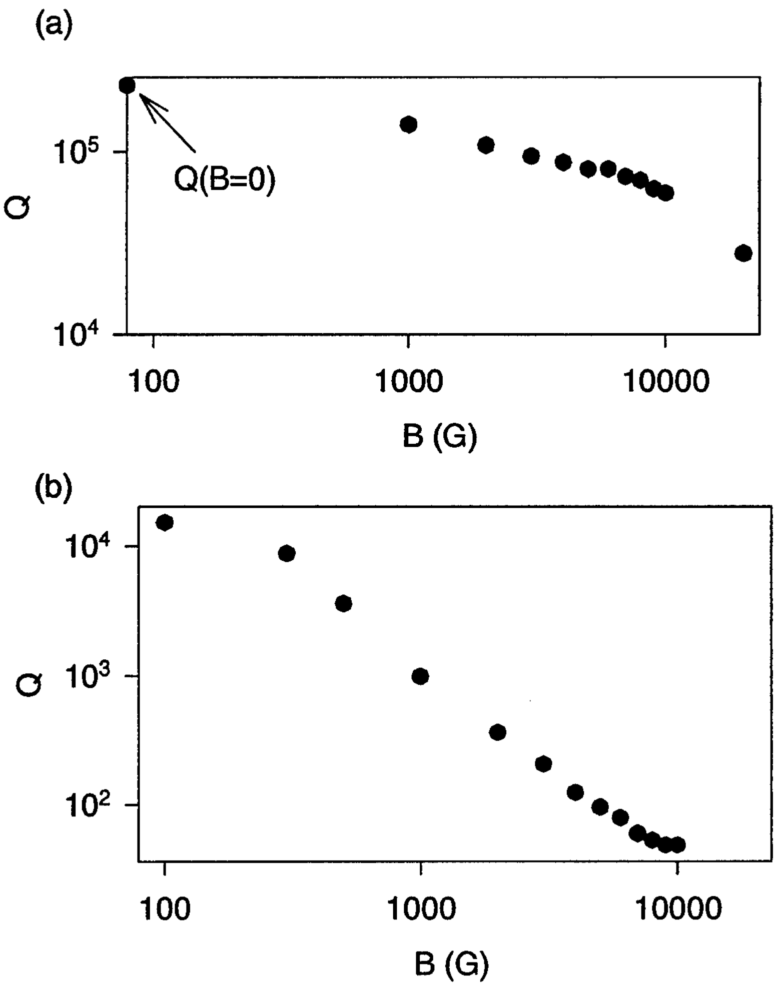

Figure 5.9: (a) Q of the cantilever with a nickel sphere ($r \simeq 10$ μm) as a function of the field. (b) Q of the cantilever with a nickel sphere ($r \simeq 55$ μm) as a function of the field.

Since the samples are uniformly doped and the lateral dimensions are much larger than the tip size, scanning in x and y does not provide any information on the imaging characteristics. Instead, EPR spectra were obtained by sweeping the external field B_{ext} with various tip-sample distances.

5.3.1 Low-dopant-concentration silicon

Figure 5.10 shows EPR spectra for low-concentration sample ($N_D \simeq 8 \times 10^{16}$ cm^{-3}). Tip-sample distances were approximately 80 μm for (a), 60 μm for (b), and 40 μm for (c), respectively. A bipolar signal was observed at ~4300 G independent of the tip-sample distance. The peak-to-peak force was approximately 100 fN.

A smaller peak, indicated by arrows, was also observed downfield from the bipolar peak. The position of the small peak moved to lower field as the tip-sample distance was decreased.

Magnetic resonance is induced for spins within the resonant slice, where $|\mathbf{B}_{\text{ext}} + \mathbf{B}_{\text{tip}}| \simeq 4300$ G for electron spins in the 12-GHz microwave field. If $|\mathbf{B}_{\text{ext}}| \gg |\mathbf{B}_{\text{tip}}|$, which is typically the case in the experiments, the resonant slice is a paraboloidal-shape contour of the z component of $\mathbf{B}_{\text{tip}}$, which we designate $B_{z,\text{tip}}$. Figure 5.11 shows contours of $B_{z,\text{tip}}$ for a fully magnetized nickel sphere of 55 μm radius. Contours are cylindrically symmetric and the cross-sections with the x-z plane are shown in the figure. Sweeping B_{ext} to higher field has the effect of moving the resonant slice away from the tip (to contours of smaller $B_{z,\text{tip}}$ values). Contours of $\partial B_{z,\text{tip}}/\partial z$, which determines the thickness of the resonant slice and hence the z resolution of MRFM, are also shown in Fig. 5.12. Contours of $\partial B_{z,\text{tip}}/\partial x$, which relates to the lateral spatial resolution of MRFM, are shown in Fig. 5.13.

As B_{ext} is swept from lower field with a fixed tip-sample distance, initially

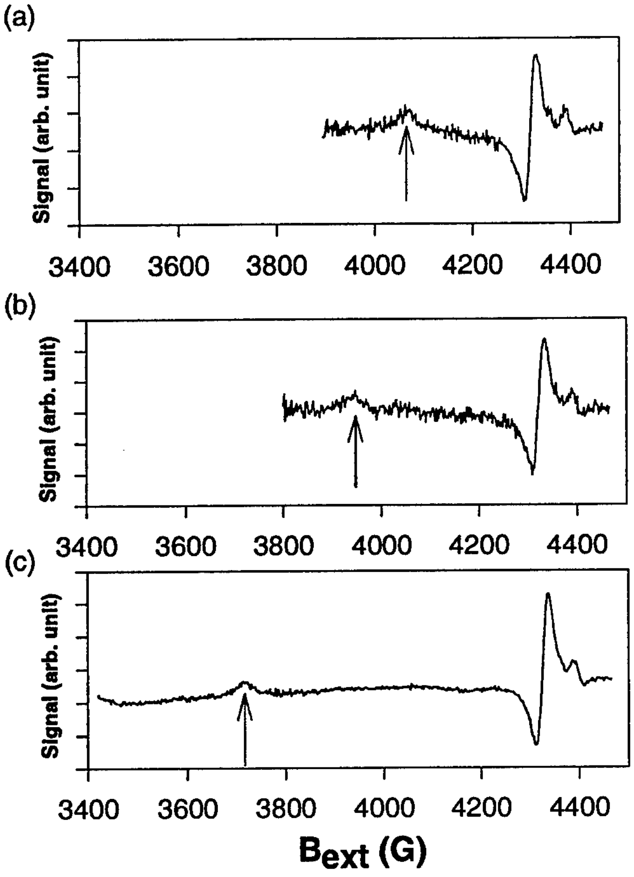

Figure 5.10: Force-detected EPR spectra of a ~100-μm-thick phosphorus-doped silicon sample. Dopant concentration is $\sim 8 \times 10^{16}$ cm^{-3}. Arrows indicate a peak that depends on the tip-sample distance. (a) The tip-sample distance was ~ 80 μm. (b) The tip-sample distance was ~ 60 μm. (c) The tip-sample distance was ~ 40 μm.

there is no overlap between the sample and the resonant slice that is too close to the tip. Therefore, there is no EPR force response until B_{ext} is swept up such that the resonant slice moves far enough from the tip to reach the sample surface. The small peaks observed in Fig. 5.10 are considered to correspond to the response when the resonant slice reaches the sample surface. For smaller tip-sample distances, lower B_{ext} is required for the resonant slice to reach the sample, causing the small peak to appear at lower field as shown in Fig. 5.10.

As B_{ext} is swept further up, the overlap volume between the sample and the resonant slice increases. However, the force per unit volume, which is proportional to $|\partial B_{z,\text{tip}}/\partial z|$, decreases at the same time, and the total EPR force changes rather gradually. The FM cyclic saturation technique used in the experiment gives a differential response as explained in Section 3.2.2. Therefore, the gradual change beyond the point where the resonant slice reaches the sample surface does not result in a distinctive peak.

When $B_{\text{ext}} \simeq 4300$ G, the resonant slice is far away from the tip (> 200 μm), and is thick because the gradient is small far from the tip. In other words, a large region of the sample except the proximity to the tip becomes on resonance. Although the force per volume is quite small, the large volume of the resonance results in rather a strong force. As B_{ext} is increased further, the resonant slice disappears rapidly, causing a distinctive response in EPR force spectra obtained by the FM cyclic saturation technique. The peak around 4300 G does not strongly depend on the tip-sample distance, since it is arising from the region far away from the tip.

Force-detected EPR spectra for a uniform thin sample can be more rigorously analyzed. The EPR force from spins in a volume dV is given by

$$dF = \frac{N_D \mu_B^2 B_0}{k_B T} S_{FM} dV, \tag{5.5}$$

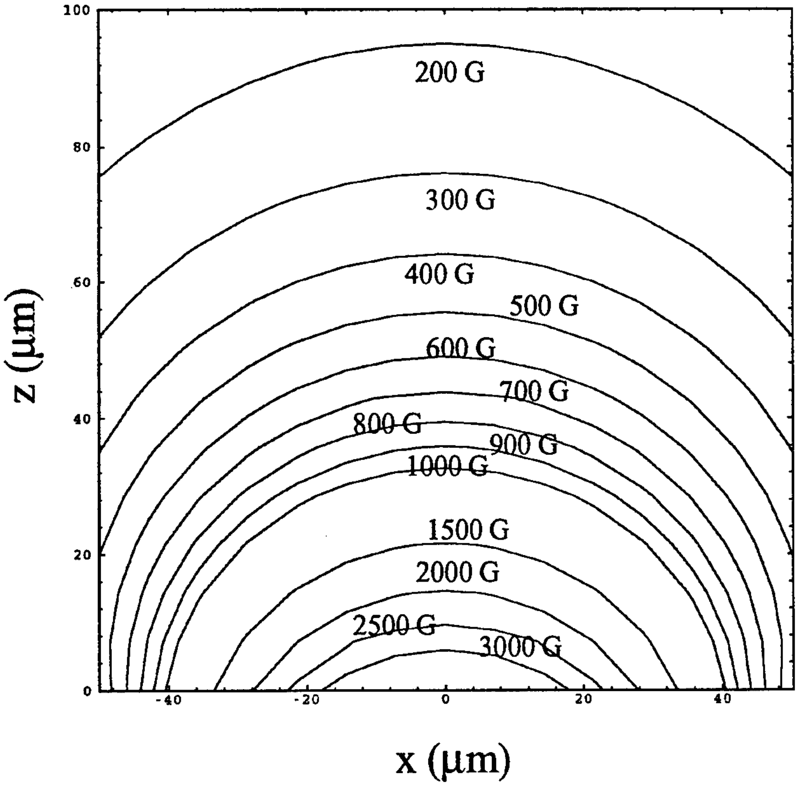

Figure 5.11: Contours of B_z from a fully magnetized nickel sphere ($r = 55$ μm). The z axis denotes the distance from the surface of the sphere.

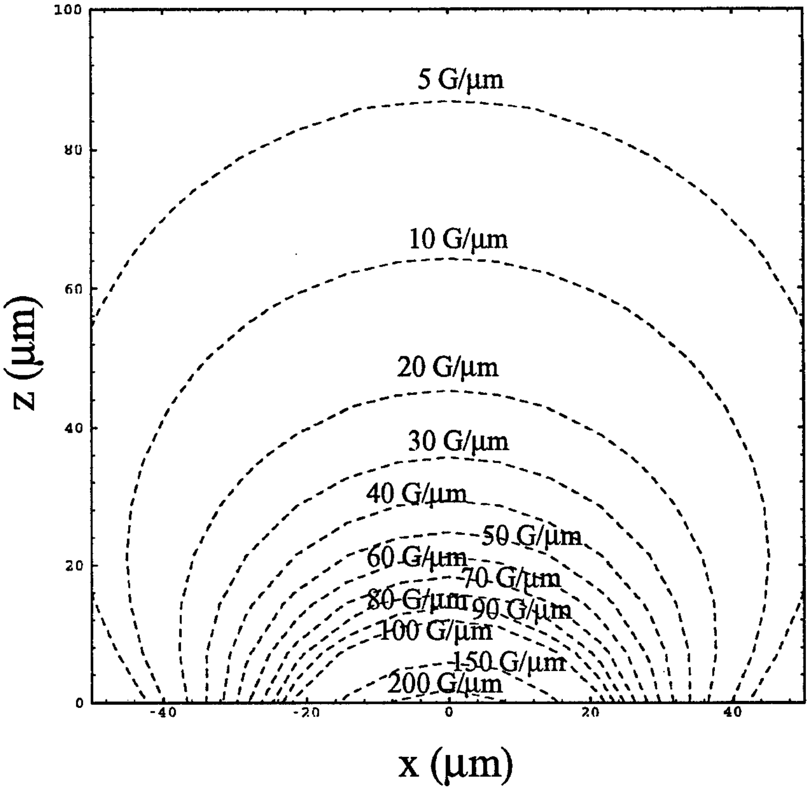

Figure 5.12: Contours of $\partial B_z/\partial z$ from a fully magnetized nickel sphere ($r = 55$ μm). The z axis denotes the distance from the surface of the sphere.

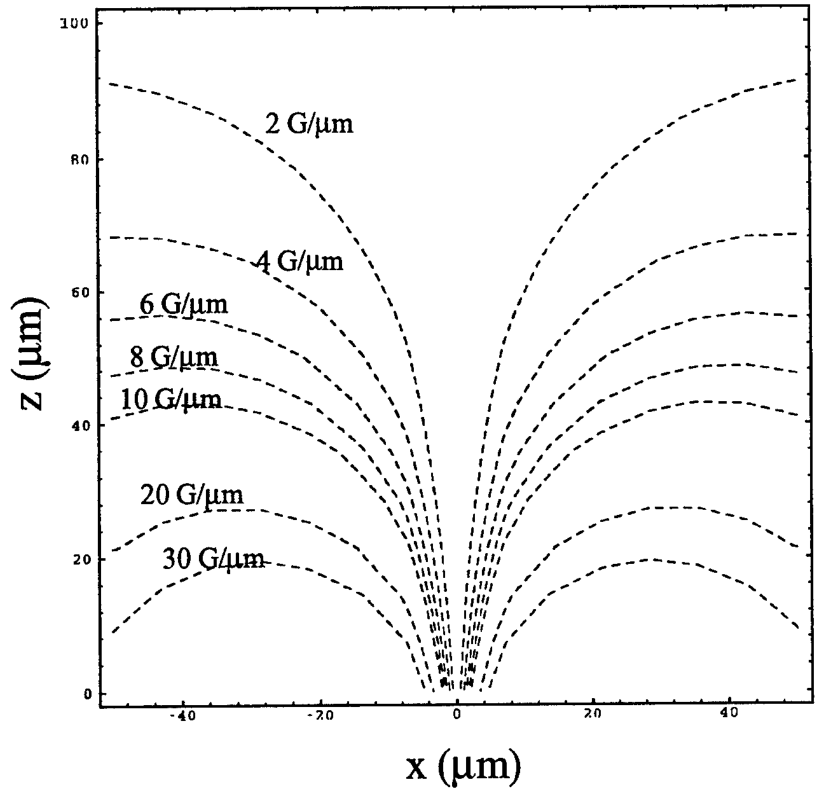

Figure 5.13: Contours of $\partial B_z/\partial x$ from a fully magnetized nickel sphere ($r = 55\ \mu\text{m}$). The z axis denotes the distance from the surface of the sphere.

where μ_B is the Bohr magneton, $B_0 \simeq 4300$ G is the resonant field for 12-GHz microwave field B_1, and S_{FM} is the response for the FM cyclic saturation given by

$$S_{FM} = \mathcal{F}\left\{\frac{\gamma^2 B_1^2 T_1 T_2}{1+[\gamma(B_{\text{ext}}+B_{\text{tip}})-\omega(t)]^2 T_2^2+\gamma^2 B_1^2 T_1 T_2}\right\}\frac{\partial B_{\text{tip}}}{\partial z}. \tag{5.6}$$

Here, $\omega(t) = \omega_0 + \Omega\cos(\omega_c t)$ is the frequency of B_1 modulated at the cantilever resonant frequency ω_c, and $\mathcal{F}$ denotes the first-harmonic Fourier component at ω_c. The total force can be obtained by integrating dF over the sample volume. We approximate the sample to be infinitely thin with the dopant concentration per unit area $\sigma_D = N_D\delta$, where δ is the sample thickness. Then, noting B_{tip} and $\partial B_{\text{tip}}/\partial z$ are cylindrically symmetric, we obtain the total force

$$F = \frac{\sigma_D \mu_B^2 B_0}{k_B T}\int_0^{x_{\max}} S_{FM}\cdot 2\pi x\,dx, \tag{5.7}$$

where $x_{\max}$ is a reasonably large cutoff length.

Figures 5.14, 5.15, and 5.16 show the calculation results of

$$\int_0^{x_{\max}} S_{FM}\cdot 2\pi x\,dx \tag{5.8}$$

as a function of B_{ext} for the tip-sample distances of 150 μm, 100 μm, and 50 μm, respectively. Values of $\gamma = 1.76\times10^7$ rad s^{-1}G^{-1}, $T_1 = T_2 = 10^{-6}$ s, B_1=0.5 G, $\omega_0/2\pi$=11.84 GHz, $\Omega/2\pi = 10$ MHz, $x_{\max} = 1$ mm, and B_{tip}, $\partial B_{\text{tip}}/\partial z$ for a fully magnetized nickel sphere of 55 μm radius were used. The results show a bipolar peak relatively independent of the tip-sample distance, and a small peak that moves towards lower field as the tip-sample distance is decreased, in good qualitative agreement with the experiments. The peak-to-peak value is on the order of 1, giving

$$\begin{aligned} F &\simeq \frac{\sigma_D \mu_B^2 B_0}{k_B T}\times 1 \\ &\simeq 4\times10^{-7}\ \text{dyne} \\ &\simeq 4\times10^{-12}\ \text{N}, \end{aligned} \tag{5.9}$$

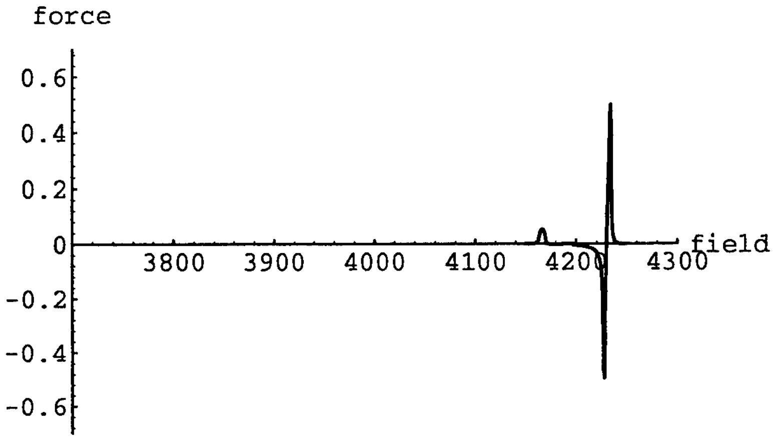

Figure 5.14: The simulation result for EPR force for a thin sample and a 55-μm-radius nickel sphere tip. Tip-sample distance is 150 μm.

which is about 40 times larger than the experimental results. The discrepancy is presumably due to the uncertainty in the parameter values and the rather crude approximation that the sample is infinitely thin.

Small features appearing at the high-field side of the bipolar peak in Fig. 5.10 are probably due to the hyperfine splitting, although the size and phase of the signal is not understood.

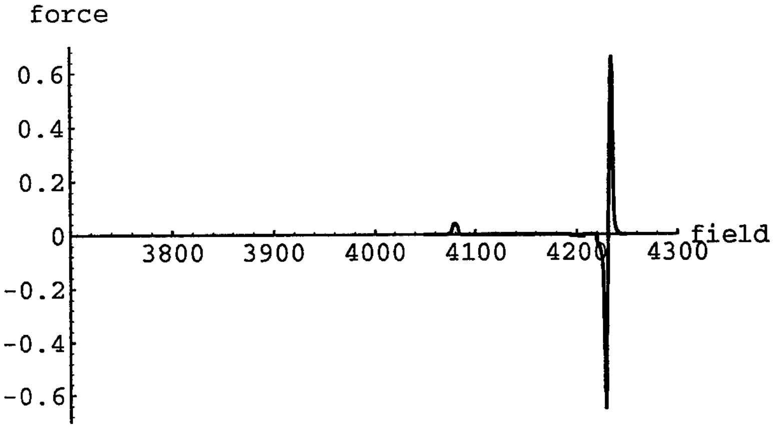

Figure 5.15: The simulation result for EPR force for a thin sample and a 55-μm-radius nickel sphere tip. Tip-sample distance is 100 μm.

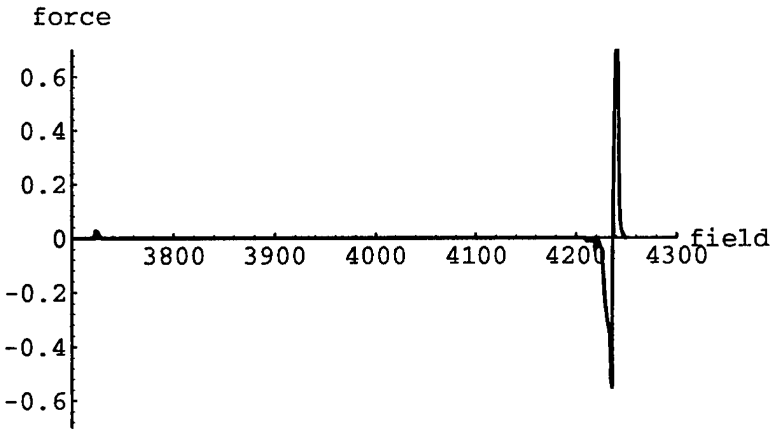

Figure 5.16: The simulation result for EPR force for a thin sample and a 55-μm-radius nickel sphere tip. Tip-sample distance is 50 μm.

5.3.2 High-dopant-concentration silicon

Results for the high-concentration ($N_D \simeq 4 \times 10^{18}$ cm^{-3}) sample showed a remarkable difference from the low-concentration sample results. Figure 5.17 shows force-detected EPR spectra of the high-concentration sample for the tip-sample distances of 100, 80, 60, and 40 μm. There is no apparent dependence on the tip-sample distance. Besides the bipolar peak around 4300 G, no peak is observed downfield unlike the case for the low-concentration sample. The close-up of the bipolar peak shows some dependence on the tip-sample distance, including the peak height difference, the shift of the peak, and the relatively long tail towards lower field for smaller tip-sample distances.

The lack of the major dependence on the tip-sample distance is a consequence of the nature of conduction electrons. Unlike the localized electrons in the low-concentration sample, the conduction electrons in the high-concentration sample feels an "average" field from the tip. Since the Hamiltonian H, which has the spatially dependent part arising from B_{tip}, appears in the form

$$\int \psi^*(\mathbf{r}) H(\mathbf{r}) \psi(\mathbf{r})\, d\mathbf{r} \tag{5.10}$$

to give the energies of the electron, the effect of B_{tip} is averaged over the extended region covered by the conduction electron wavefunction ψ.

5.4 EPR force imaging of DPPH sample

To further investigate imaging characteristics of paramagnetic samples, EPR force maps were obtained by scanning a non-uniform sample in x-y. Figure 5.18(a) shows an optical micrograph of the sample consisting of two diphenylpicrylhydrazil (DPPH) particles, ~5 μm in size.

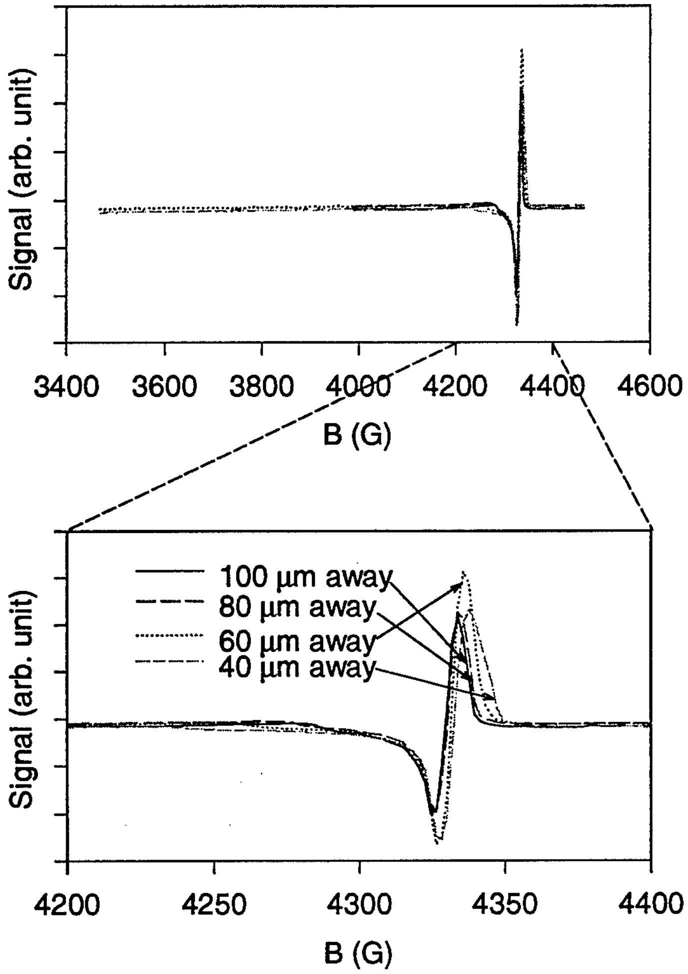

Figure 5.17: Force-detected EPR spectra for a high-concentration (4×10^{18} cm^{-3}) phosphorus-doped thin silicon sample. Tip-sample distances were approximately 100, 80, 60, and 40 μm.

Figure 5.18(b) shows a force-detected EPR signal presented as a gray-scale x-y image for $B_{\text{ext}} = 3895$ G. As explained in Ref. [16], the EPR force map has a ring-like character, reflecting the intersection of the scan-plane with the paraboloidal resonant slice created by the tip field ($B_{\text{tip}}(x, y, z) + B_{\text{ext}} \simeq 4300$ G). Two ring-like responses are observed in Fig. 5.18(b), arising from two sample particles. The center of each ring corresponds to the lateral position of each particle. The diameters of the rings are indicative of the z position of the particles. Since the ring-like response corresponds to the intersection of the sample scan-plane and the resonant slice, which is a contour of $B_{\text{tip}} \simeq 400$ G as shown in Fig. 5.11, the diameters, ~38 μm and ~68 μm, respectively, indicates the tip-sample distances of ~56 μm and ~51 μm, respectively. The larger diameter means the closer tip-sample distance.

Each ring-like response in Fig. 5.18(b) contains the information of the size and shape of each sample particle contributing to the response. This fact is more clearly demonstrated using the sample consisting of larger particles, shown in Fig. 5.19.

Figure 5.20 shows EPR force maps for four B_{ext} values obtained by scanning the sample shown in Fig. 5.19. As in the EPR force map for the smaller sample (Fig. 5.18), the force maps have a ring-like character, reflecting the intersection of the scan-plane with the paraboloidal resonant slice. Starting from a point-like response in Fig. 5.20(a), the radius of the ring-like response increases as B_{ext} is increased. Here, increasing B_{ext} moves the resonant slice away from the tip (to contours of smaller B_{tip} values), and therefore is roughly equivalent to reducing the tip-sample distance with a conversion factor $|(\partial B_{\text{tip}}/\partial z)^{-1}|$. The bipolar nature of the spectral lineshape is manifested in the EPR force map as the dark inner side of the ring-like response with a brighter outer side. It is also noted that the EPR force map is not a simple narrow ring but rather a broadened superposition of more complex

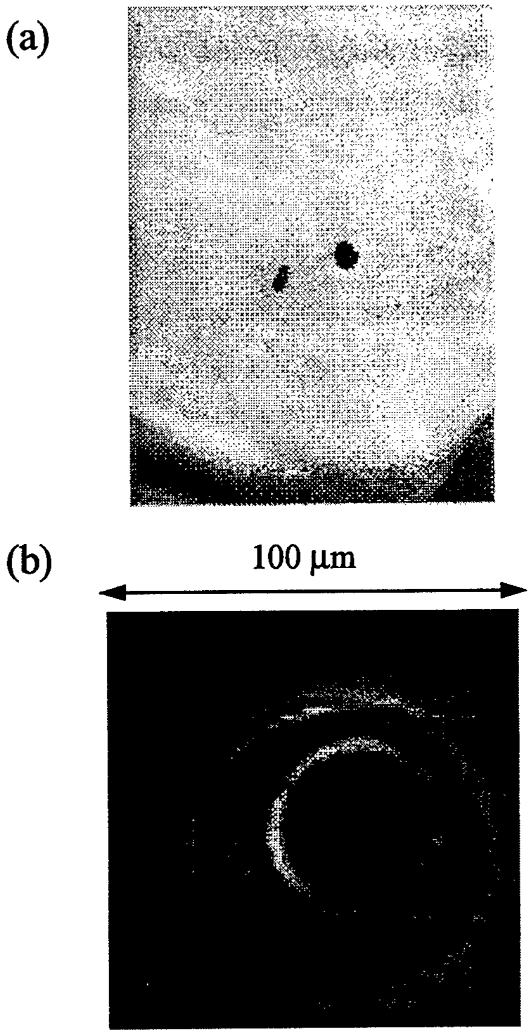

Figure 5.18: (a) Optical micrograph of DPPH sample. (b) EPR force map obtained by scanning the DPPH sample in x-y at $B_{\text{ext}} = 3895$ G.

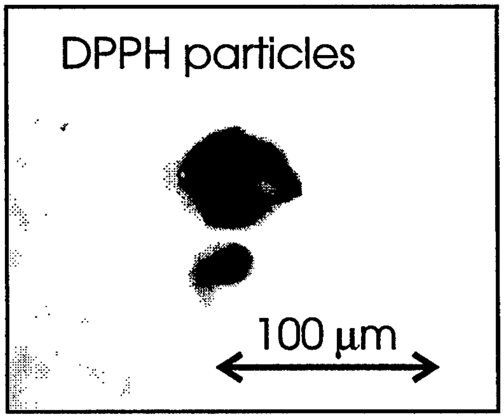

Figure 5.19: Optical micrograph of DPPH sample consisting of two particles.

features, since the signal contains contributions from spins distributed across the spatially extended sample.

Line-broadening due to the contributions from the extended sample is clearly seen in the EPR spectrum shown in Fig. 5.21. The spectrum was obtained by sweeping B_{ext} with a fixed sample position, near the center of the ring-like response in the force map in Fig. 5.20. The spectrum has a bipolar lineshape as a result of the FM cyclic saturation technique, and a broadened linewidth, ~100 G peak-to-peak.

To acquire a real-space image, a three-dimensional EPR force map $F(x, y, B_{\text{ext}})$ was measured on an x-y-B_{ext} lattice of $64 \times 64 \times 33$ points with an acquisition rate of 0.9 s per data point (0.6 s for cantilever frequency and interferometer spacing adjustment and 0.3 s for signal integration). The measured force map can be written using a real-space magnetization map $M(x, y, z)$ as

$$F(x, y, B_{\text{ext}}) = \iiint M(x', y', z') S_{FM}(x', y', z'; x, y, B_{\text{ext}})\, dx'\, dy'\, dz', \tag{5.11}$$

where

$$\begin{aligned} S_{FM} \;=\; & \mathcal{F}\left(\frac{\gamma^2 B_1^2 T_1 T_2}{1 + \{\gamma[B_{\text{ext}} + B_{\text{tip}}(x'-x, y'-y, z')] - \omega(t)\}^2 T_2^2 + \gamma^2 B_1^2 T_1 T_2}\right) \\ & \times \frac{\partial B_{\text{tip}}(x'-x, y'-y, z')}{\partial z} \end{aligned} \tag{5.12}$$

is the response for the FM cyclic saturation as in Eq. (5.6). We approximate that

$$B_{\text{tip}}(x, y, z) \simeq B_{\text{tip}}(x, y, z_0) + \alpha(z - z_0), \tag{5.13}$$

where α is a fixed representative value of $\partial B_{\text{tip}}/\partial z$. Then the B_{ext} scan is equivalent to the z scan with the conversion $B_{\text{ext}} = -\alpha z$, and Eq. (5.11) can be written as a convolution integral

$$\begin{aligned} F_{\text{equiv}}(x, y, z) \;&\equiv\; F(x, y, -\alpha z) \qquad (5.14) \\ &\simeq\; \iiint M(x', y', z') h(x - x', y - y', z - z')\, dx'\, dy'\, dz', \end{aligned}$$

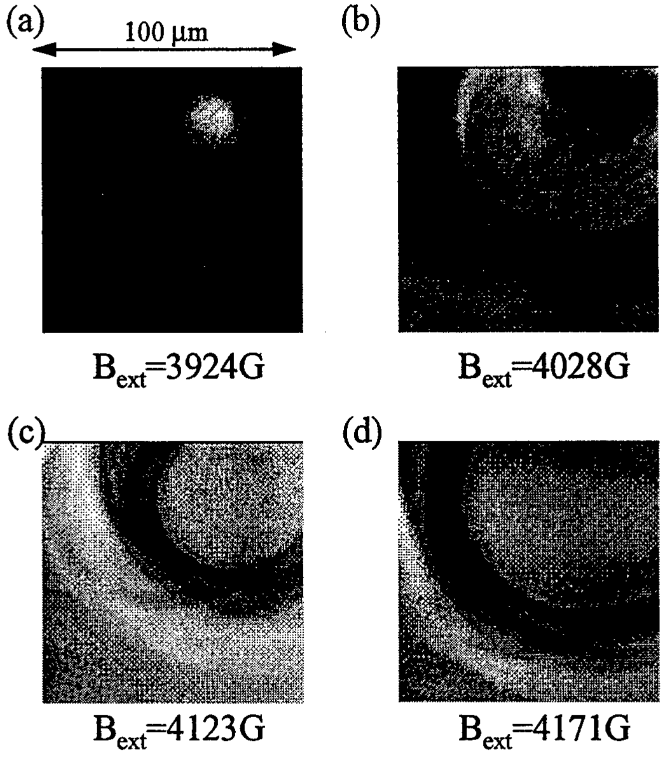

Figure 5.20: EPR force maps obtained by scanning the DPPH sample in x-y at fixed values of B_{ext}.

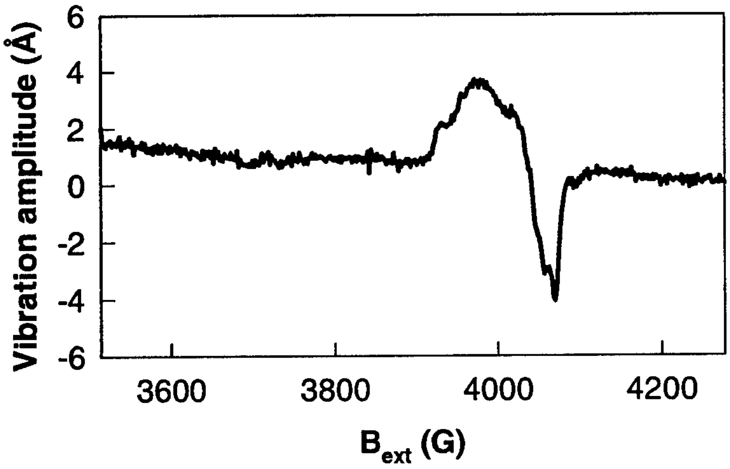

Figure 5.21: Force-detected EPR spectrum for the DPPH sample.

where

$$h(x-x', y-y', z-z') = \mathcal{F}\left(\frac{\gamma^2 B_1^2 T_1 T_2}{1+\{\gamma[B_{\mathrm{tip}}(x'-x, y'-y, z_0)+\alpha(z'-z)-\alpha z_0]-\omega(t)\}^2 T_2^2+\gamma^2 B_1^2 T_1 T_2}\right) \times \frac{\partial B_{\mathrm{tip}}(x'-x, y'-y, z_0)}{\partial z_0}. \tag{5.15}$$

We can reconstruct the real-space $M(x, y, z)$ using the Wiener filtering deconvolution technique described previously by Züger *et al.*[15, 16, 17] such that

$$\hat{M} = \frac{\hat{F}_{\mathrm{equiv}} \hat{h}^*}{|\hat{h}|^2 + C}, \tag{5.16}$$

where $\hat{M}$, $\hat{F}_{\mathrm{equiv}}$, and $\hat{h}$ are the complex-valued three-dimensional Fourier transforms of M, F_{equiv}, and h, respectively, and C is a constant that is adjusted according to the signal-to-noise ratio of the data[43]. The real-space M is then found by the inverse Fourier transform of $\hat{M}$.[4]

The point-response function h for the deconvolution was obtained using calculated values of the field from a fully magnetized nickel sphere of 55 μm radius at $z_0 = 73$ μm as a representative position and a theoretical formula for EPR response based on the estimated values of B_1, spin relaxation times for DPPH, and the FM deviation of B_1 used in the experiment.

A constant density surface of the reconstructed real-space three-dimensional magnetization is shown in Fig. 5.22,[5] showing two main particles consistent with the optical micrograph in Fig. 5.3. Evidence of the difference in z position of the two particles can be seen in the force map, especially in Fig. 5.20(c), as the difference of diameters of ring-like responses arising from the two main particles. The spatial resolution of the reconstructed image is

---

[4] Image processing software PV-WAVE was used in the deconvolution.

[5] IBM Data Explorer was used to render the image.

estimated to be roughly 5 μm. Although overall shape and size of the reconstructed objects appear to be a good representation of the sample particles, the image seems to be somewhat distorted and the detailed structures are not likely to be real. These artifacts are due to the finite signal-to-noise ratio and the limitation of the approximation that the B_{ext} scan is equivalent to the z scan. We would expect higher quality reconstruction if we had physically scanned the tip-sample distance rather than B_{ext}. This was not possible in our present apparatus due to the limited z-scan range of the piezoelectric tube.

5.5 FMR force imaging

Force detection of ferromagnetic resonance (FMR), recently demonstrated by Zhang *et al.*[44], was found to have fundamentally different imaging characteristics compared to the above paramagnetic case. FMR imaging was studied for a sample consisting of a small yttrium iron garnet (YIG) plate, 23 μm × 23 μm and 3 μm thick. The sample was prepared using photolithography and ion milling techniques, starting from a YIG thin film on a gadolinium gallium garnet (GGG) substrate.[6] The sample was oriented such that B_{ext} was normal to the plate.

Figure 5.23(a) shows a force-detected FMR spectrum obtained at a fixed x-y-z position while B_{ext} was swept. The sample position was roughly 50 μm below the magnetic tip and 50 μm away from the axis of the tip laterally. Despite the large lateral field gradient from the tip at this position, $|\nabla B_{\text{tip}}| \simeq 10$ G/μm (see Figs. 5.12 and 5.13), the spectrum shows no significant broadening in contrast to the force-detected EPR spectrum in Fig. 5.21.

---

[6] We thank R. Fontana, L. Lane, and R. Campbell for the fabrication of the YIG sample.

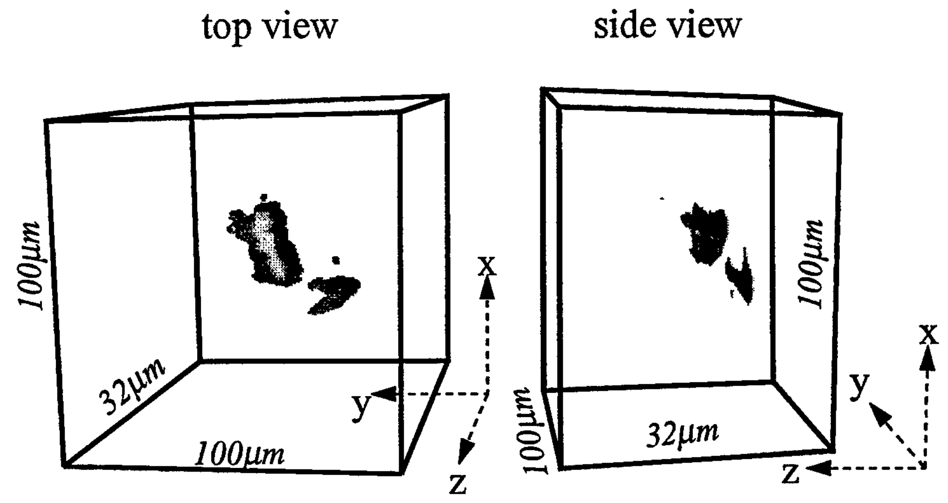

Figure 5.22: Reconstructed three-dimensional magnetization image. Constant density surfaces are depicted from two viewing orientations.

The peak-to-peak linewidth in Fig. 5.23(a) is roughly 8 G, much less than one would expect from the sample size and the field gradient (23 μm × 10 G/μm = 230 G).

The lack of broadening is clearly shown in the FMR force map. Figure 5.23(b) shows the FMR force signal obtained by scanning the sample in x-y with fixed z and $B_{\text{ext}} = 4418$ G. The result shows a ring-like response as in the EPR force map; however, the width of the ring is narrow despite the finite sample size. The difference is clear if one compares the FMR results with the EPR force maps in Fig. 5.20, where a broadened and more complex response was observed due to the finite size and shape of the sample.

The narrow spectral width is a consequence of the nature of FMR. In FMR, spins are exchange coupled to one another and each spin does not act independently. In fact, in the uniform mode, which we believe we are observing, all spins are precessing uniformly. This makes spins in the finite size sample act like a single collective spin ensemble and the FMR force map resembles the response from a point-like sample.

In addition to the main spectral line in Fig. 5.23(a), two small magnetic resonance lines were observed downfield from the main signal. These are higher-order magnetostatic modes as are observed in conventional FMR for normally magnetized YIG disks[45]. In the FMR force map, Fig. 5.23(b), these modes appear as faint concentric rings with larger diameters than the main signal. The concentric rings, including the main signal, represent contours of B_{tip} for constant values that correspond to the resonant fields of each mode (offset by the uniform field B_{ext}). Larger diameter rings correspond to contours of lower field values.

Measurement with lower microwave power (smaller B_1) revealed additional spectral features within the main spectral line, as shown in Fig. 5.24(a). We believe that these are the same structures as observed by Dillon[45] us-

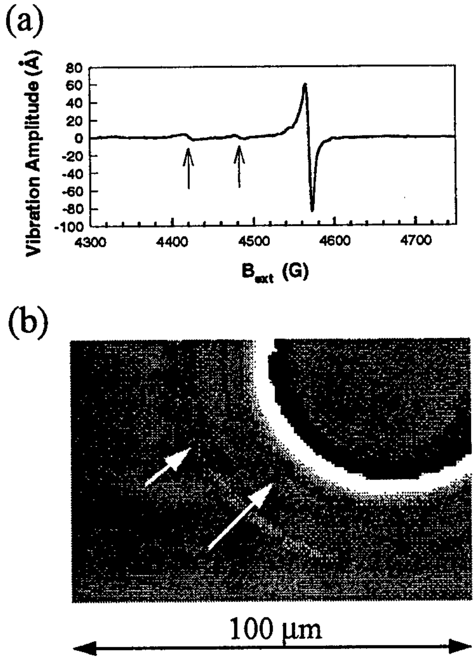

Figure 5.23: (a) Force-detected FMR spectrum for a small YIG plate, showing a narrow-linewidth main signal. Arrows indicate small spectral features observed due to magnetostatic modes. (b) FMR force map at $B_{\text{ext}} = 4418$ G, showing a sharp ring-like response. Arrows indicate concentric ring-like responses due to magnetostatic modes.

ing conventional FMR and proposed to be due to magnetoelastic coupling of magnetostatic and acoustic modes. In the FMR force map with fixed $B_{\text{ext}} = 4342$ G, shown in Fig. 5.24(b), these spectral features are not seen as simple concentric ring-like responses as in the case for the magnetostatic modes. Rather, these features seem to be spiraling across the main response depending on the x-y position, suggesting that the magnetoelastic interaction is not uniform over the entire sample. This result illustrates the ability of MRFM to visualize complex magnetic resonance phenomena on the micrometer scale.

5.6 Magnetic field mapping using force-detected FMR

The sharp spectral features of FMR can be used to make quantitative measurements of magnetic field above a ferromagnetic sample. As shown in Fig. 5.25, the idea is to use force detection to measure ferromagnetic resonance of a small yttrium-iron-garnet (YIG) particle while the particle is mounted on a cantilever and scanned over a sample. Figure 5.26, shows the force-detected spectrum from a micrometer-size gallium-doped YIG particle. A number of resonance peaks appear at well-defined field values. The peaks, which are due to various magnetostatic spin wave modes in the YIG particle, can be used as field markers when the YIG particle is scanned over a sample that generates an inhomogeneous field pattern. As a first example of quantitative field mapping, the YIG particle was scanned over a sample consisting of a 20m diameter nickel sphere. The image in Fig. 5.27 shows a series of bright rings centered over the nickel particle. Each ring corresponds to a specific contour of constant field at a distance approximately 20

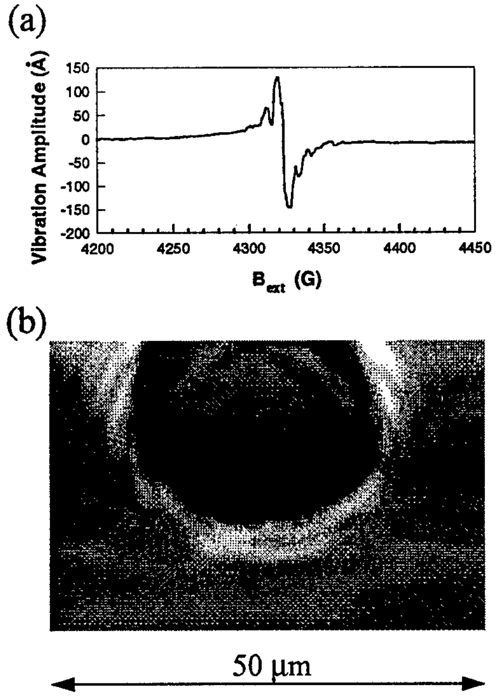

Figure 5.24: (a) Force-detected FMR spectrum obtained at lower microwave power. Small spectral features believed to be due to magnetoelastic coupling are observed within the main line. (b) FMR force map at $B_{\text{ext}} = 4342$ G with the same microwave power. Note the spiral-like features superimposed on the main circular response.

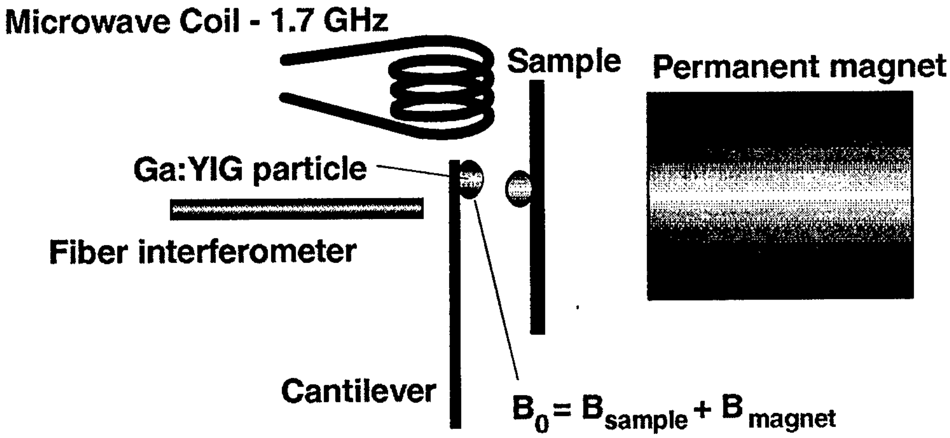

Figure 5.25: Apparatus to quantitatively map the magnetic field emanating from a sample. A Ga-doped YIG particle mounted on the cantilever serves as a local probe of magnetic field emanating from a nearby sample. A cantilever vibration signal is generated whenever the field from the sample matches the field for ferromagnetic resonance of the YIG particle.

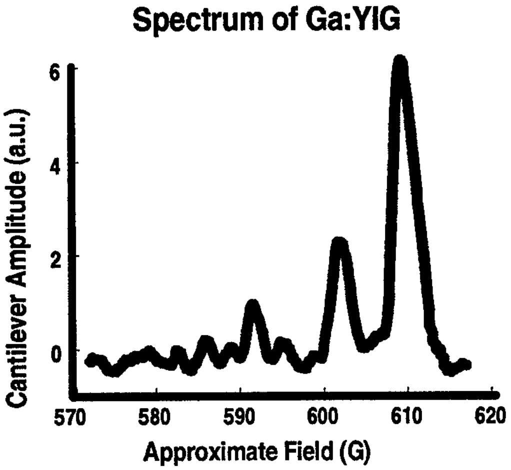

Figure 5.26: Force-detected ferromagnetic resonance spectrum of Ga-doped YIG particle.

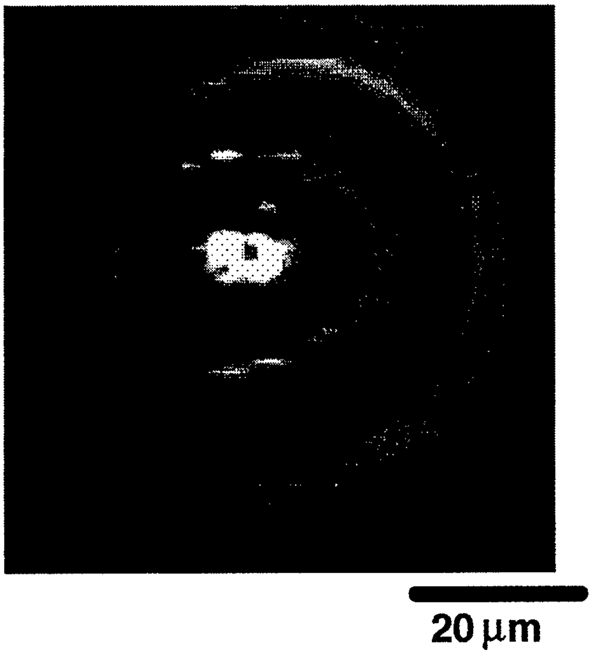

Figure 5.27: MRFM image showing contours of constant field above a 20 micron diameter nickel sphere.

μm above the sample. The spatial resolution is limited only by the size of the YIG probe particle. By using smaller probe particles, extension to submicron resolution should be possible. In addition to obvious applications for characterizing magnetic recording heads, etc., the technique should be useful for characterizing the field emanating from magnetic tips developed for single-spin MRFM experiments.

Chapter 6

Single Spin Experiment

6.1 Experimental configuration

The ultimate goal of IBM's MRFM research is to achieve single spin sensitivity with angstrom spatial resolution in three-dimensions. Considerable effort during the ONR contract has been devoted to developing the apparatus and techniques for single spin detection. The emphasis has been on electron spins rather than nuclear spins because of the larger magnetic moment of the electron.

Figure 6.1 shows a schematic diagram of IBM's single spin experiment. The experiment uses an ultrathin single-crystal silicon cantilever with a magnetic tip positioned within 10-50 nm of the surface of a polished SiO_2 sample. The sample is prepared by gamma irradiation so that it contains a known density of dangling bond defects with unpaired electron spins (E' centers) throughout its volume. The cantilever is oriented perpendicular to the sample in order to allow the tip to approach the sample surface to within 10 nm without being snapped into the surface by electrostatic and van der Waals forces. The sharp end of the cantilever is coated along one sidewall with

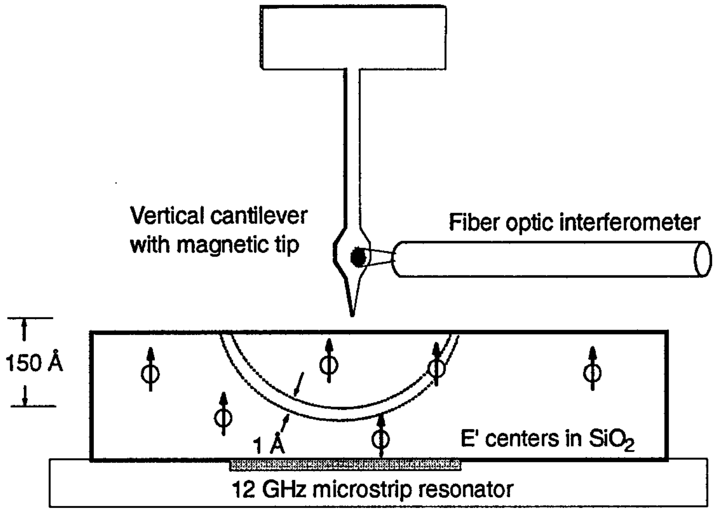

Figure 6.1: Experiment to detect individual electron spins (E' centers) in SiO_2. The 1 Å-thick resonant slice is shown by the dotted lines.

60nm of cobalt to form a magnetic tip. Angstrom-scale vibration of the cantilever is detected by a fiberoptic interferometer. The apparatus is operated at 4K so as to improve the force resolution of the cantilever and to maximize the spin-lattice relaxation time of the spins.

As is usual for MRFM experiments, the magnetic field from the tip plus an external field (in this case from a superconducting magnet) defines a resonant slice wherein magnetic resonance occurs. Electron spins located within the resonant slice undergo magnetic resonance stimulated by the 12 GHz microwave magnetic field generated by a microstripline resonator. The microstripline-sample combination is mounted on a piezoelectric tube scanner, allowing the tip to be scanned with respect to the sample in three dimensions.

The perpendicular cantilever configuration in our experiment responds to lateral forces. The lateral force due to the interaction of the tip field gradient with the target spin is given by

$$F_x = \mu_e \partial B_z / \partial x, \tag{6.1}$$

where μ_e is the magnetic moment of the electron (9.3×10^{-21} emu or 9.3×10^{-24} J/T).

Because μ_e is so small, it is important to have a large field gradient. For our present tip fabrication techniques, a gradient up to $\partial B_z / \partial x = 10$ Gauss/Å may be achievable. If this gradient is achieved, then the resulting force is 93 aN or, if the force oscillates sinusoidally, 66 aN-rms. (1aN = 1 attonewton = 10^{-18} newton.) Thus, despite the large field gradient, the resulting magnetic force is very small indeed. For comparison, this force is a million times smaller than the piconewton forces detected by conventional atomic force microscopes.

6.2 Ultrasensitive silicon cantilevers

Because of the smallness of the force to be detected, considerable effort has been devoted to developing the capability to detect attonewton forces. To enhance our capability in the area micromechanical fabrication, a strong collaboration has been established with Prof. Tom Kenny and his student Tim Stowe at Stanford University. Working together, we have demonstrated the most sensitive force detection ever achieved with mechanical sensors.

As discussed in Chapter 2, the minimum force detectable in a bandwidth $\Delta\nu$ is limited by the thermal motion of the cantilever according to

$$F_{\min} = \sqrt{\frac{4kk_BT\Delta\nu}{Q\omega_c}}. \tag{6.2}$$

The factor k/ω_c can be written in terms of cantilever geometry. For a rectangular cantilever with thickness t, width w and length l, the minimum detectable force is

$$F_{\min} = \left(\frac{wt^2}{lQ}\right)^{1/2} (E\rho)^{1/4} (k_{\mathrm{B}}T\Delta\nu)^{1/2}, \tag{6.3}$$

where E is the Young's modulus and ρ is the density of the cantilever material.

The above equation suggests the strategy we have adopted to achieve ultrasensitive force detection: fabricate high Q cantilevers that are thin, narrow, and long. In particular, we have succeeded in fabricating single-crystal silicon cantilevers as thin as 500Å and as long as 0.4 mm. Single-crystal silicon is a good choice as the cantilever material since it has low intrinsic mechanical loss (i.e., high Q) and very low internal stress, allowing long, thin structures to be fabricated without unwanted curling.

As shown in Fig. 6.2, the cantilever processing begins with ⟨100⟩-oriented silicon-on-insulator (SOI) wafers with a top silicon layer thickness of 1800Å.

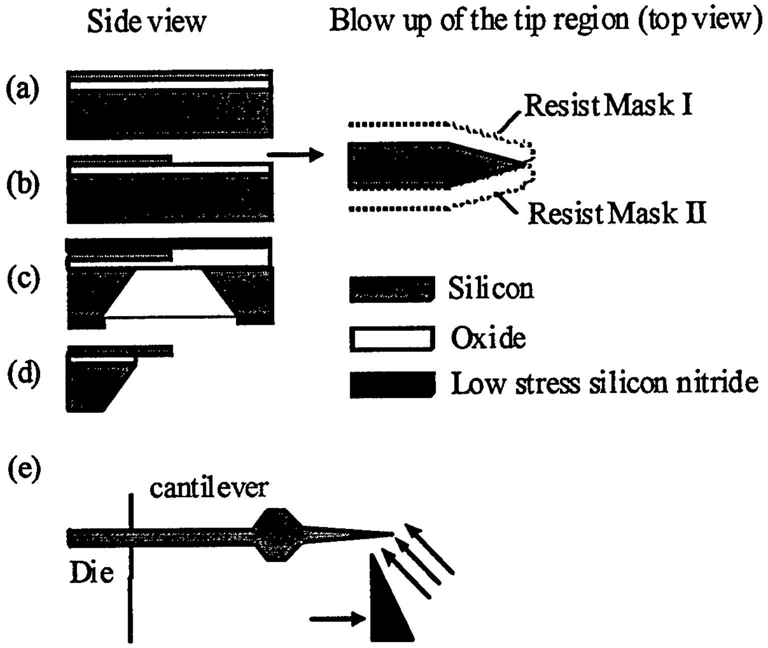

Figure 6.2: Processing steps for fabricating ultrathin silicon cantilevers with integrated in-plane ferromagnetic tips.

This top silicon layer is first thinned down to a desired thickness by growing a thermal oxide, which is then removed using a standard buffered oxide etch (BOE). Next, the cantilever and the tip are defined using a two step mask and etch process [Fig. 6.2(b)]. The first photoresist mask defines the cantilever outline with a tip rounded to 0.5 μm, the limit of our optical lithography. This cantilever pattern is etched into the silicon using a SF_6 plasma etch. This mask is stripped and a second photoresist mask containing the same pattern is applied again, but shifted to the right of the first pattern by 1 μm. A tip forms at the intersection of the right sidewall formed during the first etch and the left sidewall of the second etch, yielding a tip radius below 500-Å.

Once the cantilevers have been patterned, a 7500-Å-thick layer of low temperature oxide (LTO) and a 1-μm-thick layer of low stress nitride are deposited for topside protection. Openings in the backside LTO and nitride are patterned and the exposed silicon is etched anisotropically in 20% tetramethylammonium hydroxide (TMAH). After the backside etch is complete [see Fig. 6.2(c)], the top nitride layer is removed using a SF_6 plasma etch and the oxide membrane encapsulating the cantilevers is removed using BOE.

The wafer is transferred under liquid from BOE to water and then from water to methanol, followed by critical point drying in high pressure liquid CO_2. This CO_2 drying step avoids meniscus forces that can easily break or permanently curl the cantilevers. Finally, silicon dies defined during the backside etch are cleaved [Fig. 6.2(d)]. Each die contains cantilevers that are 4–6 μm wide and 20–400 μm long. Yields over 80% have been achieved for cantilever arrays as thin as 500Å.

Figure 6.3 shows a finished 220-μm-long, 600-Å-thick cantilever. The cantilever design includes a 20-μm-wide paddle for easy alignment of the fiberoptic interferometer to the cantilever. Tip radii were evaluated by elec-

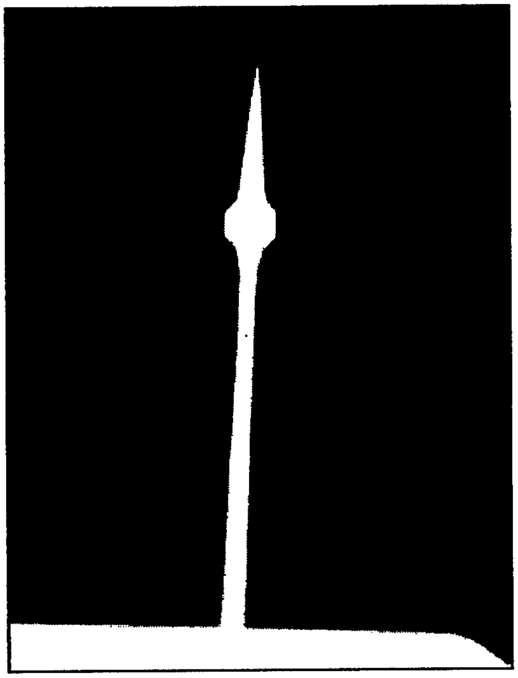

Figure 6.3: A 600 Å-thick, 220 μm-long single-crystal silicon cantilever with in-plane tip.

tron microscopy and found to be routinely in the 30–60 nm range.

6.3 Attonewton force detection

To evaluate the force resolution of a 600 Å thick, 220-μm-long cantilever, its motion was measured in vacuum at both room temperature and 4.8K using a fiber optic interferometer. The thermal motion of the cantilever at room temperature was measured to be 250 Å-rms which, from the equipartition theorem (equation (2.1)), implies a spring constant of 6.5×10^{-6} N/m.

This estimated spring constant is within 10% of the value predicted by finite element analysis.

At 4.8K, the cantilever thermal vibration was reduced to 43Å-rms, somewhat larger than the theoretical value of 32 Å-rms expected from $T^{1/2}$ scaling of the room temperature noise. This small discrepancy may be due to laser heating of the cantilever or environmental vibrations. Combining the measured cantilever vibration noise with the other cantilever parameters ($k = 6.5\mu$N/m, $f_0 = 1.7$ kHz and $Q = 6700$) gives a theoretical noise of 5.6 aN/Hz$^{1/2}$.

To demonstrate attonewton force detection, an electrode located $\sim$ 1 mm from the cantilever was used to generate a small electrostatic force oscillating at the cantilever resonance frequency. Figure 6.4 shows a time trace of the cantilever vibration amplitude as detected by the interferometer and a lock-in amplifier. When the oscillating electrostatic force was turned on, the cantilever reached a steady-state amplitude of 370-Å-rms. Based on the previously determined values of k and Q, this corresponds to a 36 aN-rms force. Using a detection bandwidth that was dominated by the natural bandwidth of the cantilever, a noise level of 3.6 aN was measured, yielding a signal-to-noise ratio of 10.

The demonstrated force resolution of 5.6 aN/Hz$^{1/2}$ is, to our knowledge, the best ever achieved using a a mechanical sensor. Even better resolution could have been achieved if higher Q (lower dissipation) had been achieved. Studies of energy dissipation in thin microcantilevers are ongoing.

6.4 Magnetic tips

The tip of the silicon cantilever is made magnetic by evaporating a thin cobalt film onto the cantilever sidewall, as shown in Fig. 6.2(e). By evaporating the

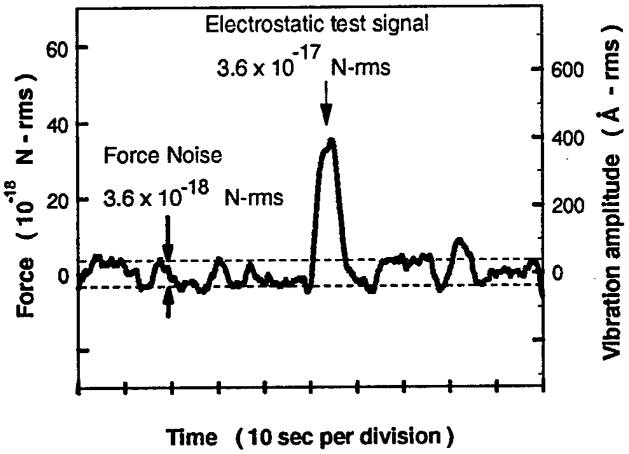

Figure 6.4: Time trace of the cantilever vibration amplitude showing noise and response to an oscillating 36 aN-rms electrostatic force. The cantilever vibration amplitude is shown on the right hand scale and the corresponding force on the left hand scale. A force noise of 3.6 aN was measured. The bandwidth of the measurement was set by the natural bandwidth of the cantilever (approximately 0.4 Hz).

cobalt preferentially onto the sidewall of the tip, a long, thin magnetic "wire" is formed that exhibits strong shape anisotropy. Side-wall deposition has an additional benefit: it avoids problems with stress in the deposited film which would cause the the cantilever to curl if the film were deposited onto the face of the cantilever. For most of our tips, knife-edge shadow masking was used to confine the cobalt to the tip region, thus minimizing mechanical dissipation effects due to the presence of the cobalt.

Magnetic characteristics of the tips have been investigated in several ways. First, the tips were used for magnetic force microscopy (MFM) of bit transitions on magnetic recording disks. High quality MFM images were obtained. In addition, information about the total moment and anisotropy of the tip was obtained by measuring the cantilever frequency as function of applied magnetic field.

Figure 6.5 shows a hysteresis loop obtained by measuring the natural frequency of the cantilever as a function of the magnetic field applied along the longitudinal axis of the cantilever. If we start at high field, where the tip magnetization is saturated, and follow the frequency as the field is decreased toward zero, we see a smooth change in frequency. As the field goes negative, there are jumps in frequency occurring at approximately -900 Gauss and -6000 Gauss. These frequency jumps represent sudden switching of the tip magnetization. The large jump at -6000 Gauss is believed to be due to magnetic switching of the cobalt located along the sidewall of the cantilever, where the bulk of the cobalt is located. This magnetic material exhibits a large coercivity because of the strong shape anisotropy. The small jump at -900 Gauss is believed to be due to the small amount of material inadvertantly deposited onto the face of the cantilever. The coercivity is much smaller because there is very little shape anisotropy.

The portion of the hysteresis loop from 15000 Gauss to -900 Gauss is

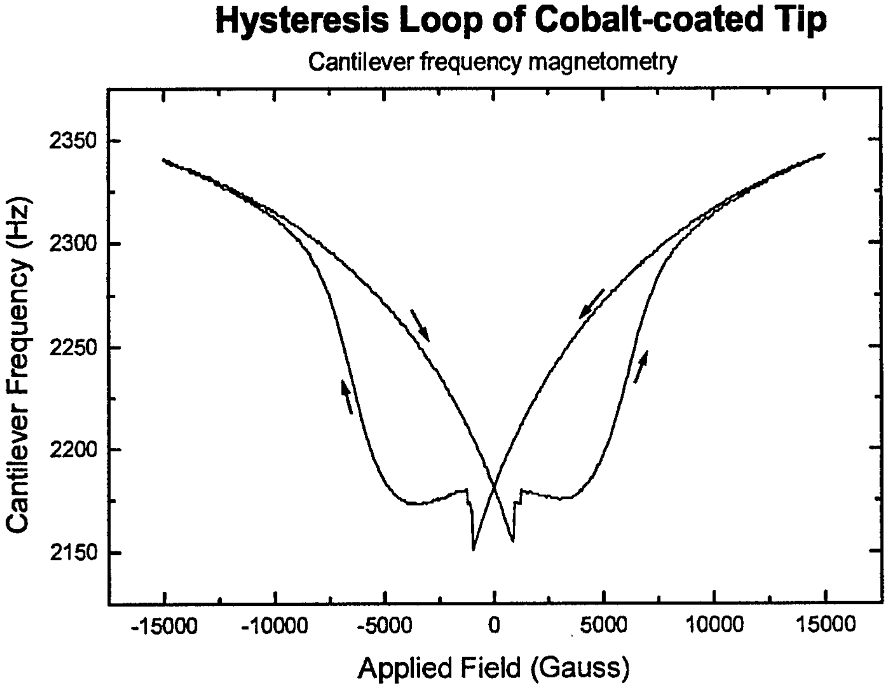

Figure 6.5: Hysteresis loop of cantilever frequency vs. applied field.

reversible and shows very little hysteresis if the direction of the field sweep is reversed. This is an indication that the tip magnetization remains fully saturated over this field range.

The behavior of the reversible portion of the hysteresis loop (+15000 Gauss to -900 Gauss) can be understood using a simple model that combines cantilever motion with the Stoner-Wohlforth model of single domain magnetic particles. Referring to Fig. 6.6, the model assumes that the magnetic tip can be modeled as an elongated single domain particle with saturation magnetization M_s and uniaxial anisotropy K_u in the presence of a z-directed applied field. The cantilever is also oriented in the z direction, but its free-end is allowed to bend as it vibrates. The angle α denotes the tilt angle of the tip due to the bending of the cantilever. α is related to the lateral displacement of the tip according to

$$x = L \sin \alpha, \tag{6.4}$$

where L is an effective cantilever length that is determined by the shape of the cantilever vibrational mode. The direction of the longitudinal axis of the particle is assumed to follow the direction of the free-end of the cantilever. The angle of the tip magnetization with respect to the longitudinal axis of the particle is denoted by θ.

The potential energy of the cantilever-magnetic particle combination can be written as the sum of anisotropy, Zeeman and elastic energy terms:

$$E = K_u \sin^2 \theta - HM_s \cos(\alpha - \theta) + \frac{1}{2} k L^2 \sin^2 \alpha. \tag{6.5}$$

The angle θ of the particle magnetization is assumed to lie in the direction that minimizes the energy. Accordingly, we set $\partial E / \partial \theta = 0$, yielding

$$2K_u \sin \theta \cos \theta - HM_s \sin(\alpha - \theta) = 0. \tag{6.6}$$

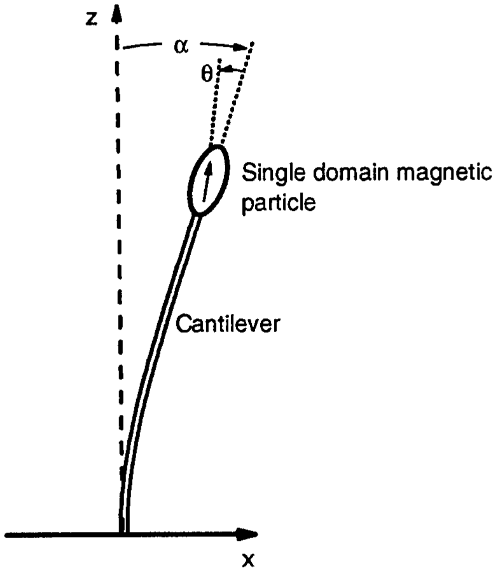

Figure 6.6: Model of single domain particle on a vertical cantilever. The easy (long) axis of the particle is assumed to be aligned with the free end of the cantilever which, during vibration, tilts by an angle α. The particle magnetization is canted by an angle θ with respect to the particle easy axis because of a z-directed applied field.

Solving this for small angles gives

$$\theta = \left(\frac{HM_s}{2K_u + HM_s}\right)\alpha. \tag{6.7}$$

Defining the anisotropy field as $H_k = 2K_u/M_s$ results in

$$\theta = \left(\frac{H}{H_k + H}\right)\alpha. \tag{6.8}$$

Substituting (6.4) and (6.8) into (6.5) and using the small angle approximation gives a spring-like potential energy with a modified spring constant:

$$E = \frac{1}{2}(k + \Delta k)x^2, \tag{6.9}$$

where the spring constant change due to the presence of the applied field is

$$\Delta k = \frac{H_k M_s}{L^2}\left(\frac{H}{H + H_k}\right). \tag{6.10}$$

This simple model gives a virtually perfect fit with experimental data, as can be seen in Fig. 6.7. In this figure we show as points the measured change in spring constant as determined from the frequency data according to

$$\Delta k = k\left(1 - \frac{f_0^2}{f^2}\right), \tag{6.11}$$

where f_0 is the cantilever frequency at zero field. The solid curve in Fig. 6.7 represents a two parameter fit of equation (6.10) to the experimental data. The fitting process uses the known spring constant and length of the cantilever and yields an estimate of the moment of the tip (1.8×10^{-9} emu) and the anisotropy field (8940 Oe).

The fact that the tip exhibits such strong shape anisotropy and remains in a saturated magnetic state down to zero external field is very good news. This should allow the tip to produce the maximum field and field gradient possible for the given geometry. To further evaluate the details of the tip field near the end of the tip, we have recently given samples of our tips to Prof. M. Scheinfein at Arizona State University for characterization by electron holography.

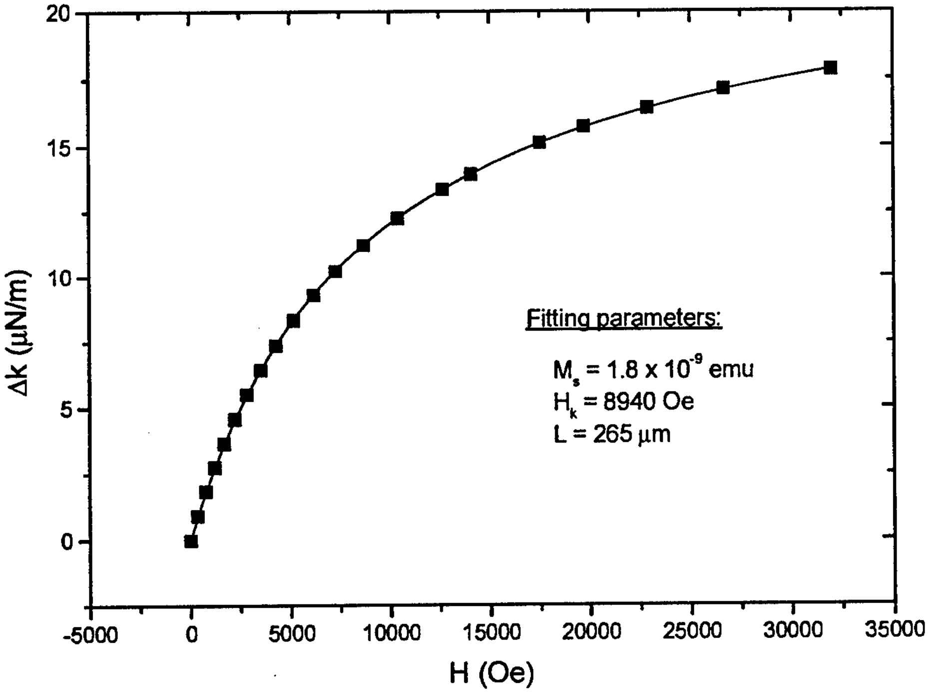

Figure 6.7: The points show the increase in cantilever stiffness measured as a function of applied field for the reversible portion of the hysteresis loop. The solid curve is a plot of equation (6.10) using the fitting parameters shown.

6.5 Single spin experiments

The single spin detection apparatus is essentially complete and has been used in several attempts to detect single spin magnetic resonance. Although no single spin signal has yet been seen, we have gained valuable experience in operating our ultrasensitive cantilevers in close vicinity to sample surfaces.

Several different methods for detecting the single spin signal are under investigation. Here are the three leading contenders:

Method 1 - Cyclic adiabatic inversion induced by frequency modulation of the microwave field

A frequency modulated microwave field is used to induce cyclic adiabatic inversion of a resonant spin. The cyclic inversion of the spin generates an oscillating force on the cantilever, causing it to vibrate.

Advantage: This is a "zero-baseline" experiment, which readily allows the theoretical thermal noise limit to achieved.

Disadvantages: a) It requires a heavily damped cantilever so that cantilever vibrations due to thermal noise and/or the spin signal don't exceed 0.1 Å . This is required so that the variation in the tip field due to the tip vibration Δx and the tip field gradient doesn't disrupt the magnetic resonance of the spin. (i.e., $\Delta x \, \partial B_z/\partial x \ll \Omega/\gamma$, where Ω is the peak frequency deviation of the frequency modulation.) b) The cw microwave field can lead to heating of the experiment. c) Spin relaxation time for spins constantly undergoing cyclic adiabatic inversion may be short ($\sim$ 40 ms).

Method 2 - Tip-induced cyclic adiabatic inversion

Cyclic adiabatic inversion is induced by using a cw microwave field of constant frequency and vibrating the cantilever. The cyclic inversion of the target spin induced by the oscillating tip field will result in a small shift in the eigenfrequency of the cantilever.

Advantage: Effectively enlarges the thickness of the resonant slice and avoids problem of keeping the target spin resonant in the presence of tip thermal vibrations.

Disadvantages: a) Detection of spin-induced cantilever frequency shift must be distinguished from much larger frequency shifts induced by miscellaneous tip-surface interactions. b) The cw microwave field can lead to heating of the experiment. c) Spin relaxation time for spins constantly undergoing cyclic adiabatic inversion may be short ($\sim$ 40 ms).

Method 3 - Sub-harmonic tip-induced adiabatic inversion[1]
The microwave field is off most of the time but is periodically pulsed on for half of a cantilever vibration cycle (e.g. once per hundred cantilever cycles). The combination of the pulsed microwave field with the field sweep caused by the cantilever motion inverts the spin. Interaction between the spin and the magnetic tip shifts the frequency of the cantilever, which alternates between a positive and negative frequency shift each time the microwave pulse inverts the spin.

Advantage: Low duty cycle of the microwave pulse increases spin relaxation time and reduces heating of the experiment.

Disadvantage: Frequency shift is smaller than in Methods 1 and 2.

We are presently exploring all three methods to better determine their relative merits. Method 3 appears to be the front-runner at the present time.

---

[1] This method was suggested to us by J. Sidles

6.6 Key outstanding issues

Several key issues in the single spin experiment remain to be better understood. These issues are:

1. Is the gradient from our tip large enough? If we don't achieve at least 5 Gauss/Å, we may not have sufficient force resolution to detect the signal. We are presently trying to evaluate this gradient using electron holography.

2. What is the lifetime of the spin quantum state during measurement? One concern is anomalously rapid relaxation induced by the proximity of the ferromagnetic tip. This is difficult to evaluate, but should be improved by using tips with large uniaxial anisotropy. If the relaxation rate is too fast (e.g., $> 10\ \text{sec}^{-1}$), then the detection bandwidth needs to be commensurately wide, resulting in increased noise.

3. Are E' centers near the surface of our SiO_2 sample similar in nature to bulk E' centers in terms of number density, relaxation times, etc. We know a lot about E' centers in the bulk, but not near the surface.

4. The tip-sample interaction due to van der Waals and electrostatic forces is much stronger than the single spin magnetic force. Will the single spin signal be overwhelmed by these other forces?

Resolving these remaining issues will be a key part of the follow-on ONR contract.

Bibliography

[1] J. A. Sidles, Phys. Rev. Lett. **68**, 1124 (1992).

[2] D. Rugar, C. S. Yannoni, and J. A. Sidles, Nature **360**, 563 (1992).

[3] J. A. Sidles *et al.*, Rev. Mod. Phys. **67**, 249 (1995).

[4] J. A. Sidles, J. L. Garbini, and G. P. Drobny, Rev. Sci. Instrum. **63**, 3881 (1992).

[5] U. Durig, O. Züger, and A. Stalder, J. Appl. Phys. **72**, 1778 (1992).

[6] J. A. Sidles and D. Rugar, Phys. Rev. Lett. **70**, 3506 (1993).

[7] R. A. Buser and N. F. D. Rooji, Sensors and Actuators **A21–23**, 323 (1990).

[8] T. R. Albrecht, P. Grütter, D. Rugar, and D. P. E. Smith, Ultramicroscopy **42-44**, 1638 (1992).

[9] D. Rugar, H. J. Mamin, and P. Guethner, Appl. Phys. Lett. **55**, 2588 (1989).

[10] Model ESP(W), Digital Instruments Inc., Santa Barbara, CA.

[11] D. Rugar *et al.*, Science **264**, 1560 (1994).

[12] J. Mertz, O. Marti, and J. Mlynek, Appl. Phys. Lett. **62**, 2344 (1993).

[13] K. J. Bruland *et al.*, J. Appl. Phys. **80**, 1959 (1996).

[14] A. Abragam, *The Principles of Nuclear Magnetism* (Oxford University Press, London, 1961).

[15] O. Züger and D. Rugar, Appl. Phys. Lett. **63**, 2496 (1993).

[16] O. Züger and D. Rugar, J. Appl. Phys. **75**, 6211 (1994).

[17] O. Züger, S. T. Hoen, C. S. Yannoni, and D. Rugar, J. Appl. Phys. **79**, 1881 (1996).

[18] C. P. Slichter, *Principles of Magnetic Resonance*, 3rd. ed. (Springer-Verlag, New York, 1990).

[19] W. J. Wallace and R. H. Silsbee, Rev. Sci. Instrum. **62**, 1754 (1991).

[20] H. How, A. Widom, and C. Vittoria, IEEE Trans. Microwave Theory Tech. **39**, 660 (1991).

[21] T. G. Castner, Jr., Phys. Rev. Lett **8**, 13 (1961).

[22] A. M. Portis, A. F. Kip, C. Kittel, and W. H. Brattain, Phys. Rev. **90**, 988 (1953).

[23] H. Ue and S. Maekawa, Phys. Rev. B **3**, 4232 (1971).

[24] G. Feher, Phys. Rev. **114**, 1219 (1959).

[25] R. C. Fletcher *et al.*, Phys. Rev. **94**, 1392 (1954).

[26] T. G. Castner, Jr., Phys. Rev. **130**, 58 (1963).

[27] P. R. Cullis and J. R. Marko, Phys. Rev. B **11**, 4184 (1975).

[28] O. Züger *et al.*, (unpublished).

[29] C. P. Slichter, Phys. Rev. **99**, 479 (1955).

[30] K. J. Bruland *et al.*, Rev. Sci. Instrum. **66**, 2853 (1995).

[31] P. C. Hammel, Z. Zhang, G. J. Moore, and M. L. Roukes, J. Low Temp. Phys. **101**, 59 (1995).

[32] Z. Zhang, M. L. Roukes, and P. C. Hammel, J. Appl. Phys. **80**, 6931 (1996).

[33] D. L. Griscom, Nucl. Instrum. Methods B **1**, 481 (1984).

[34] J. G. Castle, Jr. and D. W. Feldman, J. Appl. Phys. **36**, 124 (1963).

[35] C. S. Yannoni *et al.*, the 38th Rocky Mountain Conference on Analytical Chemistry, 1996.

[36] H.-M. Vieth, R. D. Kendrick, D. Rugar, and C. S. Yannoni, (unpublished).

[37] R. A. Weeks and C. M. Nelson, J. Appl. Phys. **31**, 1555 (1960).

[38] E. L. Hahn, Phys. Rev. **80**, 580 (1950).

[39] S. S. Eaton and G. R. Eaton, J. Magn. Reson. A **102**, 354 (1993).

[40] T. D. Stowe *et al.*, Proceedings of Solid-State Sensor and Actuator Workshop, 1996.

[41] T. D. Stowe *et al.*, Appl. Phys. Lett. **71**, 288 (1997).

[42] EBL#2, Staveley Sensors Inc., East Hartford, CT.

[43] E. L. Hall, in *Computer Image Processing and Recognition* (Academic Press Inc., New York, 1979), pp. 214–239.

[44] Z. Zhang, P. C. Hammel, and P. E. Wigen, Appl. Phys. Lett. **68**, 2005 (1996).

[45] J. F. Dillon, Jr., J. Appl. Phys. **31**, 1605 (1960).